

**A Novel Approach to Data-Driven Modeling of Damage-Induced  
Elastic Wave Propagation**

A Thesis

Submitted to the Faculty

of

Drexel University

by

Daniel Paul Servansky

in partial fulfillment of the

requirements for the degree

of

Master of Science in Mechanical Engineering

June 2012

© Copyright 2012  
Daniel P. Servansky. All Rights Reserved.

## **Dedications**

This research is dedicated in memory of  
Raymond J. Berlot

## Acknowledgements

This Master's Thesis could not have happened without the constant guidance and encouragement imparted upon me by my advisor, Dr. Antonios Kotsos. The dedication to his students and passion for cutting-edge research was endless motivation and inspiration to continue pushing through difficulties toward a successful conclusion. It has truly been an honor to work directly with and learn from Dr. Kotsos.

There is no way for me to fully express my gratitude toward my parents, Paul and Joanne Servansky, for their endless encouragement and confidence in me throughout, not only my career at Drexel University, but also my entire life. They have always been there to motivate me, push me to do my best, and constantly remind me that there are no limitations to what I can do if I set my mind to it.

I owe so much to my loving fiancée, Elizabeth Hoffman, for standing behind my work, inspiring me to believe in myself, and making me laugh when I needed it the most. She made an incredibly selfless decision to work more than full time, so that she could solely support us while I pursued my Master's Degree at Drexel University—for this and for her boundless love and support, I am infinitely grateful.

Finally, I extend my appreciation toward my colleagues, Prashanth Abraham, Dr. Ivan Bartoli, Jefferson Cuadra, Kavan Hazeli, Raghav Saralaya and Eric Schwartz, for their help in my research and enrichment of my academics at Drexel University. I have truly enjoyed working directly with such knowledgeable and helpful group as they have been.

## Table of Contents

List of Tables .....	vi
List of Figures .....	vii
Abstract .....	xii
Chapter 1: Motivation .....	1
1.1 Chapter Contents and Organization .....	2
Chapter 2: Background of Fracture Mechanics .....	9
2.1 Historical Background of Fracture Mechanics .....	9
2.2 Linear Elastic Fracture Mechanics.....	11
2.3 Introduction to the Cohesive Zone Model .....	16
2.4 Cohesive Zone Model Theory .....	19
Chapter 3: Nondestructive Evaluation in the Study of Fracture .....	21
3.1 Acoustic Emissions Testing for Fracture .....	23
3.2 Digital Image Correlation in Fracture .....	28
Chapter 4: Crack Growth Experimentation .....	32
4.1 The Forward Problem of Acoustic Emissions .....	33
4.2 Experimental Setup .....	35
Chapter 5: Data-Driven Simulations of Crack Growth Propagation .....	42
5.1 High-Performance Computational Setup .....	43
5.2 Verification of Linear Elastic Fracture Mechanics in ABAQUS .....	45
5.3 Development of a CZM FORTRAN code .....	49
5.4 Extracting a Realistic Traction Separation Law from DIC Data .....	57
5.5 Integrating User Elements into ABAQUS .....	63
5.6 Integrating FORTRAN into ABAQUS Solver Environment .....	73

5.7 Testing the FORTRAN code and the FORTRAN/ABAQUS interconnectivity ....	76
Chapter 6: Approach to Crack-Driven NDT Simulation .....	81
6.1 Transient Response Due to a Sudden Equilibrium Change .....	82
6.2 The Effect of Excitation Displacement Magnitude on the Transient Response .....	86
6.3 Preparing the Quasi-Static Crack Growth Model for Linking to the Dynamic Model .....	91
6.4 Modifying the Quasi-Static Model for Submodeling with a Dynamic Simulation	93
6.5 Data-Driven Simulation of Damage-Induced Elastic Wave Propagation.....	98
Chapter 7: Conclusions and Future Work.....	104
7.1 Summary and Conclusion .....	104
7.2 Future Work .....	105
List of References .....	108
Appendix A: The Importance of Mesh Independence .....	113
Appendix B: Displacement, Velocity and Acceleration Waveforms due to a 90nm Displacement.....	118
Appendix C: Waveform and Frequency Spectrums Captured during the Dynamic Simulation.....	121

**List of Tables**

Table 1: Mode I Stress Intensity Factors Given for Various Geometry and Loading Conditions [24] .....	15
Table 2: Compact Tension Specimen Dimensions based upon ASTM E399-05 .....	36
Table 3: Input arrays passed from ABAQUS to FORTRAN for the UEL code [52] .....	49
Table 4: Input scalars passed from ABAQUS to FORTRAN for the UEL [31] .....	50
Table 5: Output arrays passed from the FORTRAN UEL code to ABAQUS [31] .....	50
Table 6: Modified quasi-static crack growth simulation scheme .....	93

## List of Figures

Figure 1: Generalized thesis layout by chapter .....	3
Figure 2: J-Integral around the crack tip.....	11
Figure 3: $r$ and $\theta$ orientation ahead of the crack tip .....	13
Figure 4: Barenblatt Cohesive Zone Model with an Example Traction Separation Law .	18
Figure 5: a) Triangular TSL with unequal stress ramp rates; b) Trapezoidal TSL with equally-spaced ramp and plateau separation segments; c) Continuous TSL with a centrally-located critical stress value; d) Piecewise TSL with a sudden drop on stress. ..	18
Figure 6: Continuum Material with a Cohesively Bonded Crack Domain.....	19
Figure 7: (Left) Generalized Ultrasonic Testing (UT) scheme; and (Right) Generalized Acoustic Emissions (AE) testing scheme .....	22
Figure 8: Source location diagram as depicted by Tobias [32] .....	23
Figure 9: AE hit rate during a fatigue loading fracture experiment [34] .....	25
Figure 10: Characteristics of an AE signal .....	26
Figure 11: Acoustic Emissions testing setup in a laboratory setting .....	27
Figure 12: DIC utilized for capturing strain accumulation in a crack growth simulation	29
Figure 13: DIC system setup in a laboratory setting.....	29
Figure 14: Tracking a speckle subset through specimen deformation.....	30
Figure 15: A brief mapping of the Chapter 4 layout.....	33
Figure 16: ASTM E399-05 Compact Tension Specimen Recommended Dimensions ....	36
Figure 17: Displacement Loading for Mode I Fracture Experiment .....	38
Figure 18: Boundary Conditions for Crack-Growth Experiment .....	38
Figure 19: (Left) DIC camera setup during the fracture experiment .....	39
Figure 20: (Right) DIC strain capture at $t=60s$ during the fracture experiment .....	39
Figure 21: MTS displacement and load data collected during the mode I fracture experiment.....	40



Figure 22: A brief mapping of the Chapter 5 layout.....	42
Figure 23: Generalized compute cluster archetecture.....	44
Figure 24: (Left) 2D LEFM verification C(T) specimen with applied loading and boundary conditions.....	46
Figure 25: (Right) 2D LEFM verification C(T) specimen mesh .....	46
Figure 26: Comparison of the 2D MATLAB (Left) solution based upon LEFM equations and ABAQUS (Approximate) 2D solutions for: a) X-Stress b) Y-Stress, and c) Shear Stress fields around a crack tip. ....	47
Figure 27: Comparison of the 2D MATLAB (Left) solution based upon LEFM equations and ABAQUS (Approximate) 2D solutions for: a) X-Displacement, and b) Y-Displacement fields around a crack tip. ....	48
Figure 28: Cohesive Zone Element node pairs .....	52
Figure 29: 3D Planar CZE integration points .....	53
Figure 30: Y-Displacement (Left) and Y-Strain (Right) DIC snapshots at at a) t = 60s and Load = 6.7kN, b) t = 80s and Load = 9.4kN, c) t = 100s and Load =11.5kN, d) t = 120s and Load = 13.2kN .....	58
Figure 31: Stress-Displacement DIC-derived Data .....	59
Figure 32: Two-parameter optimized stress function .....	61
Figure 33: Modified two-parameter optimized stress function.....	63
Figure 34: (Left) Double Cantilever Beam geometry, simplified to the half-model .....	64
Figure 35: (Right) Cohesive Zone Element interface cell .....	64
Figure 36: Boundary Conditions applied to the DCB model.....	65
Figure 37: ABAQUS node naming convention for 20-node continuum brick elements..	67
Figure 38: Separation of the bottom face nodes (blue) and replacement with new (red) nodes .....	68
Figure 39: Shared nodes between the first and second element of the CZE interface cell	69
Figure 40: Shared nodes between the first and second element of the second row and the second element of the first row .....	69

Figure 41: ABAQUS System Information and Configuration Results for a Windows XP x64 system .....	74
Figure 42: Bottom face of the CZE interface cell showing CZE zero-thickness elements .....	77
Figure 43: Stress, Strain and Displacement Field Outputs for a DCB with CZE.....	78
Figure 44: Reaction forces in the first CZE and the applied displacement node.....	79
Figure 45: Nodal displacement along the CZE interface at various time steps .....	80
Figure 46: A brief mapping of the Chapter 6 layout.....	82
Figure 47: Dirac delta function utilized to create a sudden shift in equilibrium states ....	83
Figure 48: General schematic for transient dynamic simulation .....	83
Figure 49: Elastic stress wave propagation due to a Dirac delta displacement of 90nm..	84
Figure 50: Out-of-plane displacements and frequency spectrums recorded at the near-, mid-, and far-field locations.....	85
Figure 51: Frequency of the Peak Amplitude in the Power Spectrum .....	87
Figure 52: Displacement and frequency spectrums for various peak excitation displacements .....	89
Figure 53: Peak waveform displacement.....	90
Figure 54: Peak frequency spectrum power.....	90
Figure 55: (Left) First equilibrium state – Directly before crack extension .....	92
Figure 56: (Right) Second equilibrium state – After 2.0 mm of crack growth.....	92
Figure 57: Through-thickness stress distribution at the second equilibrium point.....	93
Figure 58: Submodel created by cutting away a large portion of the original quasi-static crack growth model.....	94
Figure 59: Front face partition for sensor location .....	95
Figure 60: Sensors, denoted by red dots, located at the intersection of the partitions.....	95
Figure 61: Global seed array for the dynamic model .....	96
Figure 62: (Left) Tetrahedron mesh utilized for the dynamic simulation .....	97

Figure 63: (Right) Zoomed view of the tetrahedron mesh .....	97
Figure 64: Selected faces to apply submodel boundary conditions .....	98
Figure 65: Elastic stress wave propagation in the dynamic submodeling simulation that has been driven by the equilibrium states of the quasi-static simulation.....	100
Figure 66: Displacement, Velocity and Acceleration waveforms captured at sensor location 4 and their associated frequency spectrum analyses .....	101
Figure 67: AE waveforms and frequency spectrums captured by the dynamic simulation (Left) and by Vanniamparambil (Right) [3] .....	103
Figure 68: AE sensor location during an Aluminum Alloy 2024-T3 crack growth experiment [3].....	103
Figure 69: (Left) Theoretically infinite plate with a circular hole in the center. ....	114
Figure 70: (Right) Boundary conditions applied to the theoretically infinite plate.....	114
Figure 71: a) 1mm mesh, b) 0.1mm mesh and c) 0.05mm mesh and the associated stress contour for d) 1mm e) 0.1mm and f) 0.05mm meshes. ....	116
Figure 72: Mesh dependence simulation results .....	117
Figure 73: Displacement, Velocity and Acceleration waveforms captured at the near-field sensor and their associated frequency spectrum analyses.....	118
Figure 74: Displacement, Velocity and Acceleration waveforms captured at the mid-field sensor and their associated frequency spectrum analyses.....	119
Figure 75: Displacement, Velocity and Acceleration waveforms captured at the far-field sensor and their associated frequency spectrum analyses.....	120
Figure 76: Displacement, Velocity and Acceleration waveforms captured at sensor location 1 and their associated frequency spectrum analyses .....	121
Figure 77: Displacement, Velocity and Acceleration waveforms captured at sensor location 2 and their associated frequency spectrum analyses .....	122
Figure 78: Displacement, Velocity and Acceleration waveforms captured at sensor location 3 and their associated frequency spectrum analyses .....	123
Figure 79: Displacement, Velocity and Acceleration waveforms captured at sensor location 4 and their associated frequency spectrum analyses .....	124

Figure 80: Displacement, Velocity and Acceleration waveforms captured at sensor location 5 and their associated frequency spectrum analyses .....	125
Figure 81: Displacement, Velocity and Acceleration waveforms captured at sensor location 6 and their associated frequency spectrum analyses .....	126
Figure 82: Displacement, Velocity and Acceleration waveforms captured at sensor location 7 and their associated frequency spectrum analyses .....	127
Figure 83: Displacement, Velocity and Acceleration waveforms captured at sensor location 8 and their associated frequency spectrum analyses .....	128

**Abstract****A Novel Approach to Data-Driven Modeling of Damage-Induced  
Elastic Wave Propagation****Daniel Paul Servansky  
Antonios Kontsis, Ph.D.**

Current research into the simulation of elastic stress wave propagation utilizes user-imposed energy functions to drive the required energy changes for the production of elastic waves that propagate through the continuum model. This thesis proposes a novel approach to theoretically investigate the creation and propagation of elastic stress waves in a computational model by linking "experimental data-driven" quasi-static crack growth simulations with dynamic simulations for transient elastic wave propagation. The quasi-static simulations are used to determine both the displacement, strain and stress fields associated with crack initiation and the rate at which the crack will grow. As these elastic fields change over time as a function of crack growth increments, the dynamic model is used to capture the changes in the stored energy that lead to new equilibrium states for a developing crack, as well as the transient path followed to achieve this structural evolution. Within this energy balance lies the production and propagation of elastic stress waves associated with energy released by the crack growth. In the computational models, specific locations are selected for monitoring in- and out-of-plane displacement, velocity and acceleration. Such data generated by the model and captured by numerical sensors are analyzed in both time and frequency domains and are compared to related experimental measurements. The computationally generated transient elastic stress waves that propagate through the model produce the equivalent of what is known as Acoustic Emissions, providing in this way an innovative approach to directly link fracture

mechanics with theory related to nondestructive testing. The research findings in this thesis are expected to contribute towards the design of more efficient strategies for the fundamental understanding of the fracture process, as well as for the reliable damage monitoring in structural health monitoring applications.



## Chapter 1: Motivation

Damage monitoring in solids is the concept of watching, listening and predicting the occurrence of deformation and ultimate failure based upon an observed phenomenon. It is through the understanding of what drives damage, how damage may occur, and what the result will be when damage does occur that allows engineers to pioneer new materials, build structures more efficiently, improve safety and efficiently diagnose and repair a damaged structure.

From a theoretical standpoint, near-field crack tip stresses, strains and displacements can be predicted through linear elastic fracture mechanics, elastic-plastic fracture mechanics, and fully plastic fracture mechanics [1]. Additionally, the onset and propagation of a crack can be predicted through the use of several concepts such as Crack Tip Opening Displacement, Cohesive Zone Theory, J-Integral, and Coulomb Fracture, just to name a few. Experimentally, fracture has mostly been studied based on test standards which have proven methods of computing a material's Fracture Strength, Fracture Resistance, Strain Energy Release Rate and other fracture-related quantities. Moreover, over the past four decades, advanced techniques for nondestructive testing (NDT) of damage in solids, including for example Ultrasonic Testing and Eddy Current testing among other, and assisted by microscopy, have offered a glimpse into how damage occurs through the depth of a solid [2]. Further, NDT for monitoring of damage in solids, include Digital Image Correlation and Acoustic Emissions Testing which have offered the capability to monitor, in real-time, the effect, leading up to, while occurring and after, damage has on a solid. Digital Image Correlation, for example, is an advanced metrology technique which is capable of measuring full-field displacements and strain on the surface of a solid which



can be utilized to predict the location, formation and propagation of damage. Acoustic Emissions Testing, on the other hand, listens to the solid, in the way that a seismologist listens to the earth, for bursts of stress waves that have been generated by the sudden release of energy in damage. The utilization of several sensors allows for the pinpointing of the "epicenter" and again can predict, based on this information, the location of damage.

As technology continues to advance and more accurate sensors and images can be captured, the next generation of data-driven fracture models are being developed to aid in the understanding of the fracture phenomenon. The constitutive framework for these data-driven fracture models is built in this thesis by combining state-of-the-art in-situ methodology [3], data-driven fracture parameters [4], and advanced techniques of damage modeling [5, 6]. The ultimate goal of this scheme is to build a damage model that is based on and updated with real-time experimental results.

### *1.1 Chapter Contents and Organization*

This thesis is organized in a manner that is intended to lay out a basic background understanding of fracture mechanics, cohesive zone modeling and the forward acoustic emissions problem. After becoming familiar with the forward acoustic emissions problem the experimental setup and reasoning, which is the basis of gathering realistic damage parameters, is explained in detail. The parameters of the experimental scheme were chosen to excite a specific type of fracture in a ductile material. The damage parameters and stress function which drive the cohesive zone model will be extracted from

experimental data and applied to Cohesive Zone Elements in a quasi-static crack growth Finite Element Model which mimics the experimental scheme.

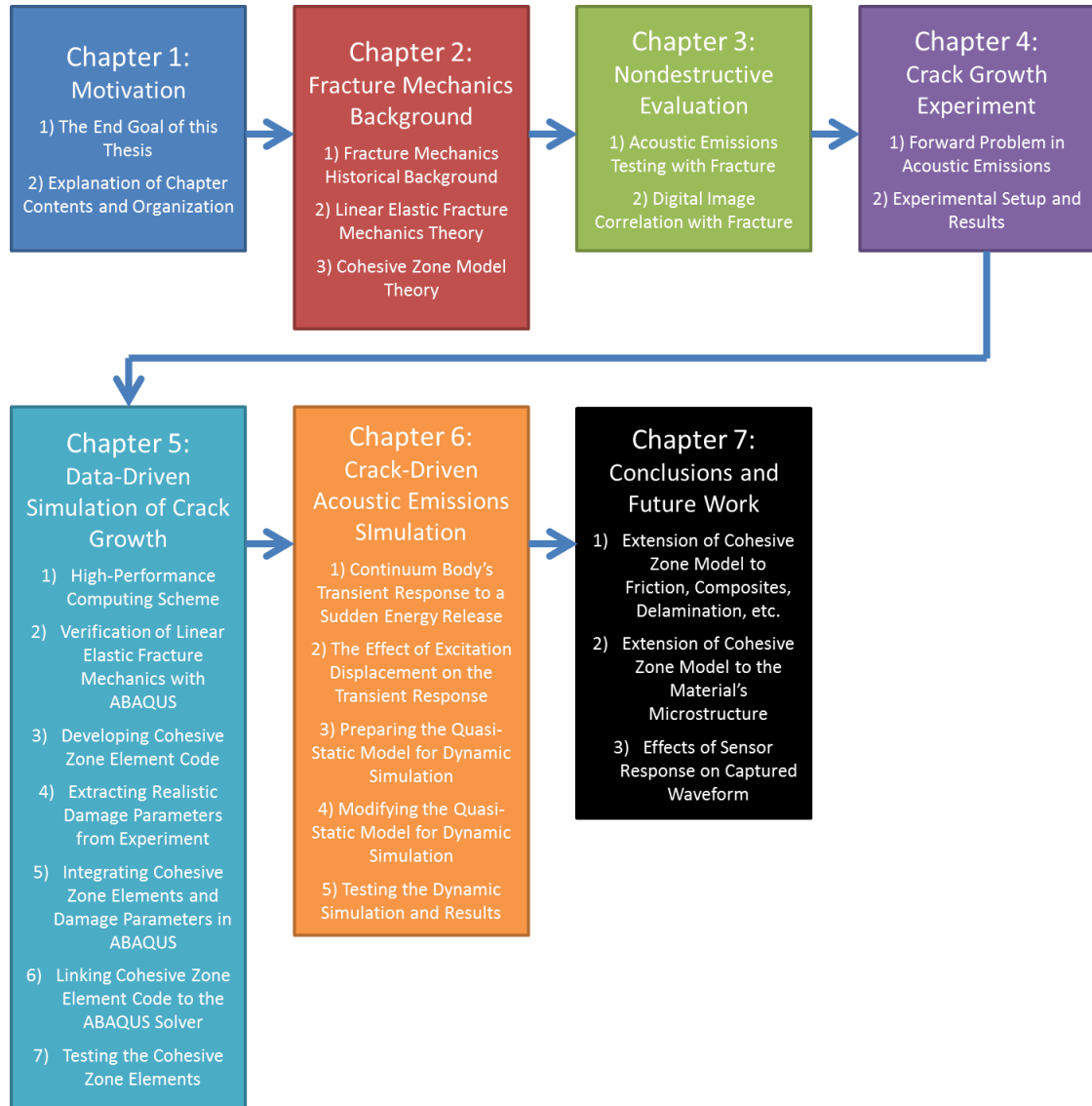


Figure 1: Generalized thesis layout by chapter

The crack in the quasi-static simulation, which is driven by realistic damage parameters, will be allowed to grow and snapshots of equilibrium points before and after crack extension will be captured and utilized as boundary conditions to a dynamic simulation. The dynamic simulation will find the transient path by which the equilibrium state shifts from the point before crack extension to the point after crack extension. Within this transient response will be the sudden release of energy that drives the creation and propagation of elastic stress waves. Such waves will be monitored at various locations throughout the model in a way that simulates the application of piezoelectric sensors in standard Acoustic Emissions testing setups. The out-of-plane displacement, velocity and acceleration will be captured at these “sensor” locations throughout the dynamic simulation.

The first chapter is primarily designed to bring attention to the present state-of-the-art methods of theoretical and experimental damage monitoring in solids and shine light on the novelty of the methods discussed within this thesis for a data-driven approach to the simulation of damage-induced elastic wave propagation. Secondly, this chapter will introduce the reader to the topics which will be covered in each chapter and offer some guidance to the appearance of material.

The second chapter will familiarize the reader with the history of Fracture Mechanics, starting with work done by Leonardo Da Vinci, and moving up through modern fracture studies such as Cohesive Zone Modeling. An in-depth look at linear elastic fracture mechanics and the governing equations being crack advancement will be discussed in the second part of this chapter. Following linear elastic fracture mechanics is a more in-depth look at the theory behind Cohesive Zone Modeling, the application and importance of the

Traction Separation Law to Fracture Mechanics, and the mathematical theory and virtual energy balance that governs the reaction of the Cohesive Zone Model with respect to the continuum body.

The third chapter will outline a brief history of Nondestructive Evaluation and Structural Health Monitoring with a focus on Nondestructive Testing methods, such as Acoustic Emissions and Ultrasonic Testing testing, as well as Digital Image Correlation. The direct application of Acoustic Emission in fracture will be discussed with a focus on research in the past thirty years. Additionally, extensive information will be presented on the measurement characteristics of an Acoustic Emission signal and effective methods of tracking them.

The theory behind Digital Image Correlation, including surface detail mapping, specimen preparation, displacement computation and unique applications will be presented. Key benefits of Digital Image Correlation and its ability to be incorporated into Nondestructive Evaluation and Finite Element Analysis will be highlighted.

Chapter 4 will begin the methodology behind the novel approach discussed throughout this thesis. A differentiation between the forward (production) and inverse (capturing) problems of Acoustic Emissions testing will be made and an outline of the method for utilizing advanced Nondestructive Evaluation techniques to drive a Finite Element model will be outlined. In addition, the experimental scheme, which has been specifically designed to perform controlled Mode I mechanical testing of commercial alloy specimens, while monitoring the fracture process using Acoustic Emissions and Digital Image Correlation will be drawn.

Chapter 5 dives into the quasi-static crack growth simulation, which is based upon experimentally derived damage parameters, by creating a map of the 64-core High-Performance Computing setup that was designed specifically for running ABAQUS simulations. Secondly, the chapter will show the development of ABAQUS simulations for the verification of linear elastic fracture mechanics theories discussed in Chapter 2. Next, the development of a Cohesive Zone Model user element code, based on the FORTRAN language, is established and the link between the user element code and the ABAQUS solver is made. The application and insertion of the Cohesive Zone Elements (i.e. the user elements) into an ABAQUS model is discussed before testing the application of Cohesive Zone Elements with a Double Cantilever Beam simulation.

Chapter 6 is based around the transient response of solids due to an excitation caused by a sudden energy release. In the first case, the same Double Cantilever Beam used in the last part of Chapter 5, is modeled with a sudden energy release applied as a Dirac delta function of displacement, which peaks at 90nm, at the crack tip. In this case, there are no cohesive elements,. Sensors are placed at near-, mid- and far-field locations where out-of-plane displacements, velocities and accelerations are captured and analyzed. The second part of Chapter 6 studies the effect of peak displacement on the transient response of the continuum s. Here, the same Double Cantilever Beam model with the same sensor location and displacement algorithm are used, however peak displacements imparted by the Dirac delta function vary by simulation as follows: 60nm, 90nm, 500nm and 50 $\mu$ m.

The third section is where everything presented up to that point comes together as one unit—this is the data-driven damage-induced elastic wave propagation. This model began with the experiment presented in Chapter 4 where advanced metrology and active

Nondestructive Testing was utilized to capture key information about the specimen as it was loaded and began to fail. From this, realistic damage parameters, specific to Cohesive Zone Modeling, were extracted and input into a user-generated Cohesive Zone Element algorithm which calculates the stress based upon the separation of a material bridge ahead of the crack tip. The last section of Chapter 5 develops the model that will be the basis of the transient response. The Cohesive Zone Elements are inserted into a model that represents a section of the experimental specimen used in Chapter 4. This model is loaded and the crack is allowed to propagate. Full-field equilibrium displacements, stresses and strains are captured as a “snapshot” directly before crack growth begins and after a determined amount of crack propagation. The exact model that was utilized to create these “snapshots” will now be used to model the transient response of the system during the equilibrium shift, which includes the propagation of the crack. The “snapshots” are used as inputs in the dynamic model thus no other user-based parameter which defines energy release is applied to this model—*the energy release characteristics are generated fully by the quasi-static crack growth model*. As with the simulations in the first half of Chapter 6, sensors are placed throughout the model to capture out-of-plane displacement, velocity and accelerations, which will be analyzed. Chapter 7 concludes this thesis by reviewing the results presented throughout and drawing conclusions based upon these findings. Future work will include the implementation of crack branching [7, 8] and mixed-mode fracture [9] with the current scheme. Additionally, Cohesive Zone Modeling can be extended to non-homogeneous materials such as composites [10-12] and used to model the effects of friction [13, 14]. Finally, sensory system itself can be taken into account to determine the effects of the

piezoelectric crystals, the continuum material-sensor interface and the conversion of elastic waves into electric signals, on the variations observed between the produced "primitive" elastic waves due to damage and experimentally captured waves [6].

## Chapter 2: Background of Fracture Mechanics

The study of fracture mechanics is centuries old; however, it was not until more recent years that a more realistic and applicable understanding of fracture mechanics became possible by using advances in both experimental and computational tools. A major driving force behind these advances is the rapid growth of computational performance, and the paralleled growth of Finite Element (FE) capability. Additionally, the discovery of electron microscopy in the mid-1980's allowed for the direct observation of fracture surfaces down to micro and nano scale which has opened the possibility to validate, enhance and make key advances in both fracture mechanics and techniques used for damage monitoring such as Nondestructive Evaluation (NDE) techniques including Acoustic Emission (AE) monitoring and Digital Image Correlation (DIC) [15, 16]. This chapter will give a basic background on the history of fracture mechanics, including the initial studies of Leonardo da Vinci, the early works of A.A. Griffith up through the development of the Barneblatt/Dugdale Cohesive Zone Model (CZM). A major focus of this chapter will be the understanding of Cohesive Zone Modeling and the application to FE simulations. The chapter will close with an organizational summary of this thesis.

### *2.1 Historical Background of Fracture Mechanics*

The study of fracture mechanics dates back to Leonardo da Vinci [1] who is credited with conducting tests on iron wires whereby he discovered that strength was inversely correlated to wire length which implied that given a homogenous material, material flaws influence strength through the assumption that the number of flaws increases as the volume of material increases. The theoretical and mathematical connection between



material flaws and material strength was not developed until 1920 by A. A. Griffith [17] who formulated a fracture theory based on simple energy balance. Additionally, he postulated that in the case of two identical plates, a plate that has a surface scratch will fail prior to a plate with no surface scratch. A simple example of this theory is the use of scoring glass to facilitate breaking: Glassworkers will score glass to produce a clean cut along the score line. Griffin's theories, however, only applied to brittle materials such as glass and ceramics. The next major development in fracture mechanics came after World War II when the G.R. Irwin formulated, and the Ship Structure Committee division of the Navy expanded upon, the theory of localized plastic flow and energy release rates in metal plates [1]. In 1954 Irwin realized that there was an additional strain component in metals which was not present in brittle materials [18]. This, he proposed, was the strain component due to plastic deformation near the material flaw. By 1956, in conjunction with the Naval Research Laboratory [19], Irwin developed a theory, based upon earlier work by H.M. Westergaard [20], by which the stress and displacement near the crack tip could be correlated directly to the Energy Release Rate through a constant parameter known as the "Stress Intensity Factor" (SIF) [1]. Up to this point, it is important to note that the research was based around linear elastic materials, that is little or no plastic deformation occurred around the crack tip. Several modifications of the Linear Elastic Fracture Mechanics (LEFM) theories began to be developed to account for materials that had significant yielding at and near the crack tip. In 1968, J.R. Rice proposed the idea of the well-known J-Integral [21] which is a path-independent closed-loop integral surrounding the crack tip in a two-dimensional strain field as seen in Figure 2.

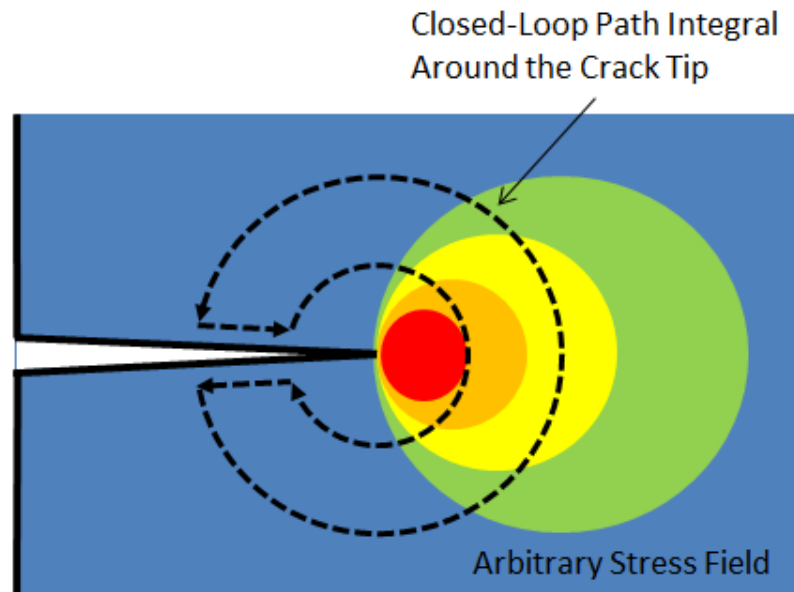


Figure 2: J-Integral around the crack tip

The averaged value of the strain concentration near the crack tip is used to approximate near-tip stress and strain singularities, Crack Tip Opening Displacement (CTOD), crack tip blunting and the plastic zone size. In 1960 and 1962, Dugdale and Barenblatt, respectively, developed theories on inelastic material behavior at and around the crack tip [22]. Both theories would later become known as the “Cohesive Zone Model” (CZM) which will be discussed in detail in the next section. More recent fracture mechanics have focused on the addition of time-dependent variables in fracture models and theories, and the incorporation of fracture prediction into design and simulation [1].

## 2.2 Linear Elastic Fracture Mechanics

Linear Elastic Fracture Mechanics (LEFM) is a set of energy-based theories governing the propagation of a crack in a continuum body. One of the most commonly used

parameter is known as the Strain Energy Release Rate (SERR) that is denoted with  $G$  and is in the units of  $\text{J/m}^2$ . The SERR is defined as the energy released during fracture per unit area due to the creation of new crack surfaces. In order for the crack to grow, the energy added to the system through the application of boundary traction and displacement loading conditions must be balanced by the released energy due to changes caused by the formation of new crack surfaces plus the dissipation due to phenomena such as heat and sound. Mathematically, the SERR is equivalent to the negative change in potential energy per change in crack length (E2.1).

$$G = -\frac{\partial U}{\partial a} \quad (\text{E2.1})$$

Where  $U$  is the potential energy and  $a$  is the crack length. The Fracture Energy, denoted as  $G_c$ , is considered to be a geometry and load-independent material property and corresponds to a fracture initiation criterion.

Along with the description of the fracture process using an energy framework, the elastic fields at the crack tip which govern crack growth have been modeled using the concept of Stress Intensity Factor (SIF), denoted by  $K_i$  where  $i$  corresponds to I, II or III for Mode I, II or III fracture, respectively. Mode I fracture is caused by tensile opening whereas Mode II and Mode III are in-plane (sliding) and out-of-plane shear (tearing), respectively. The SIF is typically used to estimate the intensity of stresses near the crack tip and is most accurate when applied to linear elastic and homogenous material [1]. The value of the SIF itself is dependent upon the specimen geometry, the loading conditions and size

of the crack which is demonstrated in Table 2.1 where various geometries and their related Mode I Stress Intensity Factors are given. The generalized definitions of SIF are given in equation (E2.2).

$$\begin{aligned}
 K_I &= \lim_{r \rightarrow 0} \sqrt{2\pi r} \sigma_{yy}(r, 0) \\
 K_{II} &= \lim_{r \rightarrow 0} \sqrt{2\pi r} \sigma_{xy}(r, 0) \\
 K_{III} &= \lim_{r \rightarrow 0} \sqrt{2\pi r} \sigma_{yz}(r, 0)
 \end{aligned}
 \tag{E2.1}$$

Where  $\sigma_{ij}(r, \theta)$  is a stress function dependent upon the radius,  $r$ , and angle,  $\theta$ , from the crack tip as illustrated in Figure 3. Note that equation (E2.1) contains a special case of the  $\sigma_{ij}(r, \theta)$  function where theta is always parallel to the propagation of the crack.

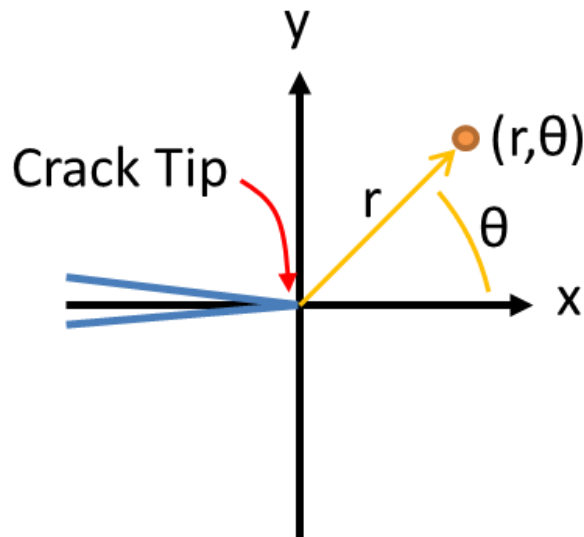


Figure 3:  $r$  and  $\theta$  orientation ahead of the crack tip

Failure will occur when the SIF reaches a critical level known as the Fracture Toughness, denoted as  $K_{iC}$  where  $i$  corresponds to the fracture mode. Fracture toughness is a measurement of the material's ability to resist fracture and is in the units of  $\text{Pa} \cdot \text{m}^{1/2}$ .

Stress intensity is an additional way to consider driving forces for fracture. Moreover, fracture toughness of a linear elastic material can be related to the Critical SERR through equation (E2.2) where  $E$  is the material's Young's (Elastic) Modulus,  $\nu$  is the Poisson's Ratio and  $\mu$  is the Shear Modulus. Similarly, the three Stress Intensity Factors can be related to the SERR through equation (E2.3) [23].

$$G_c = K_{Ic}^2 \left( \frac{1 - \nu^2}{E} \right) + K_{IIc}^2 \left( \frac{1 - \nu^2}{E} \right) + K_{IIIc}^2 \left( \frac{1}{2\mu} \right) \quad (\text{E2.2})$$

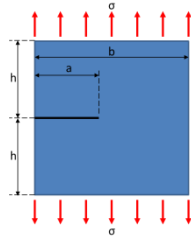
$$G = K_I^2 \left( \frac{1 - \nu^2}{E} \right) + K_{II}^2 \left( \frac{1 - \nu^2}{E} \right) + K_{III}^2 \left( \frac{1}{2\mu} \right) \quad (\text{E2.3})$$

Note that in the case of pure Mode I, Mode II or Mode III fracture, equations (E2.2) and (E2.3) reduce to a direct relationship between SERR and the corresponding SIF. In all other cases of mixed-mode fracture, the two equations involve combinations of individual SIF.

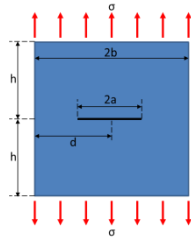
**Table 1: Mode I Stress Intensity Factors Given for Various Geometry and Loading Conditions [24]**

Geometry

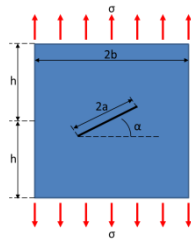
Mode I Stress Intensity Factor



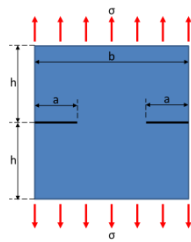
$$K_I = \sigma\sqrt{\pi a} \left[ 1.12 - 0.23 \left(\frac{a}{b}\right) + 10.6 \left(\frac{a}{b}\right)^2 - 21.7 \left(\frac{a}{b}\right)^3 + 30.4 \left(\frac{a}{b}\right)^4 \right]$$



$$K_I = \sigma\sqrt{\pi a} \left[ \frac{1 - \frac{a}{2b} + 0.326 \left(\frac{a}{b}\right)^2}{\sqrt{1 - \frac{a}{b}}} \right]$$



$$K_I = \sigma\sqrt{\pi a} [\cos^2 \alpha]$$



$$K_I = \sigma\sqrt{\pi a} \left[ 1.99 - 0.41 \left(\frac{a}{b}\right) + 18.7 \left(\frac{a}{b}\right)^2 - 38.48 \left(\frac{a}{b}\right)^3 + 53.85 \left(\frac{a}{b}\right)^4 \right]$$

The Stress Intensity Factor is also used to map stress, strain and displacement contours ahead of a crack tip in a continuum body. In general these take on the forms in equation (E2.4).

$$\begin{aligned}
\sigma_{ij}(r, \theta) &= f(r) \cdot K_m \cdot [\sigma(\theta)] \\
\varepsilon_{ij}(r, \theta) &= f(r) \cdot K_m \cdot [\varepsilon(\theta)] \\
u_i(r, \theta) &= f(r) \cdot K_m \cdot [u(\theta)]
\end{aligned} \tag{E2.4}$$

Where  $f(r)$  is a function dependent upon only the radius from the crack tip,  $r$ ,  $K_m$  is the  $m$ -th SIF, and  $\sigma(\theta)$ ,  $\varepsilon(\theta)$ , and  $u(\theta)$ , are functions of stress, strain and displacement, respectively, at an angle,  $\theta$ , from the crack tip. In Mode I, as discussed by David Broek and Kare Hellan [23, 24], the stress and displacement function are as follows.

$$\sigma_{11}(r, \theta) = \frac{K_I}{\sqrt{2\pi r}} \cos \frac{\theta}{2} \left[ 1 - \sin \frac{\theta}{2} \sin \frac{3\theta}{2} \right] \tag{E2.5a}$$

$$\sigma_{22}(r, \theta) = \frac{K_I}{\sqrt{2\pi r}} \cos \frac{\theta}{2} \left[ 1 + \sin \frac{\theta}{2} \sin \frac{3\theta}{2} \right] \tag{E2.5b}$$

$$\sigma_{33}(r, \theta) = \begin{cases} 0, & \text{Plane Stress} \\ \nu(\sigma_{11} + \sigma_{22}), & \text{Plane Strain} \end{cases} \tag{E2.5c}$$

$$\sigma_{12}(r, \theta) = \cos \frac{\theta}{2} \sin \frac{\theta}{2} \cos \frac{3\theta}{2} \tag{E2.5d}$$

$$\sigma_{23}(r, \theta) = \sigma_{13}(r, \theta) = 0 \tag{E2.5e}$$

$$u_x(r, \theta) = \frac{K_I}{\mu} \sqrt{\frac{r}{2\pi}} \cos \frac{\theta}{2} \left[ \kappa - 1 + 2 \sin^2 \frac{\theta}{2} \right] \tag{E2.6a}$$

$$u_y(r, \theta) = \frac{K_I}{\mu} \sqrt{\frac{r}{2\pi}} \sin \frac{\theta}{2} \left[ \kappa + 1 - 2 \cos^2 \frac{\theta}{2} \right] \tag{E2.6b}$$

### 2.3 Introduction to the Cohesive Zone Model

Barenblatt introduced the Cohesive Zone Model (CZM) for brittle materials by integrating the nonlinear affects of micro-scale damage mechanics with linear fracture

mechanics and imposing a material-dependent fracture resistance known as the Traction Separation Law (TSL). The TSL is a stress function of separation, [25] as depicted in Figure 4, which, depending upon the application of the cohesive elements, may be a smooth or continuous piecewise function in order to create an appropriate stress field along the crack front. The stresses induced by the TSL are known as ‘closure stresses’ and they counter the separation occurring due to an applied load. In other words, they are the material’s resistance to opening. Generally, as the separation increases, the material’s resistance to opening increases similarly to the reaction of a spring. There is a certain point, however, where the material can no longer continue to resist the separation and damage will begin to occur either as softening such as plastic deformation, or catastrophically such as fracture. Figure 5 depicts several common Traction Separation Laws, the simplest of which is one of triangular nature where the stress ramps linearly upward to the point of separation where a critical stress is reached. Beyond this point, the stress ramps linearly downward, potentially at a different rate than the initial ramp-up, to the critical separation value where stress is zero and the material fails. Similarly, a trapezoidal TSL will linearly ramp upward to the critical stress level; however, instead of the stress immediately beginning to linearly ramp down, a plateau, where the critical stress level is maintained, exists between two defined separation values. More complex TSL exist where stress is a smooth function of separation. In such cases the idealized TSL is often determined experimentally or theoretically. In the Barenblatt model, a balance is found between the opening stresses caused by forces external to the crack surface and the closure forces produced by the TSL.



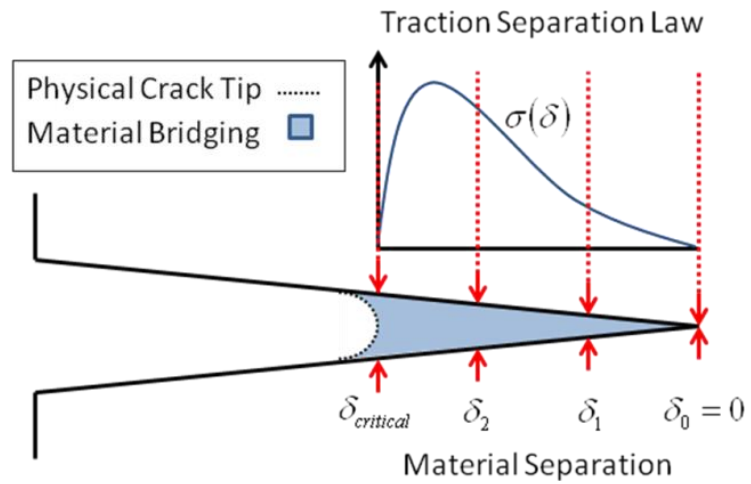


Figure 4: Barenblatt Cohesive Zone Model with an Example Traction Separation Law

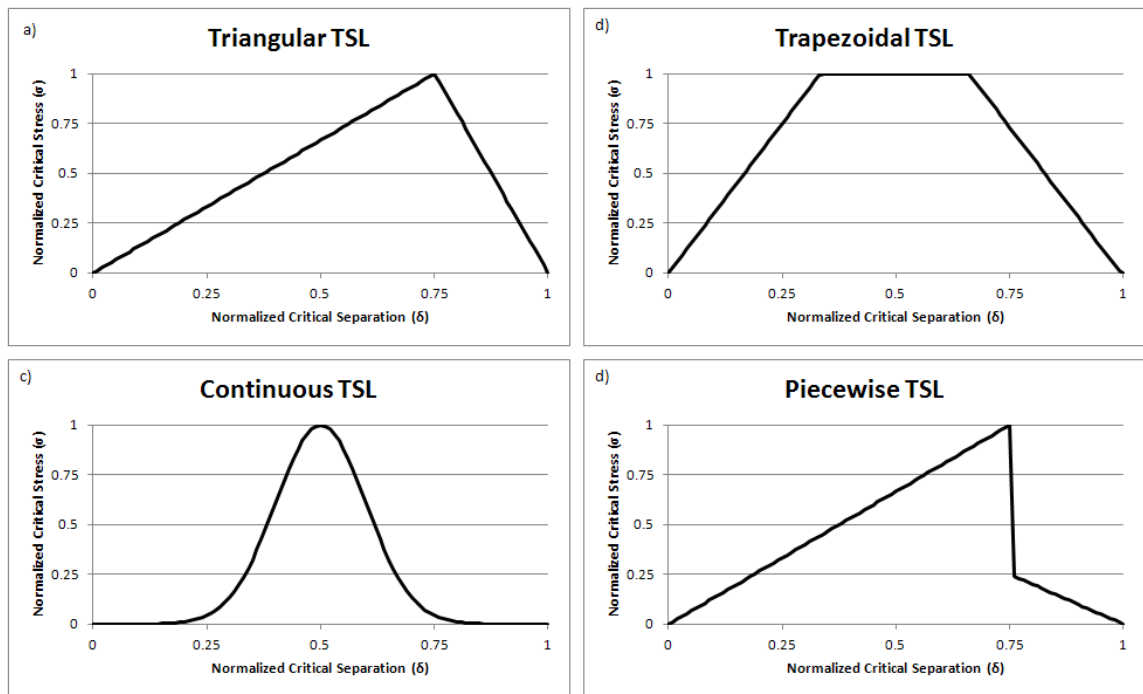


Figure 5: a) Triangular TSL with unequal stress ramp rates; b) Trapezoidal TSL with equally-spaced ramp and plateau separation segments; c) Continuous TSL with a centrally-located critical stress value; d) Piecewise TSL with a sudden drop on stress.

### 2.4 Cohesive Zone Model Theory

Cohesive Zone Modeling is based around the principal of virtual work [26] and can be represented in a continuum,  $\Omega$ , with external traction,  $\mathbf{T}$ , acting upon boundary,  $\Gamma$ , and internal traction,  $\mathbf{T}_c$ , acting upon the cracked boundary,  $\Gamma_c$ , through the following equation:

$$\int_{\Omega} \Delta \boldsymbol{\varepsilon}^T \cdot \boldsymbol{\sigma} d\Omega + \int_{\Gamma_c} \Delta \boldsymbol{\delta}^T \cdot \mathbf{T}_c d\Gamma_c = \int_{\Gamma} \Delta \mathbf{u}^T \cdot \mathbf{T} d\Gamma \quad (\text{E2.7})$$

$$\Delta W_{\text{continuum}} + \Delta W_{\text{cohesive}} = \Delta W_{\text{external}} \quad (\text{E2.8})$$

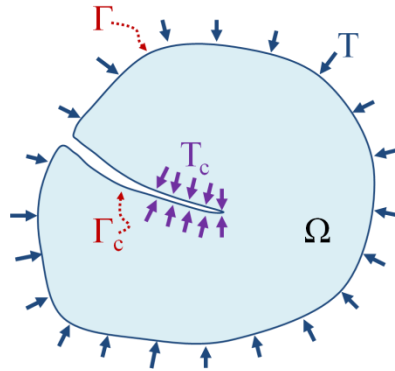


Figure 6: Continuum Material with a Cohesively Bonded Crack Domain

Where  $\Delta \boldsymbol{\varepsilon}$  is the virtual strain tensor,  $\boldsymbol{\sigma}$  is the Cauchy stress tensor,  $\Delta \mathbf{u}$  is the virtual displacement along the boundary,  $\Gamma$ , and  $\Delta \boldsymbol{\delta}$  is the virtual crack face separation along the cohesive boundary within  $\Gamma_c$ . The Cauchy stress tensor is related to the traction in the  $n$ -direction through E2.9 where  $n_j$  is the  $j$ -direction component of the normal  $\mathbf{n}$ .

$$\mathbf{T}^{(n)} = \boldsymbol{\sigma} \cdot \mathbf{n} \text{ or in tensor notation, } T_j^{(n)} = \sigma_{ij} n_j \quad (\text{E2.9})$$

The first term in (E2.7) quantifies the energy stored in the continuum whereas the second term represents the energy associated with the cohesive traction  $T_c$  acting along the boundary  $\Gamma_c$ . These two terms are equal to the right hand side in (E2.7) which is the total work done by the imposed traction  $T$  along boundary  $\Gamma$ .

### **Chapter 3: Nondestructive Evaluation in the Study of Fracture**

Nondestructive Evaluation (NDE) is a principle which has existed for centuries in one form or another and came to light by the realization that all structures, whether manmade or not, are not invincible and will eventually deteriorate and fail [27]. The earliest form of NDE, and still the most commonly employed, is visual inspection of a structure for outward signs of fatigue and failure such as cracks, corrosion, oxidation, etc. Before proceeding, a distinction should be made between terms relating to NDE: Nondestructive Testing (NDT) and Nondestructive Inspection (NDI). While the three terms presented thus far may, theoretically, be interchangeable when speaking about the principle at hand, a distinction will be drawn for this thesis: Nondestructive Testing and Nondestructive Inspection are, for all intents and purposes, interchangeable and can be defined as the act of using tools and sensors to collect information about a structure in a manner which is not detrimental to the structure's integrity. Nondestructive Evaluation is the act of using the information gathered through NDT to make an educated analysis of the flaws, weaknesses and integrity of a structure.

Over the past four decades, several new, and significantly more accurate, acoustic-based methods of NDT have come to fruition, majorly due to the exponential growth in capabilities of computers and sensors. An ideal goal of NDE is to develop an integrated and robust Structural Health Monitoring (SHM) system to, first and foremost, improve safety for the public by monitoring and alerting structural owners of damage in real-time [3, 28] and to improve the cost and maintenance scheduling of large structures such as bridges. Two common acoustic-based methods utilized in SHM are Ultrasonic Testing (UT) and Acoustic Emissions (AE) monitoring, which work under the same general idea

based on which acoustic stress waves can be generated and tracked as they travel in a continuum body. The major difference, as depicted in Figure 7, is that UT is an active monitoring system, meaning that the user generates a surface/point pulse which creates stress waves in the continuum [29], whereas AE is a passive monitoring system[2], meaning that the elastic stress waves are induced by sudden changes in energy caused for example by failure, among other reasons [30].

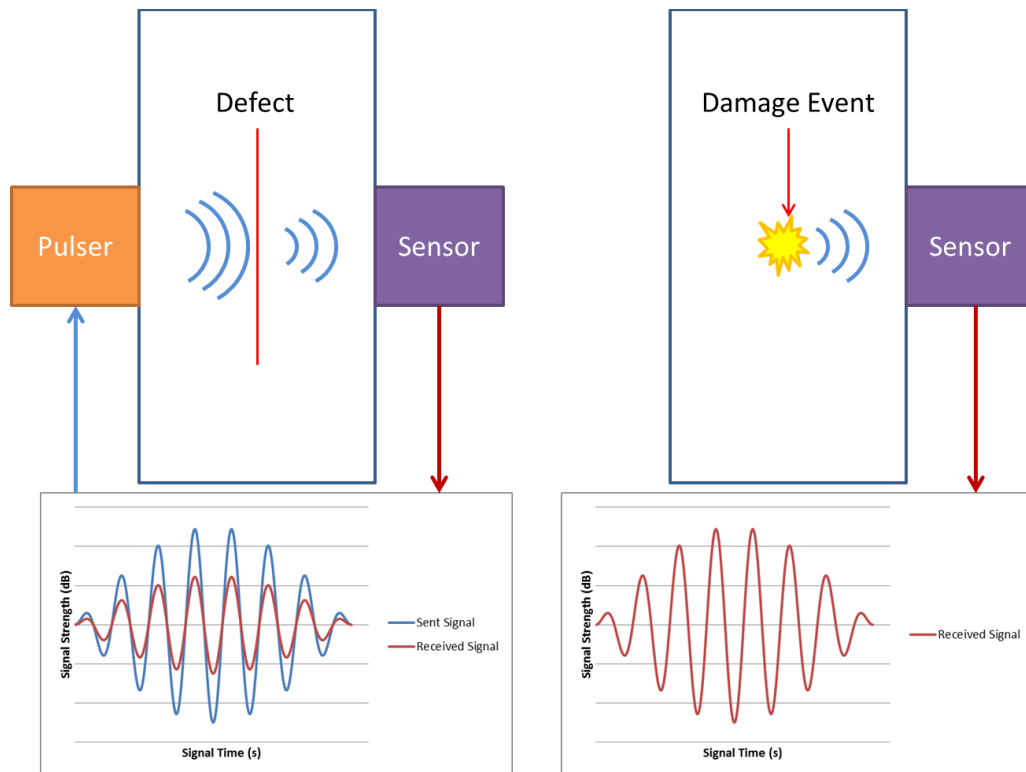


**Figure 7: (Left) Generalized Ultrasonic Testing (UT) scheme; and (Right) Generalized Acoustic Emissions (AE) testing scheme**

### 3.1 Acoustic Emissions Testing for Fracture

In a larger sense, AE can be directly related to the science of seismology where, in seismology, the specimen is the earth, the sensors are the seismographs, and the elastic stress waves are the shockwaves generated by the earthquake [30]. Similar to seismology, the data acquired at multiple locations, as described by Tobias, can be used in conjunction with the theoretical wave speed to pinpoint the source location in the three-dimensional space [31, 32].

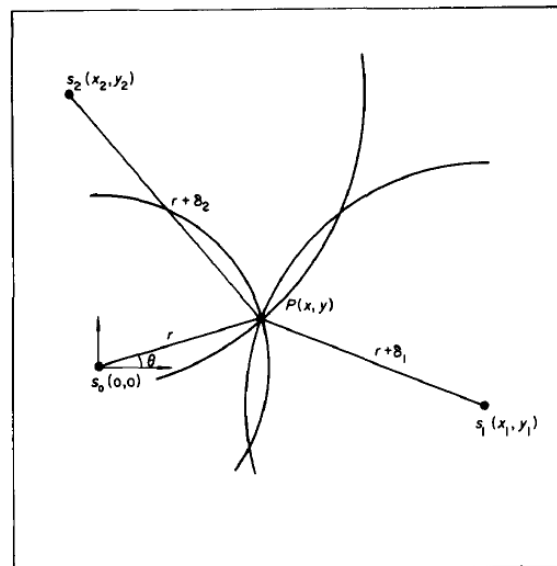


Figure 8: Source location diagram as depicted by Tobias [32]

Acoustic Emissions are produced any time there is a sudden change of energy within a medium, whether it be due to plastic deformation, friction, the creation of new surfaces in fracture or impact [2]. Each of these drivers produces distinct characteristics in an AE

signal amplitude, frequency, duration, etc. This thesis will be focusing on high-amplitude AE produced by fracture in ductile metals. Research has shown that the vast majority of these AE signals can be captured within the range of 100-500kHz frequency [2].

Figure 10 depicts the various characteristics associated with the capture of an AE signal [33]. The "primitive", as it is called, AE signal at the source location is an oscillating motion of the particles of the medium which travels through the medium at a constant speed and is captured by appropriate sensors that typically convert displacement, velocity or acceleration time series to voltage series. An AE Hit is the entire duration of an AE signal recorded by a sensor. The hit rate, as discussed by Ozevin et al [34] and displayed in Figure 9, can be used to monitor material relaxation due to a fracture event [35]. The Threshold is a minimum amplitude which the signal must exceed to be considered an AE hit—this is often utilized to eliminate false AE activity due to environment effects and system noise. The Duration of the signal is the length of time in which pulses in the AE signal occur above the threshold amplitude whereas Rise time is the length of time in required to reach the signal's maximum amplitude. Related AE features are the Counts, which are the number of AE signal pulses that exceed the threshold amplitude.

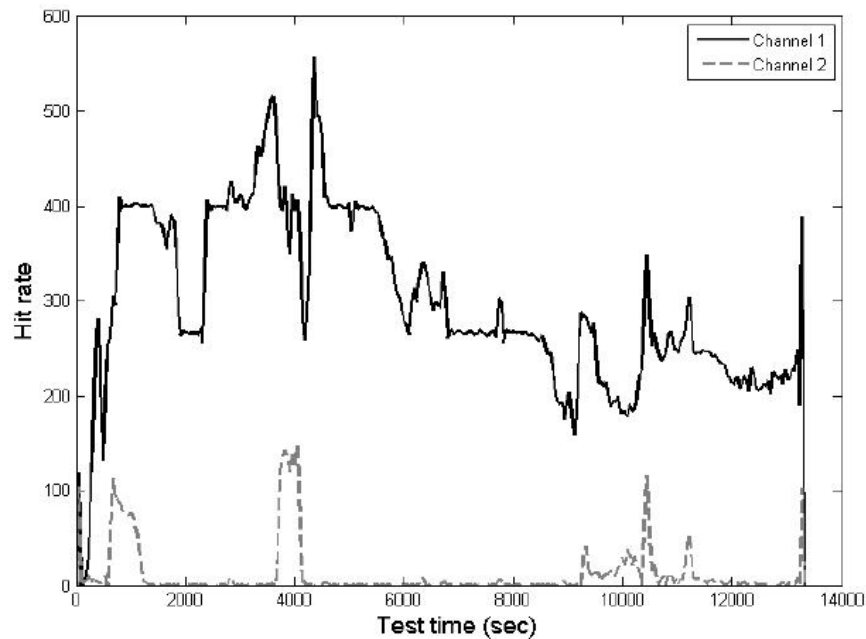


Figure 9: AE hit rate during a fatigue loading fracture experiment [34]

The Energy of an AE signal is the total area under the signal and is equal to one half of the theoretically symmetric signal as shown below in gray. A secondary energy parameter, known as the Absolute Energy, exists which is the absolute area under the entire curve of the AE signal. A standard AE testing setup consists of a loaded test specimen with piezoelectric sensors affixed to one or more of the exterior surfaces. The sensor signals are passed through a pre-amplifier before being analyzed by the Data Acquisition (DAQ) unit.



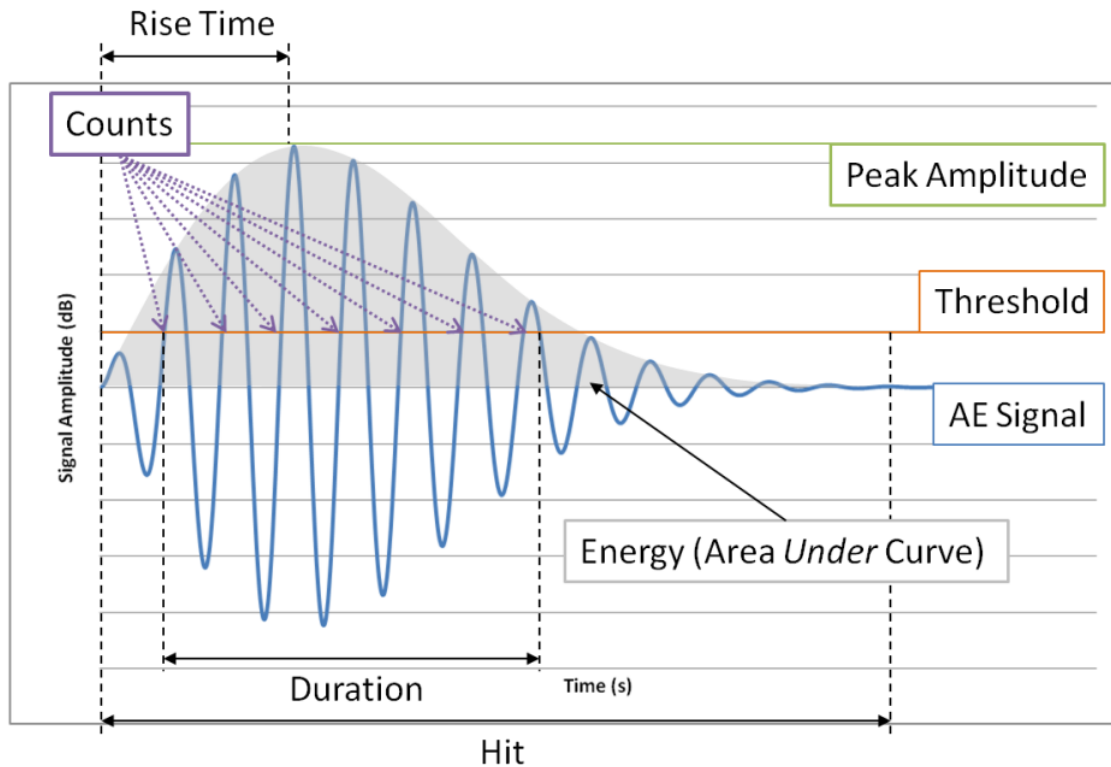


Figure 10: Characteristics of an AE signal

The DAQ samples and processes the signal at a preset rate and applies filtering if it is desired by the user. The amplified, processed and filtered signal now passes on to the computer software interface which calculates the duration, rise time, counts, etc.

Additionally, if multiple sensors are utilized, the software may pinpoint and map where, on the specimen, the AE activity originated [3].

Early work in the late 1970's with AE was strictly based on the artifact itself—that is AE was monitored as damage was occurring [36]. Fifteen years later, links were developed between the production of AEs and the Stress Intensity Factor and Crack Growth Rate [37, 38]. Shortly after this, the characteristics of where damage began in a structure was

determined through AE testing [39]. This has led to the modern-day applications of AE for damage prediction through a correlation between the rate and intensity of AE emissions based upon the phase of damage [40, 41]. Recent research considers the effects of the sensor itself, and the link between the sensor and the material, on the captured AE. Moreover, research into the interconnectivity between AE and other advanced metrology techniques have been explored. Finally, research into the production and propagation of AE due to a sudden release of stresses in and the prediction of crack growth from AE analysis forms a ground for which this thesis begins. These state-of-the-art methods have been researched by Sause [6], Vanniamparambil et al. [3], Andreykiv et al. [42], and Yu et al. [41] respectively.

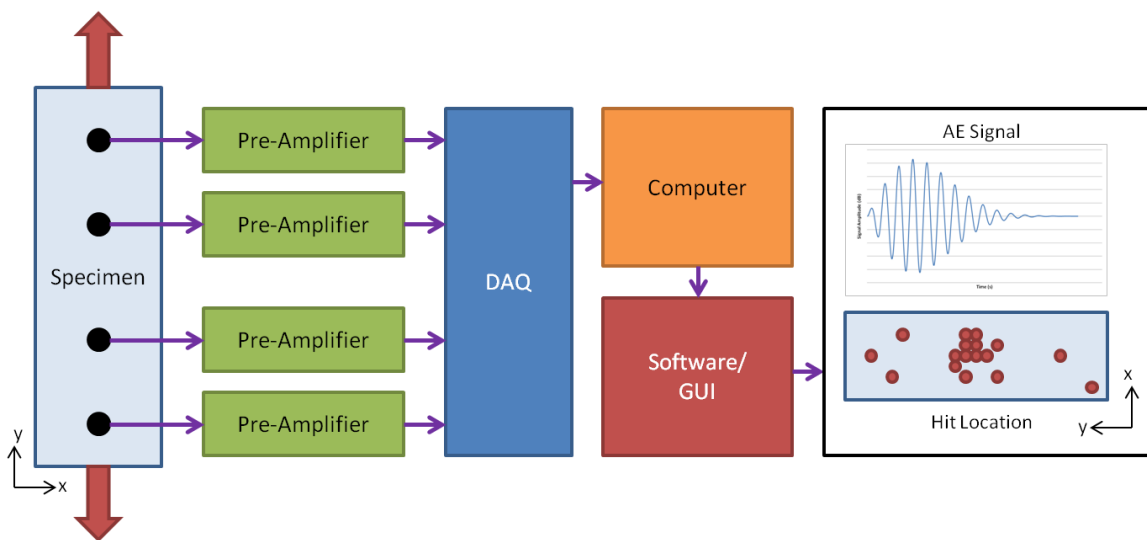


**Figure 11: Acoustic Emissions testing setup in a laboratory setting**

### *3.2 Digital Image Correlation in Fracture*

Digital Image Correlation (DIC) is a form of in situ non-contact optical deformation and strain measurement method, seen in Figure 12, based upon images taken by a set of stereo digital cameras [43]. An indicative example of DIC is the software program ARAMIS (developed by GOM Optical Gauging Techniques) which distinguishes surface details of the specimen, and then correlates coordinates to the pixels of the image. As deformation occurs additional images are captured, the same surface details are identified, and new coordinates are applied. In cases where few surface details exist, such as smooth cut or polished homogenous materials like metals and painted surfaces, pseudo surface details must be applied. Depending upon the scale of the specimen, the pseudo surface details can range from a fine micron-scale powder applied to an area where grain structure is being observed, to a speckled high-contrast nondeterministic paint pattern or dot pattern for most laboratory cases. In special cases where an entire structure such as a bridge may be monitored, several-meter diameter dots may be applied [43].

DIC is unique in the sense that it can be applied to high-speed deformation for strain and vibrational analysis, and high-temperature applications due to its inherent remoteness to the specimen in testing. Additionally, the specimen can move and rotate rigidly with respect to the DIC cameras as long as the surface details are still present in the field-of-view. This is because the computed displacements are with respect to one another, not the surrounding environment; this allows for the application of DIC to crash and long-term testing where the cameras may be moved or removed completely in between image captures [44]. Figure 13 shows a typical DIC test setup.

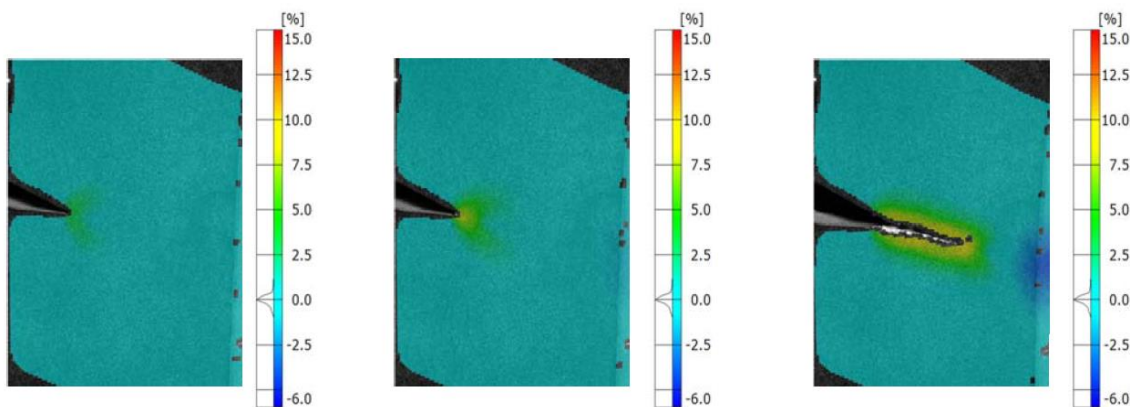


Figure 12: DIC utilized for capturing strain accumulation in a crack growth simulation

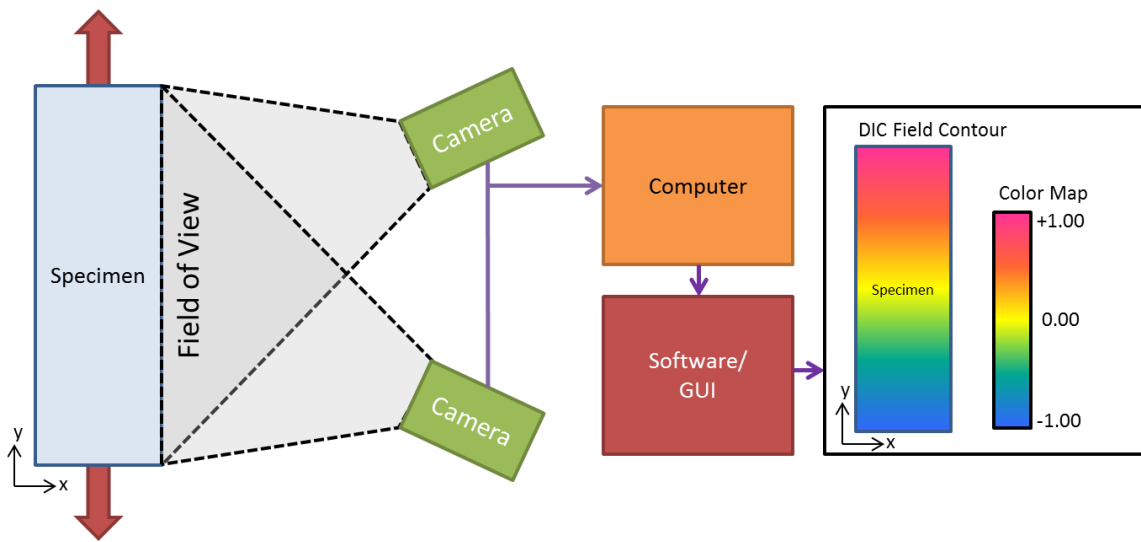
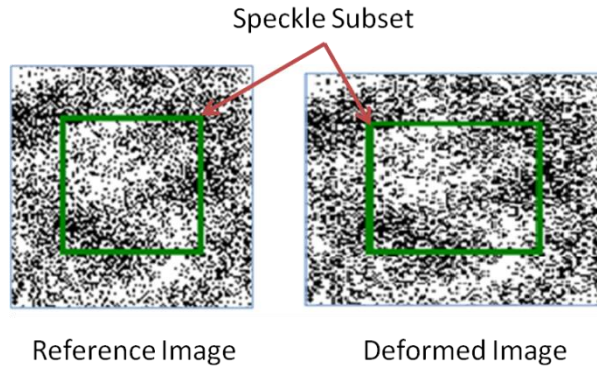


Figure 13: DIC system setup in a laboratory setting

The DIC algorithm functions by tracking and relating an array of physical points, on the specimen surface, from a given frame to a reference image by mapping square subsets of pixels in a speckled pattern applied to the specimen [3]. Figure 14 shows how a square subset may change from the reference image to a deformed frame.



**Figure 14: Tracking a speckle subset through specimen deformation**

The average grayscale intensity of a subset is computed in the reference image and compared to that of the deformed image by solving for the displacements where, in the 2D case as shown by equation (E3.1), x- and y-displacements are  $u$  and  $v$ , respectively [45].

$$C(u, v) = \sum_i \sum_j I_R(r_i, s_i) I_D(r_i + u_A, s_i + v_A) \quad (\text{E3.1})$$

$$u_A = u + \frac{\partial u}{\partial r} \cdot (r_A - r_C) + \frac{\partial u}{\partial s} \cdot (s_A - s_C) \quad (\text{E3.2})$$

$$v_A = v + \frac{\partial v}{\partial r} \cdot (r_A - r_C) + \frac{\partial v}{\partial s} \cdot (s_A - s_C) \quad (\text{E3.3})$$

Where  $I_R$  and  $I_D$  are the grayscale intensities of the subset of pixels in the reference and deformed images, respectively,  $u$  and  $v$  are the displacements of the center point, located at the point  $(r_C, s_C)$ , of the subset of pixels, and  $u_A$  and  $v_A$  are the displacements of an arbitrary point, located at  $(r_A, s_A)$ , within the subset. After solving for the displacements, strain can be computed using standard elasto-plastic strain definitions.

Key benefits of DIC is its inherent ability to monitor strain and displacement without damaging the equipment, which is often an issue in fracture studies which use strain gauges, and its ability to capture full-field information in virtually every direction instead of being limited to a specific point and set of directions as with strain gauges.

Additionally, DIC offers the capability of integration into other forms of NDT such as AE and UT [3], and integration into Finite Element Analysis (FEA) to provide data-driven simulation and realistic fracture and damage parameters [4, 46]. Recent research has been investigating the use of DIC to verify fracture laws and propose integrated DIC (I-DIC) and DIC-tuned damage parameters [47, 48] for use in simulations as well as for verifying and comparing the simulation to experimental data [49]. The realistic damage parameter extraction discussed in Chapter 5 of this thesis is based on the recent works of Gain [46] and Paulino et al [4] where DIC is implemented during a fracture experiment with the specific intention of extracting a function optimized Traction Separation Law for use in a Cohesive Zone Model..

## Chapter 4: Crack Growth Experimentation

The current chapter describes the difference between the forward and inverse acoustic emission problem and then continues to explain the general approach to develop a novel approach to solving the forward acoustic emission problem through the merging of experimental results, the extraction of realistic fracture parameters and the application of Cohesive Zone Modeling in static-driven dynamic simulations. There have been approaches to the forward problem (simulation of acoustic emissions) in the past; however the issue residing with these simulations is the way that the energy release was applied to the model: An artificial displacement is applied to a node over the course of an assumed time frame where, either 1) the displacement on the node is held, 2) the displacement on the node is reverted back to the original state, or 3) the node is released and the model is allowed to resonate naturally [6]. The problem here resides in the fact that for each of these cases, an energy model is forced upon the body and the response captured in the simulation is not necessarily the response of the body due to the extension of a crack, but rather the response due to the applied energy model. The technique proposed in this chapter was designed to eliminate the user-created forced energy function and replace it with a model derived directly from the energy-balance associated with quasi-static crack growth .

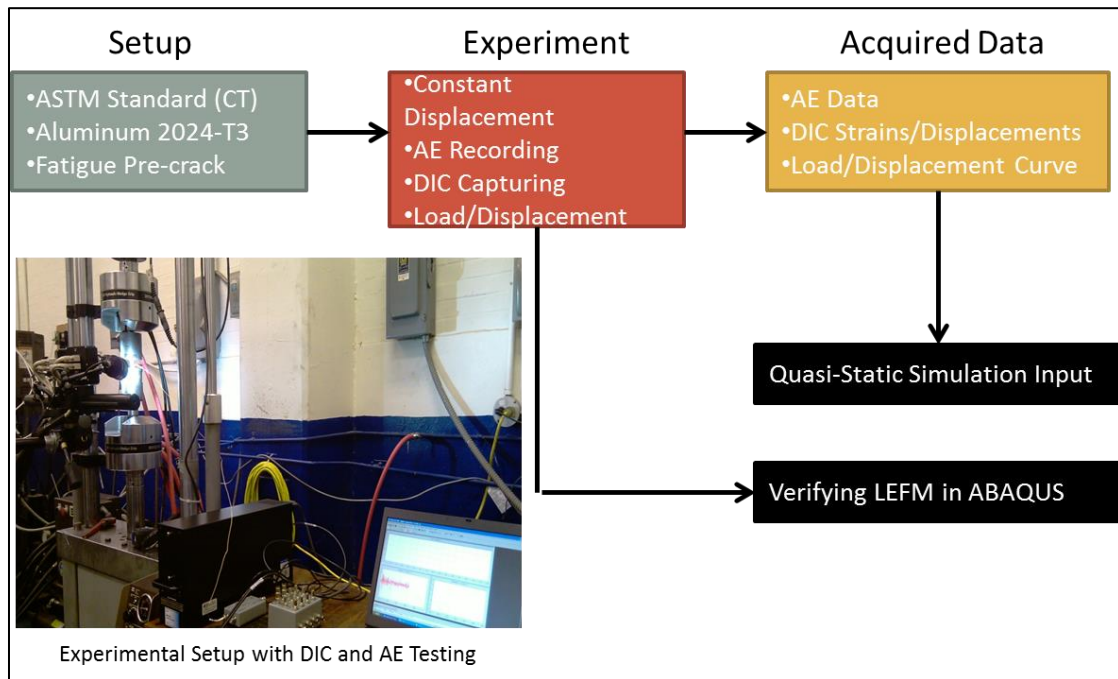


Figure 15: A brief mapping of the Chapter 4 layout

#### 4.1 The Forward Problem of Acoustic Emissions

The forward problem of acoustic emissions considers the source of what actually produces elastic waves and attempts to predict the production and propagation of acoustic waves through a medium, whereas the reverse problem monitors the medium for acoustic activity and attempts to locate and characterize the source of the emission. The first step to understanding the forward problem is to understand the reverse problem; that is, one must first understand the phenomena is producing the elastic waves that are being captured before one can attempt to recreate them. Looking at the reverse problem in strictly macro-scale, one can consider the sound which a tree branch makes as it fails: A distinct crackling and popping sound can be heard as the branch fractures and fails.



An identical phenomenon occurs in brittle and ductile materials in the micro-scale as individual bonds between molecules are broken. In an experimental setting, this is typically captured using piezoelectric sensors which have been securely mounted to the test specimen. The forward acoustic emission problem must take different fracture modes, geometry, loading, material, environmental conditions and practically endless other variables into account in order to reproduce the acoustic signals captured during the experiment. The experiments designed for AE capture are meticulously crafted in an attempt to control as many of these parameters as possible and eliminate the variability produced in the system.

In this context, a Mode I fracture experiment was carefully designed to control the accumulation of strain around a fatigue pre-crack and monitor the crack growth process in a Compact Tension specimen of Aluminum Alloy 2024-T3. Acoustic Emission hits and waveforms were captured as loading was increased and crack growth occurred.

Simultaneously, stereo digital cameras captured images that were processed for Digital Image Correlation, yielding full-field strain and displacement data. This experimental information, reported in [3] is used in this thesis to optimize a set of damage parameters for use in Finite Element Analysis (FEA) simulations.

The commercially available ABAQUS software package is utilized to develop quasi-static FEA simulations based on the specimen geometry, material properties and experimental loading. A Cohesive Zone Model (CZM) will be implemented along a horizontal plane located at the tip of the specimen notch. The realistic damage parameters which drive the CZM are extracted from the experimental DIC data by mapping points on the strain and displacement contours, later used to optimize a stress-separation function to

the data points. The nodal and elemental stress, strain and displacement information at specific equilibrium points during the simulation, before and after crack growth, will be utilized as inputs to a dynamic Boundary Value Problem (BVP) which will yield the transient solution of the system from one equilibrium point to another. Within this solution at hand the production and propagation of Acoustic Emissions created by the sudden release of energy is achieved.

#### *4.2 Experimental Setup*

For completeness details on the relevant experimental setup are mentioned herein. The test was based on the ASTM standard E399-05 [50] which utilizes a compact tension specimen for Mode I fracture during tensile testing where loading was applied as a constant velocity displacement. The compact tension specimen was designed to follow the ASTM399-05 guideline for dimensions computed based on the width of the specimen seen in Figure 16. Several additional conditions were taken into consideration when designing the compact tension specimen: The size/capability of the load frame, the size of the holes, and viewing area/resolution of the DIC system. It should be noted that the diameter of the holes was chosen to be 12.72mm to directly match up with a 0.5 inch diameter steel bar to be used to pin the specimen to the load frame. Based around this parameter, the width,  $W$ , was chosen to be 50.8mm resulting in the remainder of the dimension as follow, and as shown in Table 2: The outside dimensions were 63.00 mm wide by 61.00 mm tall with two 12.72 mm diameter holes, for loading the specimen, located 50.80 mm from the non-notched side and 14 mm above and below the symmetric centerline.

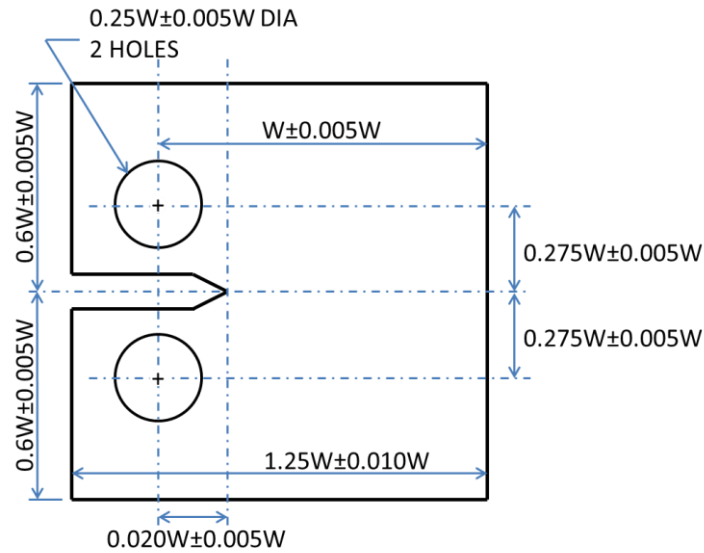


Figure 16: ASTM E399-05 Compact Tension Specimen Recommended Dimensions

Table 2: Compact Tension Specimen Dimensions based upon ASTM E399-05

Dimension	ASTM Dimension	Dimension Range	Chosen Dimension
<b>Width, W</b>	--	--	50.80 mm
<b>Specimen Width</b>	1.25W±0.010W	62.992 – 64.008 mm	63.00 mm
<b>Specimen Height (From line of symmetry)</b>	0.6W±0.005W	30.226 – 30.734 mm	30.50 mm
<b>Hole, Distance from line of symmetry</b>	0.275±0.005W	13.716 – 14.224 mm	14.00 mm
<b>Hole, Diameter</b>	0.25±0.005W	12.447 – 12.954 mm	12.72 mm
<b>Distance from holes to starter notch tip</b>	0.25±0.005W	9.906 – 10.414 mm	10.20 mm
<b>Parallelism and Perpendicularity Tolerance</b>	0.002W	0.102 mm	--
<b>Starter notch point location symmetry tolerance</b>	0.005W	0.254mm	--

Additional notes, as specified in the standard, require that all surfaces be parallel and/or perpendicular to 0.102 mm and the point of the starter notch tip be located within 0.254mm of equal distance from the top and bottom surfaces. The dimensions of the notch are 3.175mm high (1.588 mm above and below the symmetric center line) with length, including the angled tip, of 22.4 mm. A fatigue pre-crack of approximately 3 mm was created using cyclic loading between 600 N and 6000 N at a rate of 10 Hz following the ASTM Standard E1290-08 [51] for fatigue crack growth. The purpose of this pre-crack was to help guide the crack extension in a horizontal direction to keep with the assumption that the crack will propagate in pure Mode I crack extension and to ensure there will be an area of stable crack growth when crack propagation begins. Loading was applied through a constant displacement of 0.5 mm/minute, as shown in Figure 17, in the negative y-direction at the bottom hole, which was pinned and allowed to rotate about the Z axis but not translate in the X direction [3]. Similarly, the top whole was fixed in the X, Y and Z direction but allowed to rotate about the Z axis as shown in Figure 18. The holes were pinned to the test stand apparatus using 0.500” steel rods which, when compared to the shear and elastic moduli of Aluminum alloy 2024-T3, and the cross-sectional area of the steel rod to the area of applied load on the specimen, can be considered rigid and have negligible effect on the transfer of the displacement loading from the .load frame to the test sample.

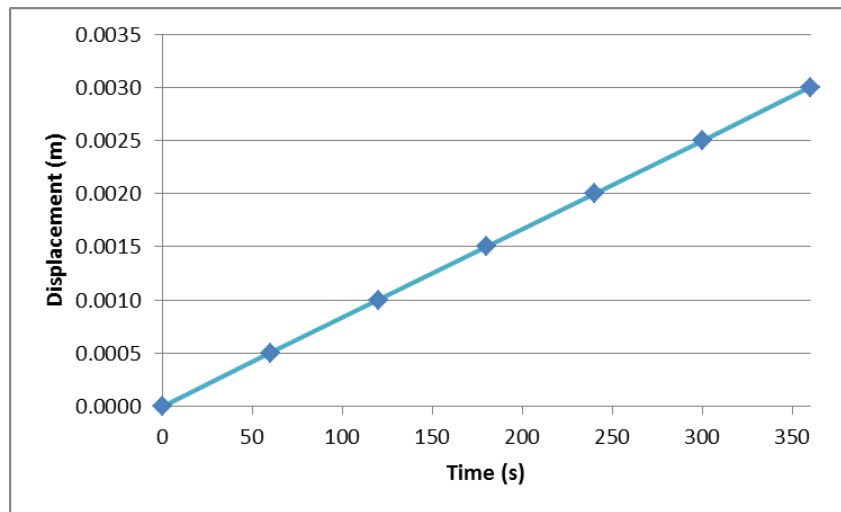


Figure 17: Displacement Loading for Mode I Fracture Experiment

The load frame used for this experiment is a Material Test System (MTS) set up with steel clevises as specified in ASTM Standard E399-05 Figure 2.2 and associated notes [50] .

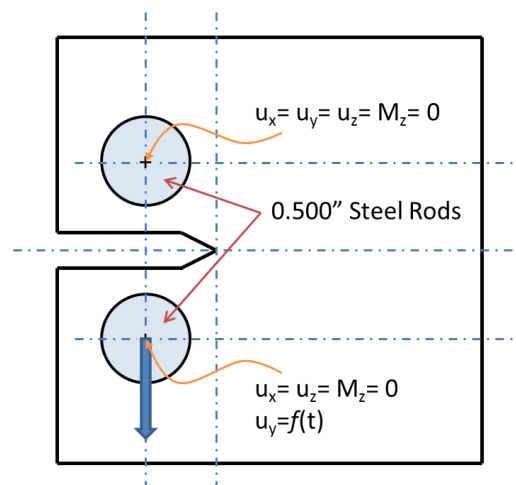
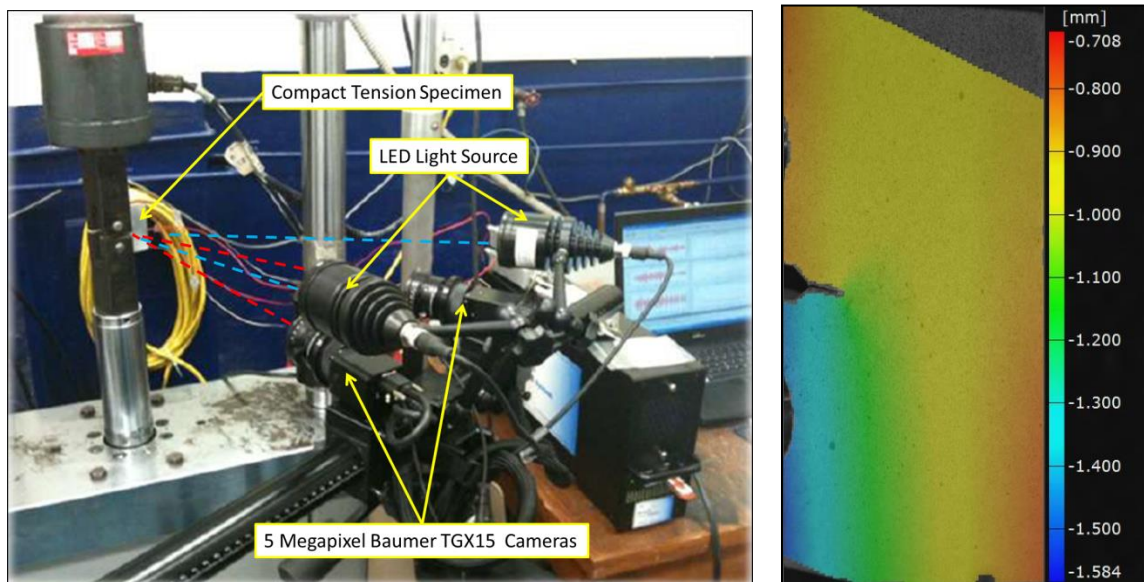


Figure 18: Boundary Conditions for Crack-Growth Experiment

Digital Image Correlation captured the full-field strains and displacements during the experiment using a GOM ARAMIS 3D DIC system which utilized stereo 5 Megapixel Baumer TGX15 [3] black and white digital cameras at a capture rate of 1Hz. The DIC system was carefully calibrated for the experimental setup to achieve displacement accuracy of 3 microns and strain accuracy of 50-100 microstrain with a field of view of 65 x 55mm by placing the cameras 485mm from the specimen with a separation of 176mm which yields the manufacturer's recommended camera angle of 25° [3].



**Figure 19: (Left) DIC camera setup during the fracture experiment**  
**Figure 20: (Right) DIC strain capture at t=60s during the fracture experiment**

A four-channel acoustic emission acquisition system (DiST) and software (winAE) by Physical Acoustics Corporation was used, with one piezoelectric transducer (pico) per channel, to capture out-of-plane elastic stress waves (i.e. Acoustic Emissions) due to

crack growth. The four identical piezoelectric sensors have an operating frequency range of 200-750kHz with a peak frequency at 500kHz [3]. Each piezoelectric sensor was pre-amplified by individual 40dB gain amplifiers and sampled at a rate of 10MHz. Two additional parameters, load and applied displacement, were captured by the MTS test stand and will be utilized to help quantify and verify the theoretical results captured during the quasi-static ABAQUS simulation. The results of the MTS data are plotted below.

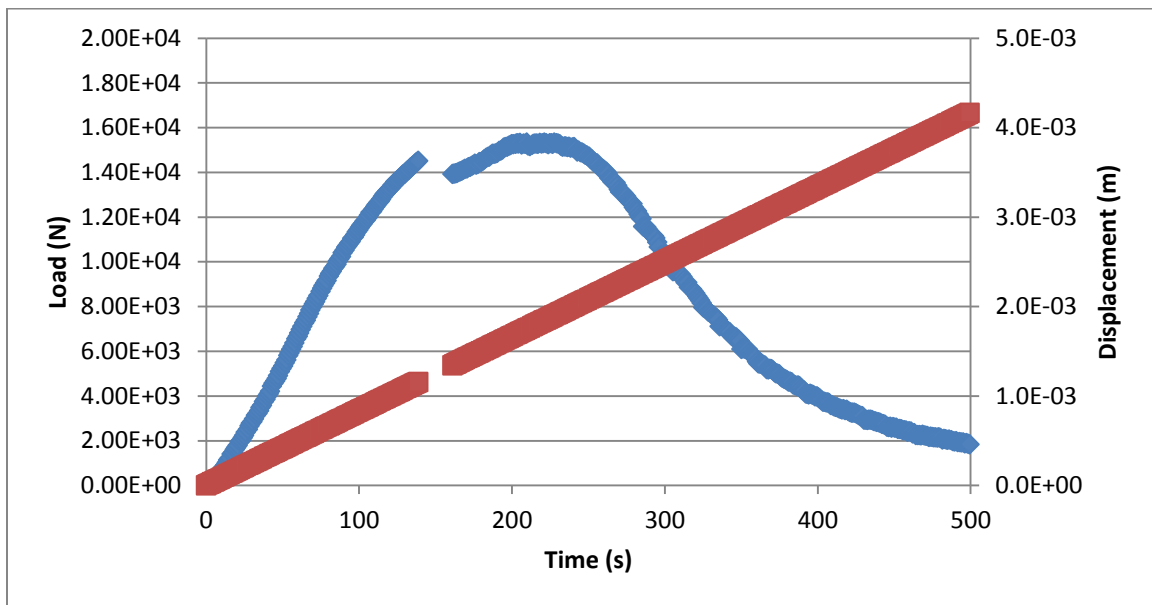


Figure 21: MTS displacement and load data collected during the mode I fracture experiment

The MTS and DIC systems are tied together through an Analog to Digital (AD) controller which captures the load and displacement data from the MTS machine and uses it, if desired, to trigger the capture of DIC frames. During the experiment, a short-term

malfunction in the AD controller resulted in a loss of MTS and DIC data between experiment times of 138s and 161s, however the MTS loading scheme was uninterrupted. The effects of this may be seen in Figure 21 where a section of load and displacement data is interrupted.



## Chapter 5: Data-Driven Simulations of Crack Growth Propagation

This chapter will discuss the use of ABAQUS for modeling both static and quasi-static fracture mechanics. In the first case a continuum body with a preexisting crack will be loaded but the crack will not be allowed to propagate. Conversely, in the second case, a continuum body with a preexisting crack will be loaded and allowed to propagate in a controlled manner using quasi-static loading and cohesive zone modeling. A compact tension specimen with a pre-crack, which is equivalent to the experimental pre-crack, will be loaded to verify that the model matches the theoretical Linear Elastic Fracture Mechanics (LEFM) solutions of near crack-tip stress, strain and displacement fields.

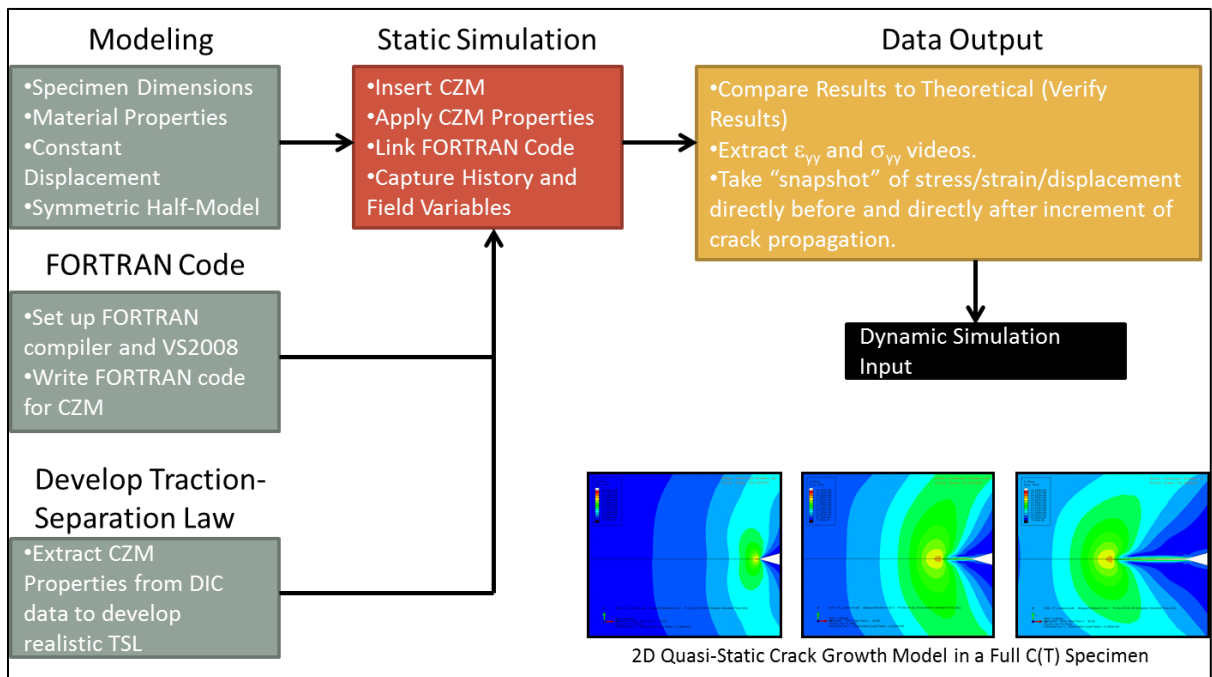


Figure 22: A brief mapping of the Chapter 5 layout

Ensuring the model matches the theoretical solution of near crack-tip fracture mechanics will ensure that the simulation is adhering to the underlying physical and mathematical constraints of the fracture problem. After the LEFM solution has been verified, a new simulation with an integrated FORTRAN-driven Cohesive Zone Model will be developed to test the quasi-static crack growth model. In this chapter, the development and integration of user-generated FORTRAN code and elements (UEL) into an ABAQUS simulation will be discussed in detail.

### *5.1 High-Performance Computational Setup*

The majority of models and simulations discussed in this thesis are relatively large in terms of the number of elements and number of Degrees of Freedom (DOF). The number of DOF directly correlates to the number of equations which must simultaneously be solved for by the solver algorithm for each time increment in the simulation. Although the number and clock speed of processing cores will directly affect the speed at which a simulation will complete, the major bottleneck comes from the availability of Random Access Memory (RAM) for the compute node to store variable values during a solver iteration. It is not uncommon to find workstations with dual or quad-core processors and 8Gb of RAM. In fact, the node utilized for modeling and setting up the simulations is exactly that: a workstation with a quad-core AMD Athlon X2 645 3.1GHz processor and 8Gb of DDR3 RAM. This workstation was capable of handling the simulation of a model with no more than five-hundred thousand elements and three million DOFs. Additionally, depending upon the length of the simulation, the length of the time increments and the size of the model, a complete simulation on this node could take several days to

complete. To alleviate the computational strain on this node, and improve overall performance of simulations, a small compute cluster was assembled specifically for running ABAQUS models.

The compute cluster is built with eight nodes running Red Hat Enterprise Linux Server 5.7 (OS Version 2.6.18-274.el5) operating system and interconnected by ten-gigabit Ethernet. Each node is comprised of two quad-core Intel Xeon 206C2 2.4Ghz processors and 24Gb of DDR3 RAM. Each node shared storage on a 6Tb (4Tb accessible due to the RAID scheme) Buffalo TeraStation III iSCSI Network Attached Storage (NAS) unit which was interconnected via 10-Gb Ethernet similarly to each node's interconnectivity. Each node was accessible remotely through a Secure Shell (SSH) and File Transfer Protocol (FTP) client.

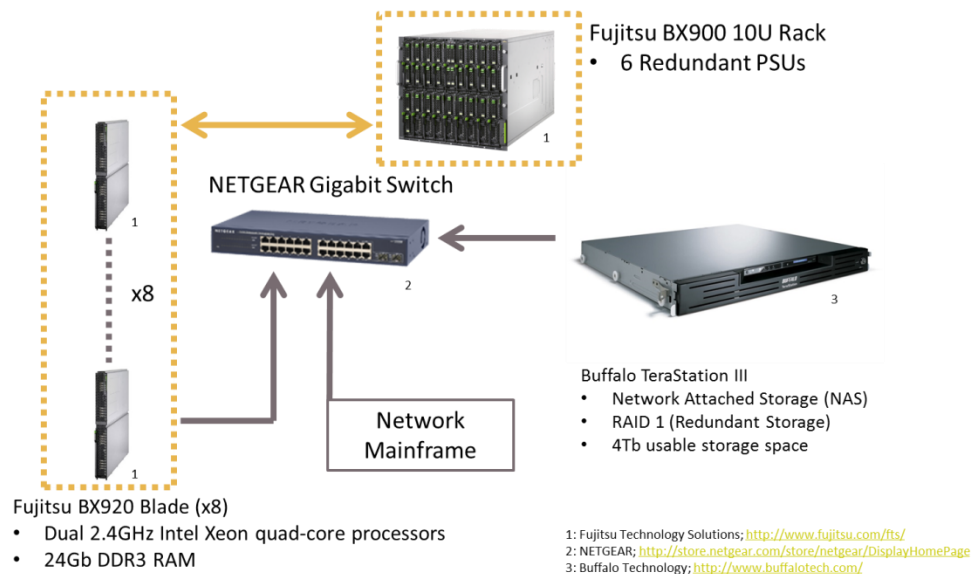


**Figure 23: Generalized compute cluster architecture**

Additionally each node was equipped with a remote desktop connection, using the open source software TightVNC, which allowed for results to be viewed and manipulated directly on the node as opposed to transferring the output database back to the local node.

### *5.2 Verification of Linear Elastic Fracture Mechanics in ABAQUS*

Credability of the ABAQUS model is ensured by replicating the Linear Elastic Fracture Mechanics (LEFM) equations discussed in Chapter 2. The model begins as a full two-dimensional Compact Tension, C(T), specimen with identical dimensions as the experiment discussed in Chapter 4 including a 3.0 mm pre-crack which is assumed to pass through the entire thickness of the specimen. The pre-crack is applied to the ABAQUS model as a non-conjoined seam through the interactions menu. It is important to note that crack advancement was disabled for this simulation. Loading was applied, as shown in Figure 24, as a y-direction point load of 1000N in the center of a rigid inclusion located where the upper hole and pin would be located in the specimen. A similar technique was used to pin the bottom hole of the specimen in the center of an identical rigid inclusion. This technique allows for the rotation of the specimen, around what would be the equivalent of the steel pin in the experiment, without introducing contact interactions or producing localized plasticity.

A global seed size of 1.00 mm was used with local seed sizes ranging from 0.50 mm around the outermost ring surrounding the pre-crack, 0.05 mm around the inside ring surrounding the pre-crack, and a biased seed size of 0.05 mm at the ends and 0.01mm in the middle of the pre-crack as shown in Figure 25.

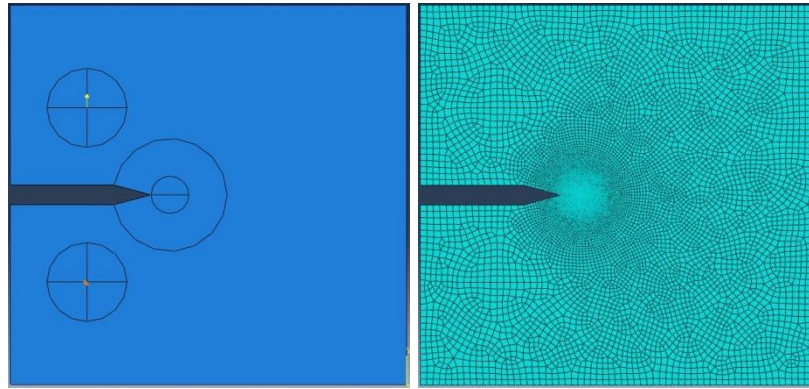


Figure 24: (Left) 2D LEFM verification C(T) specimen with applied loading and boundary conditions  
Figure 25: (Right) 2D LEFM verification C(T) specimen mesh

The following results were captured in the vicinity of the crack tip, with a field view of approximately 1.0 mm square, where the image to the left is the MATLAB plot of the LEFM solution, and the image on the right is the ABAQUS solution.

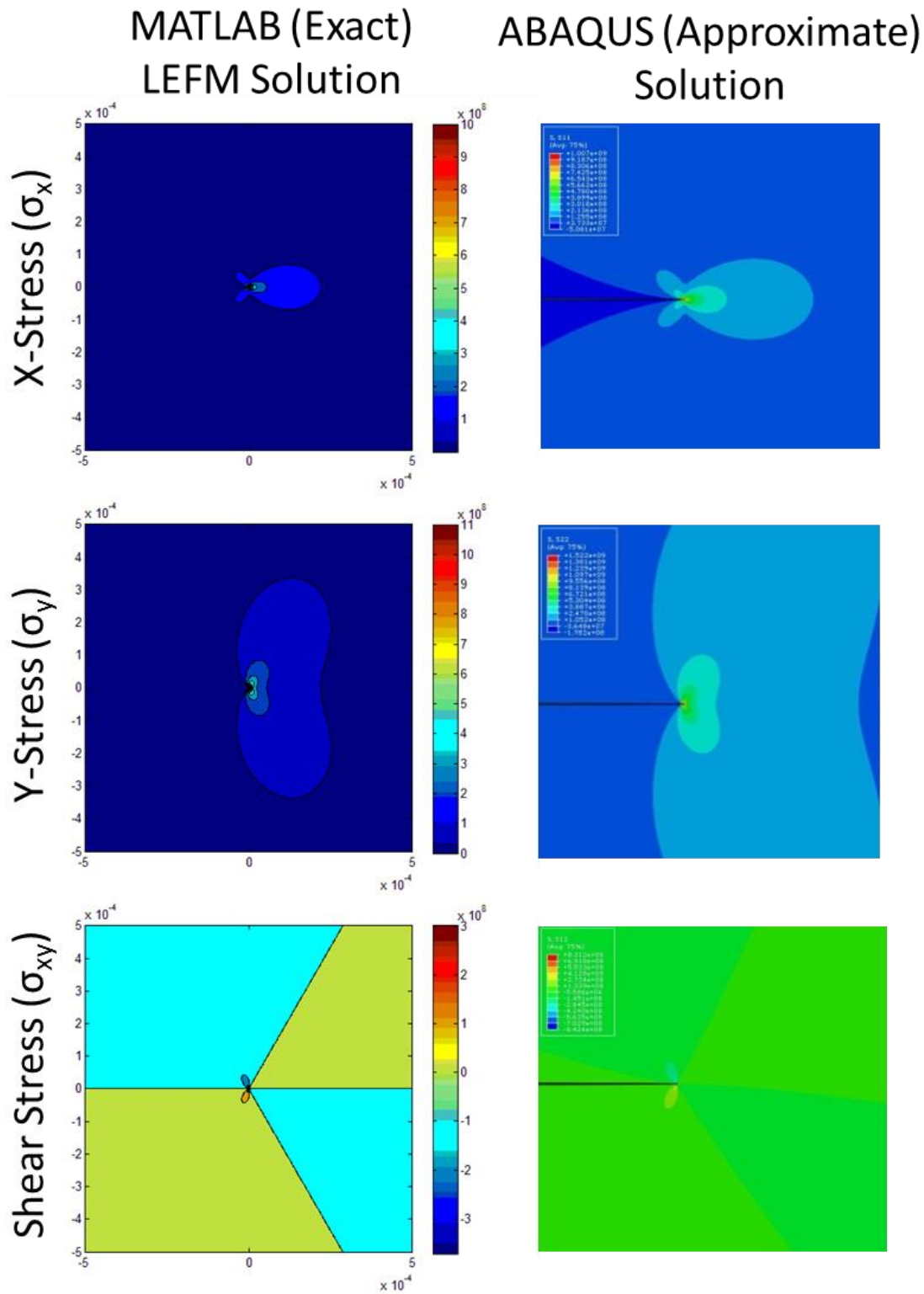


Figure 26: Comparison of the 2D MATLAB (Left) solution based upon LEFM equations and ABAQUS (Approximate) 2D solutions for: a) X-Stress b) Y-Stress, and c) Shear Stress fields around a crack tip.

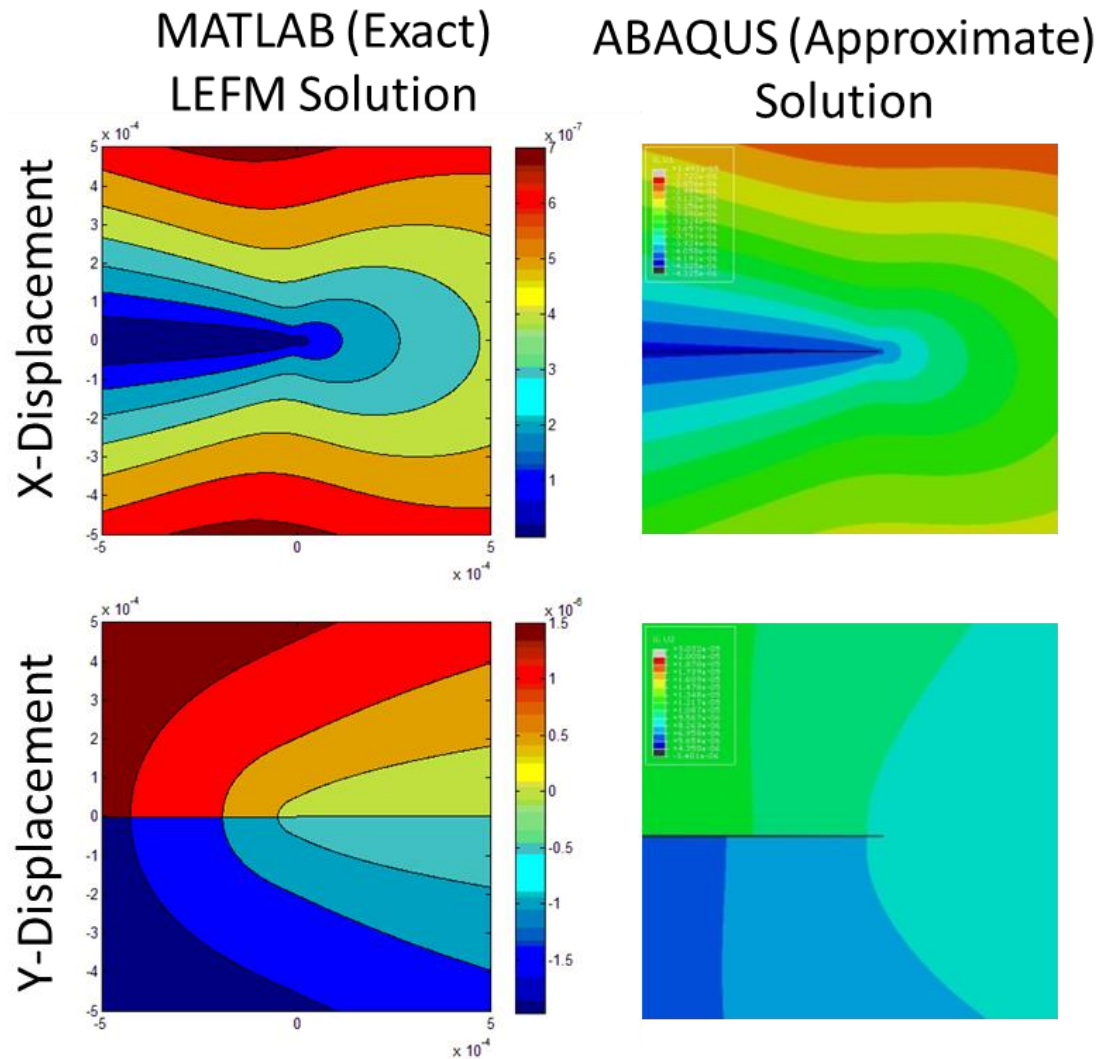


Figure 27: Comparison of the 2D MATLAB (Left) solution based upon LEFM equations and ABAQUS (Approximate) 2D solutions for: a) X-Displacement, and b) Y-Displacement fields around a crack tip.

The results show an exact geographical match between the theoretical LEFM and ABAQUS approximate solutions thus the stress and displacement fields in the vicinity of the crack tip have been verified to be realistic and accurate in the simulation.

### 5.3 Development of a CZM FORTRAN code

ABAQUS offers the capability to communicate with user-generated code to control over fifty aspects of a simulation which can range from Nodal Displacement Control (DISP), User-defined materials (UMAT), user-computed field outputs (UFIELD) and User Elements (UEL) [52]. This section will discuss the development of a FORTRAN-based Cohesive Zone Element (CZE) user element (UEL). There is a set of arrays which will be passed into the UEL code by ABAQUS to be used for computing, defining and updating output arrays. Table 3 and Table 4 show lists of ABAQUS defined inputs that will be used and required in the UEL code whereas Table 5 shows a list of arrays which will be developed in the UEL code and passed back to ABAQUS for use in the solver algorithm.

**Table 3: Input arrays passed from ABAQUS to FORTRAN for the UEL code [52]**

<b>UEL Input Array</b>	<b>Description</b>
U	Nodal Displacements
PROPS	Floating-point constants which have been defined in the input file.
JPROPS	Integer constants which have been defined in the input file.
PARAMS	Parameters associated with the solution procedure as indicated in the LFLAGS array.
LFLAGS	Solution parameters and requirements for element calculations.



**Table 4: Input scalars passed from ABAQUS to FORTRAN for the UEL [31]**

<b>UEL Input Scalars</b>	<b>Description</b>
NDOFEL	Number of degrees of freedom
NPROPS	Number of floating-point constants which have been defined in the input file.
NJPROPS	Number of integer constants which have been defined in the input file.
NSVARS	Number of state variables.
MCRD	Maximum number of coordinates required at a node point.

**Table 5: Output arrays passed from the FORTRAN UEL code to ABAQUS [31]**

<b>UEL Output Arrays</b>	<b>Description</b>
RHS	Contributions of elements to the right-hand side of the global system of equations.
AMATRIX	Contributions of elements to the stiffness matrix of the global system of equations.
SVARS	Solution-dependent state variables.
ENERGY	Kinetic, Elastic Strain, Creep Dissipation, Plastic Dissipation, Viscous Dissipation, Artificial Strain and Electrostatic Energy.

Both the 2D and 3D cohesive elements are zero-thickness elements which are either quadratic line elements for the 2D case or quadratic planar elements in the 3D case. The mathematical concepts and progression of the UEL code is identical for both 2D and 3D cohesive elements. The following derivation [10] will cover the 3D CZE case with nine integration points as shown in Figure 29.

After the initialization of the FORTRAN code as specified by the ABAQUS User's Manual, each vector and matrix used in the code must be initialized and dimensioned using the function DIMENSION where the vectors and matrices are listed, separated by commas, as follows

*DIMENSION*  $vector(i)$ ,  $matrix(j,k)$ , ...

where  $vector$  is the name of an  $i$ -length vector and  $matrix$  is the name of a  $j \times k$  dimension matrix. Real input properties from the input file are brought into the code by assigning the values of  $PROPS(i)$  and  $JPROPS(i)$  to variables.

The code checks the number of nodes and state variables to ensure they are appropriate for the number of integration points selected. If either number is found to be incorrect, the simulation is terminated and an error message is printed to the message file explaining the cause of the termination.

The following mathematical procedure, which is based on the work done by Stefanie Feih in 2005 [10], will discuss the computation of separation at integration points within the element. Each element has forty-eight degrees of freedom (DOF), x, y and z displacement at each of the upper and lower eight nodes. These DOFs are arranged into a matrix as follows:

$$u_N = \begin{bmatrix} -d_1^x & 0 & 0 & \dots & 0 & 0 & 0 & d_9^x & 0 & 0 & \dots & 0 & 0 & 0 \\ 0 & -d_1^y & 0 & \dots & 0 & 0 & 0 & 0 & d_9^y & 0 & \dots & 0 & 0 & 0 \\ 0 & 0 & -d_1^z & \dots & 0 & 0 & 0 & 0 & 0 & d_9^z & \dots & 0 & 0 & 0 \\ \vdots & \vdots & \vdots & \ddots & \vdots & \vdots & \vdots & \vdots & \vdots & \vdots & \ddots & \vdots & \vdots & \vdots \\ 0 & 0 & 0 & \dots & -d_8^x & 0 & 0 & 0 & 0 & 0 & \dots & d_{16}^x & 0 & 0 \\ 0 & 0 & 0 & \dots & 0 & -d_8^y & 0 & 0 & 0 & 0 & \dots & 0 & d_{16}^y & 0 \\ 0 & 0 & 0 & \dots & 0 & 0 & -d_8^z & 0 & 0 & 0 & \dots & 0 & 0 & d_{16}^z \end{bmatrix} \quad \text{E5.1}$$

which is equivalent to the ordered vector of DOFs multiplied by two consecutive 24x24 identity matrices, the first of which is negative and denoted by  $\Phi$ .

$$u_N = \Phi d_N = [I_{24} \quad I_{24}] \{d_1^x, d_1^y, d_1^z, \dots, d_{16}^x, d_{16}^y, d_{16}^z\}^T \quad \text{E5.2}$$

Eight node pairs exist where the nodes of the upper CZE face initially intersects with the nodes of the lower CZE face as shown in Figure 28. For each node pair there exists three separation terms—one for each principal direction.

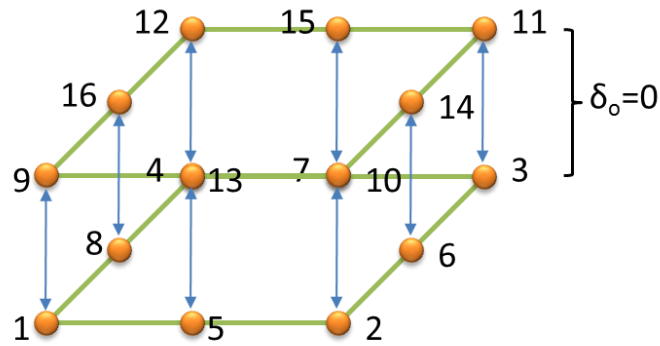


Figure 28: Cohesive Zone Element node pairs

These are signified by  $\delta$  and can be written as follows:

$$\delta(\zeta, \eta) = \begin{bmatrix} \delta_x(\zeta, \eta) \\ \delta_y(\zeta, \eta) \\ \delta_z(\zeta, \eta) \end{bmatrix} = \mathbf{S}(\zeta, \eta) u_N \quad \text{E5.3}$$

Where  $\zeta$  and  $\eta$  are the local coordinates of the element, as shown in Figure 29, and range in value from -1 to 1 with the center of the undeformed element marking the origin of the  $\zeta$ - $\eta$  plane.

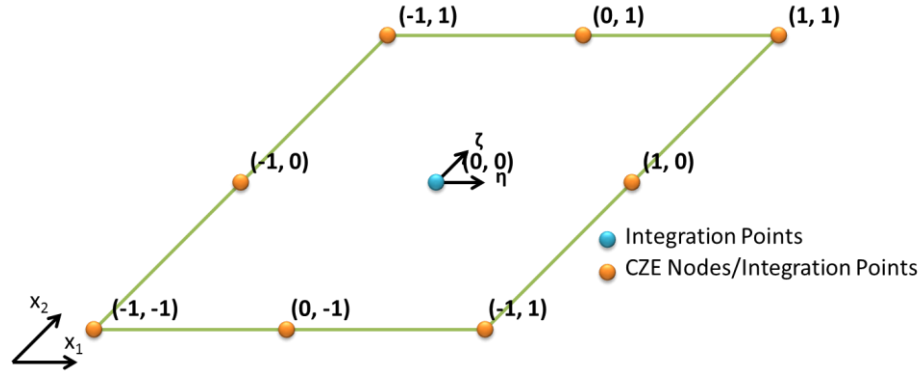


Figure 29: 3D Planar CZE integration points

$\mathbf{S}(\zeta, \eta)$  is a  $3 \times 24$  matrix where the  $i$ -th  $3 \times 3$  submatrix represents an identity matrix multiplied by the shape function value at the  $i$ -th node pair located the local coordinates  $(\zeta, \eta)$ .

$$\mathbf{S}(\zeta, \eta) = \begin{bmatrix} N_1(\zeta, \eta) & 0 & 0 & \cdots & N_8(\zeta, \eta) & 0 & 0 \\ 0 & N_1(\zeta, \eta) & 0 & \cdots & 0 & N_8(\zeta, \eta) & 0 \\ 0 & 0 & N_1(\zeta, \eta) & \cdots & 0 & 0 & N_8(\zeta, \eta) \end{bmatrix} \quad \text{E5.4}$$

Where  $N_i$  is the shape function value at node pair  $i$ . Combining equations E5.2 and E5.3 results in

$$\delta(\zeta, \eta) = \mathbf{S}(\zeta, \eta) \Phi d_N \quad \text{E5.5}$$

Which can be written as

$$\delta(\zeta, \eta) = \mathbf{B}d_N \quad \text{E5.6}$$

Where  $\mathbf{B}$  is a 3x48 Matrix and  $\delta(\zeta, \eta)$  is a 3x1 vector. Reference position coordinates can be calculated using equation E5.3.

$$\mathbf{x}^R(\zeta, \eta) = \mathbf{S}(\zeta, \eta)\mathbf{x}_N^R \quad \text{E5.7}$$

The vector normal to the  $\zeta$ - $\eta$  plane is derived by computing the normalized cross product of the global position vectors differentiated with respect to the local coordinate system as follows

$$\mathbf{t}_n = \frac{\frac{\partial \mathbf{x}^R}{\partial \zeta} \times \frac{\partial \mathbf{x}^R}{\partial \eta}}{\left\| \frac{\partial \mathbf{x}^R}{\partial \zeta} \times \frac{\partial \mathbf{x}^R}{\partial \eta} \right\|} \quad \text{E5.8}$$

The first tangential vector is computed by normalizing the global position vector differentiated by the local direction,  $\zeta$ .

$$\mathbf{t}_1 = \frac{\frac{\partial \mathbf{x}^R}{\partial \zeta}}{\left\| \frac{\partial \mathbf{x}^R}{\partial \zeta} \right\|} \quad \text{E5.9}$$

The second tangential vector is computed by taking the cross product of normal vector by the first tangential vector.

$$\mathbf{t}_2 = \mathbf{t}_n \times \mathbf{t}_1 \quad \text{E5.10}$$

The transformation matrix from the local to the global coordinate system is represented as

$$\mathbf{\Theta} = (\mathbf{t}_1, \mathbf{t}_2, \mathbf{t}_n) \quad \text{E5.11}$$

Thus, the local displacements are computed as

$$\delta_{loc}(\zeta, \eta) = \mathbf{\Theta}^T \delta(\zeta, \eta) \quad \text{E5.12}$$

The local y-displacement values are passed on to a subroutine to compute the stress traction values based upon the Traction Separation Function as described in Chapter 2. These tractions are computed in the local coordinate system, and then transferred back into the global coordinate system using the transformation matrix derived in equation E5.11. The RHS nodal force vector is computed by multiplying the transform of the  $\mathbf{B}$  matrix with the transform of the  $\mathbf{\Theta}$  matrix and the local tractions,  $\mathbf{t}_{loc}$  and finally the Jacobian,  $\mathbf{J}$ , then integrating over the area of the element as follows

$$\mathbf{f}_N = \int_A \mathbf{B}^T \boldsymbol{\Theta}^T \mathbf{t}_{loc} \mathbf{J} dS$$

$$\mathbf{f}_N = \int_{-1}^1 \int_{-1}^1 \mathbf{B}^T \boldsymbol{\Theta}^T \mathbf{t}_{loc} \mathbf{J} d\zeta d\eta$$
E5.13

Where the Jacobian is computed as follows

$$\mathbf{J} = \sqrt{(\mathbf{J}1)^2 + (\mathbf{J}2)^2 + (\mathbf{J}3)^2}$$

$$\mathbf{J}1 = \partial x_{\zeta}^R \partial y_{\eta}^R - \partial y_{\zeta}^R \partial x_{\eta}^R$$

$$\mathbf{J}2 = \partial x_{\zeta}^R \partial z - \partial z_{\zeta}^R \partial x_{\eta}^R$$

$$\mathbf{J}3 = \partial y_{\zeta}^R \partial z_{\eta}^R - \partial z_{\zeta}^R \partial y_{\eta}^R$$
E5.14

Each individual element of the Jacobian, J1, J2 and J3, may be negative, however the Jacobian itself cannot be negative. If the resulting Jacobian is negative the simulation will be terminated with an explanation of the error written into the message file. The stiffness matrix, which becomes a 48x48 matrix, is computed as

$$\mathbf{K}_N = \int_A \mathbf{B}^T \boldsymbol{\Theta}^T \mathbf{T} \boldsymbol{\Theta} \mathbf{B} dS$$

$$\mathbf{K}_N = \int_{-1}^1 \int_{-1}^1 \mathbf{B}^T \boldsymbol{\Theta}^T \mathbf{T} \boldsymbol{\Theta} \mathbf{B} d\zeta d\eta$$
E5.15

Where  $\mathbf{T}$  is the partial derivative of the local traction with the local displacements

$$\mathbf{T} = \frac{\partial \mathbf{t}_{loc}}{\partial \delta_{loc}} \quad \text{E5.16}$$

The final procedure in the FORTRAN code updates the RHS and AMATRIX matrices, SVARS vector and passes the ENERGY terms on to the ABAQUS solver. This entire procedure iterates for each cohesive element during each increment.

#### *5.4 Extracting a Realistic Traction Separation Law from DIC Data*

It is essential to utilize realistic damage parameters when conducting a simulation which is intended to replicate experimental fracture and damage results. Several methods exist for determining a Traction Separation Law based upon experiment data integrated with Digital Image Correlation used as an input into either a forward or inverse [4] optimization scheme. DIC data captures the full-field strains and displacements of the specimen at set intervals during the experiment. A set of four snapshots, located at evenly spaced intervals between the first onset of stable crack growth and the onset of unstable crack growth, will be used to extract realistic TSLs. Fifteen points, ahead of the crack tip and along the crack path, are selected in each frame for both strain and displacement as shown in Figure 30. A pixel color-matching scheme was used to correlate the points on the DIC field with its associated color bar where interpolation was employed, assuming that the scales are linear, to determine the true strain or displacement value of the selected pixel. Each strain value is converted to stress using a continuous piecewise function (E5.17) which has been fitted, with an  $R^2$  value of 0.995, to the experimentally derived tensile stress-strain curve for wrought Aluminum 2024-T3 Alloy plate [53]. The



displacement directly above and directly below the crack was measured for each point in a frame so that the separation could be calculated by finding the absolute value of the difference in displacement.

$$\sigma(\epsilon) = \begin{cases} 73.1 \times 10^3 \epsilon & | 0.0000 < \epsilon < 0.0036 \\ 52.6058235 \ln \epsilon + 568.4177412 & | 0.0036 < \epsilon < 0.1950 \end{cases} MPa \quad E5.17$$

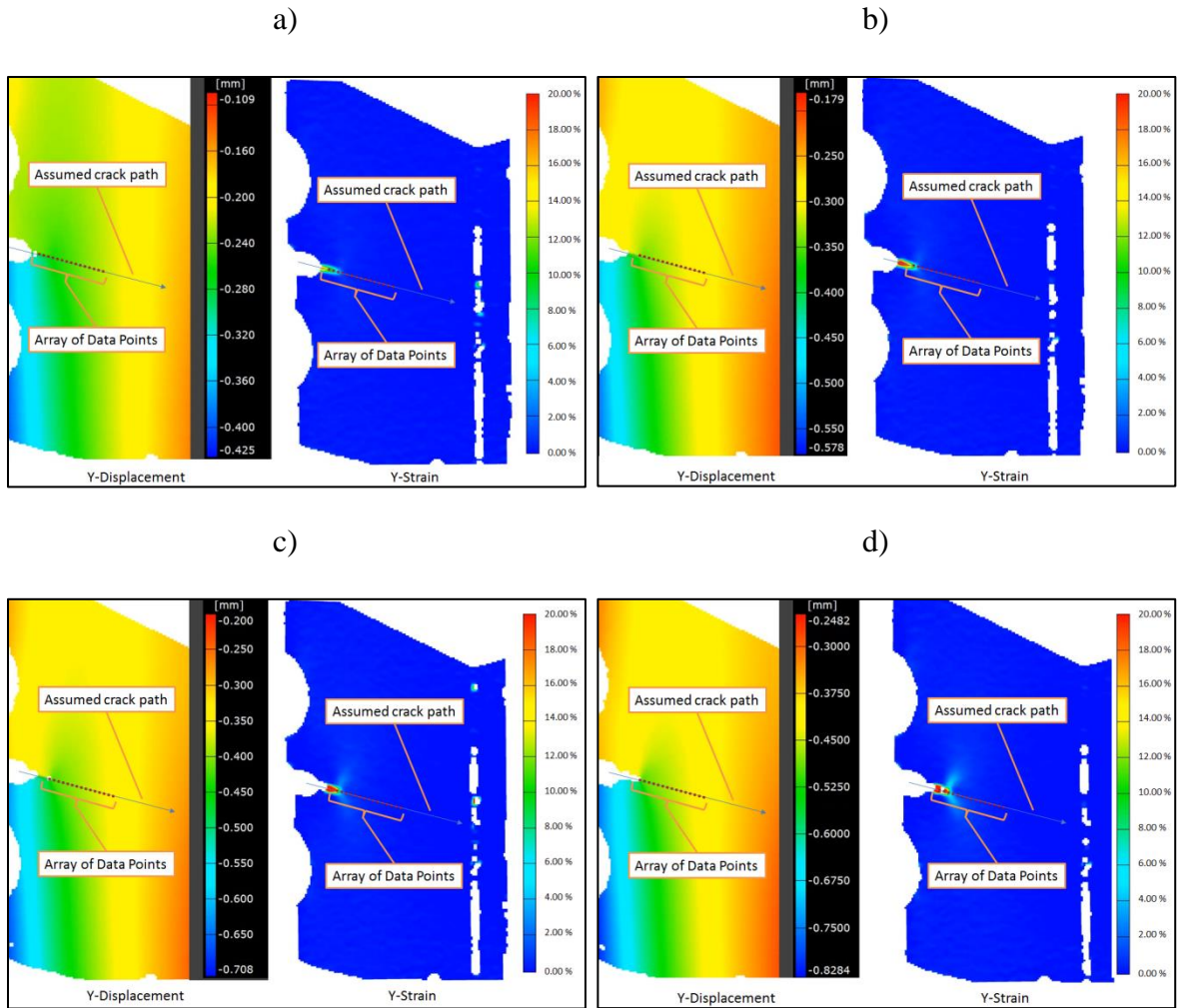


Figure 30: Y-Displacement (Left) and Y-Strain (Right) DIC snapshots at a)  $t = 60s$  and Load = 6.7kN, b)  $t = 80s$  and Load = 9.4kN, c)  $t = 100s$  and Load = 11.5kN, d)  $t = 120s$  and Load = 13.2kN

The data captured, on average, yielded 3-4 nonzero stress (i.e. nonzero strain) values per frame. These nonzero stress and their associated separation values are plotted in Figure 31. The resulting scatter plot shows a logarithmic trend where there is a sudden uptake of stress between 0.00 mm and 0.004mm of separation where 85% of the peak stress is achieved. An additional 15% peak load is achieved from 0.004 mm to 0.11 mm of separation.

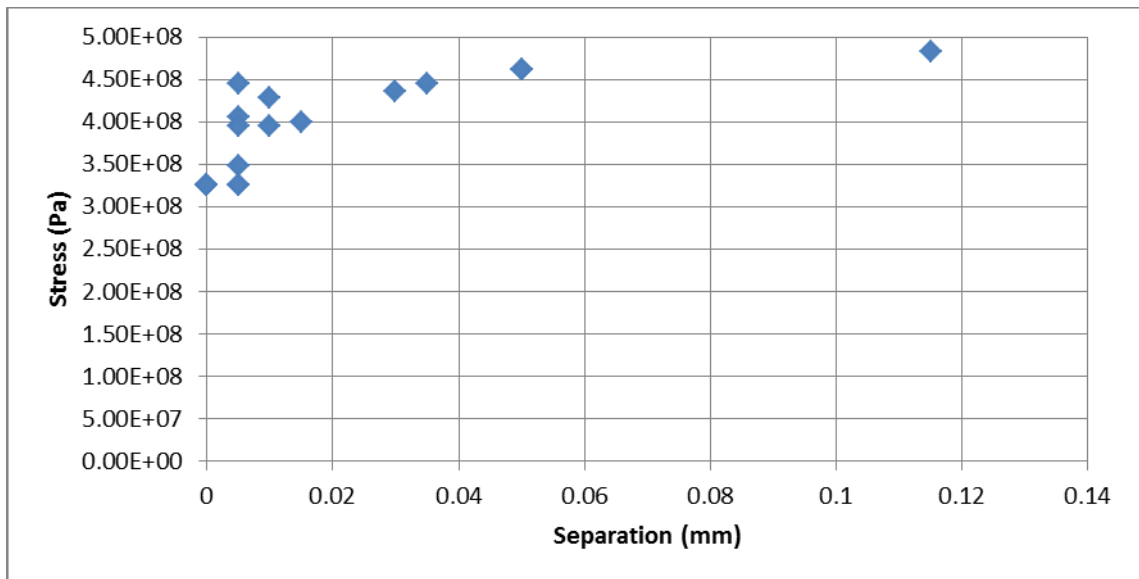


Figure 31: Stress-Displacement DIC-derived Data

A two parameter logarithmic-shaped function is devised to fit the data presented above. A true logarithmic function cannot be utilized in this case due to the requirement of a real stress value at the point where separation is zero. The following function, which meets these parameters, was selected.

$$\sigma(\delta) = \left(\frac{\delta}{\delta_c}\right)^{\left(\frac{1}{\alpha}\right)} \quad \text{E5.18}$$

Where  $\delta$  is the current separation,  $\delta_c$  is the critical separation and  $\alpha$  is an exponential parameter. The function will be optimized to the data by minimizing the average residual value through a Euclidean Normal routine as follows.

$$R = \frac{1}{N} \sum_{i=1}^N \sqrt{(\sigma_N - \sigma(\delta_N))^2} \quad \text{E5.19}$$

Where  $N$  is the number of data points, and  $\sigma_N$  and  $\delta_N$  are the  $N$ -th stress and separation DIC data values, respectively. The stress function was optimized for critical separation values between 0.45 mm and 0.60 mm, and alpha values between 20 and 40. The optimized values, based on the average residual value, were found to be a critical separation of 0.51 mm and an alpha value of 34 that yields the following optimized stress function as plotted against the original data points in Figure 32.

$$\sigma_{opt}(\delta) = \sigma_{peak} \left(\frac{\delta}{0.51}\right)^{0.0294} \quad \text{E5.20}$$

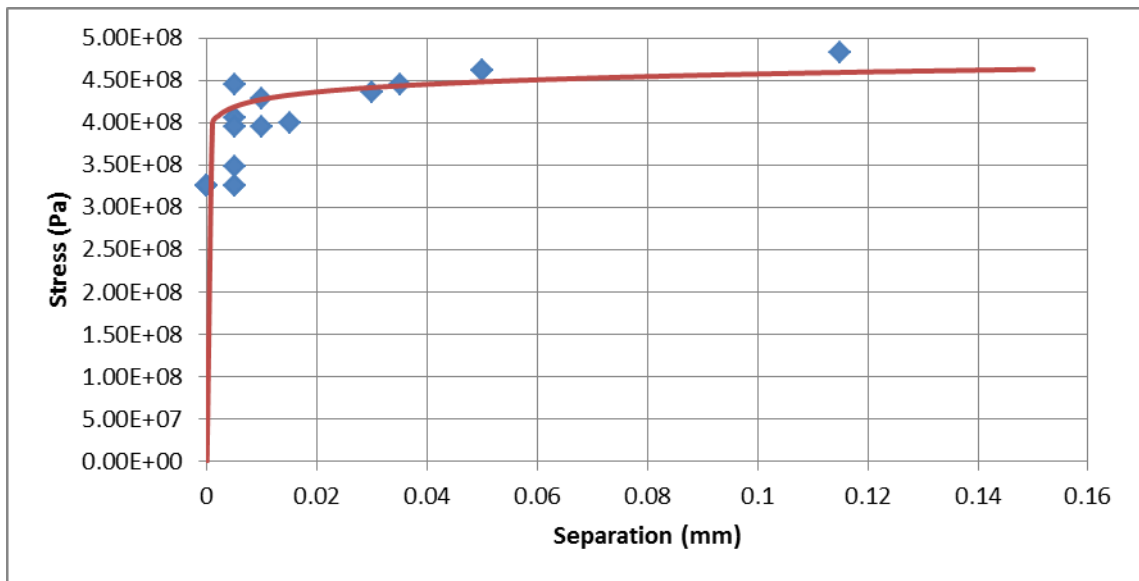


Figure 32: Two-parameter optimized stress function

An issue was discovered with this optimized stress function during an ABAQUS simulation. The initial stress uptake exceeds the linear-elastic material properties of Aluminum Alloy 2024-T3 so that the stress incurred by a small separation (on the order of  $10^{-15}$  m) resulted in an equilibrium solution where the correction to nodal displacements far exceeded the separation (on the order of  $10^{-8}$  m). This caused over-closure in the crack and penalty stresses which were on the same order of magnitude as the stress due to separation, thus the new equilibrium solution resulted in nodal separation on the same order of magnitude as the original separation—this cycle repeated until the simulation crashes due to non-convergence. It was found that a stress uptake of no more than 120 GPa/m may be utilized to withhold the linear-elastic properties of Aluminum Alloy 2024-T3. The proposed stress function (E5.18) was modified, to take this into account, by separating it into two distinct functions where a linear function is assumed up

to the yield stress and a nonlinear logarithmic-shaped function continues beyond the yield stress. It is important to ensure the stress function is continuous from a separation of zero to infinity. The following modified stress function is now proposed.

$$\sigma(\delta) = \begin{cases} 120 \times 10^9 \delta, & 0 \leq x \leq 0.003 \\ (\sigma_{peak} - \sigma_{yield}) \left( \frac{\delta - 0.003}{\delta_c} \right)^{\left(\frac{1}{\alpha}\right)} + \sigma_{yield}, & x > 0.003 \end{cases} \quad \text{E5.21}$$

An identical residual minimization scheme was used to optimize the new proposed stress function between critical separation values of 0.01 mm and 0.15 mm and alpha values between 5 and 25. The optimized values, based on the average residual value, were found to be a critical separation of 0.09 mm and an alpha value of 12 that yields the following optimized stress function as plotted against the original data points in Figure 32.

$$\sigma(\delta) = \begin{cases} 120 \times 10^9 \delta, & 0 \leq x \leq 0.003 \\ (1.8 \times 10^8) \left( \frac{\delta - 0.003}{0.09} \right)^{(0.0833)} + 3.0 \times 10^8, & x > 0.003 \end{cases} \quad \text{E5.21}$$

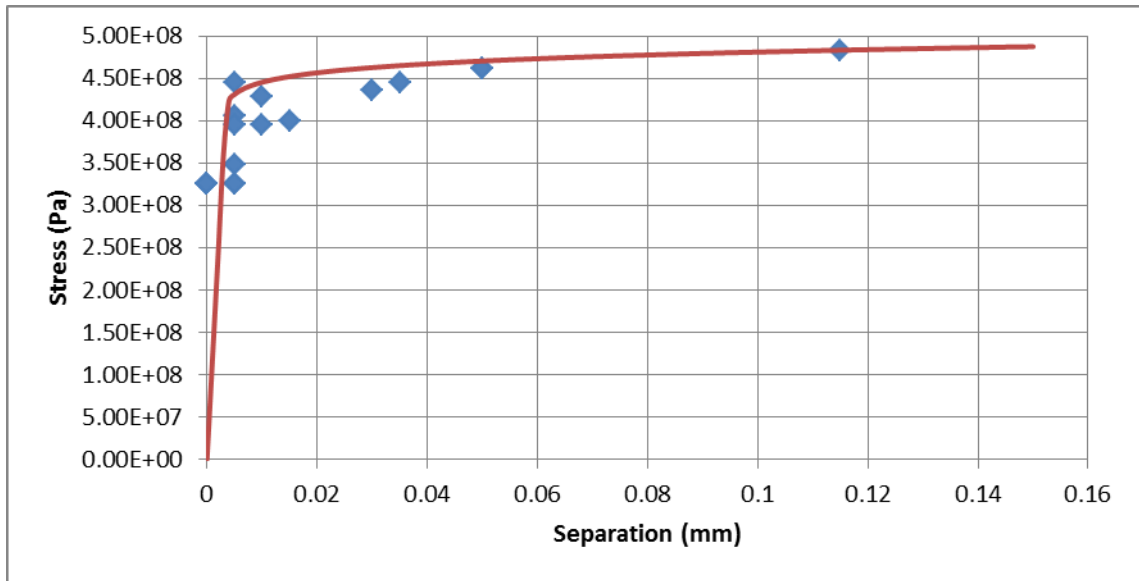


Figure 33: Modified two-parameter optimized stress function

The new stress function adheres to the material properties of the Aluminum Alloy and can be successfully implemented in ABAQUS as the next two sections will describe.

### 5.5 Integrating User Elements into ABAQUS

Creating a model which implements user elements begins with making a model in ABAQUS CAE in the exact same manner as if the simulation were to be run directly through the Graphical User Interface (GUI). The example used in this section is a Double Cantilever Beam (DCB) as shown in Figure 34. Due to symmetry, the geometry will be simplified by modeling only the upper half of the DCB. A cell of dimensions  $t_{cze}$  by  $w$  by  $l_{cze}$  as shown in Figure 35, where  $t_{cze}$  is the length of one individual CZE,  $w$  is the width of the model, and  $l_{cze}$  is the total length of the CZE interface, was created along the lower boundary where CZE will be inserted at a later point. Although the elements inside this

cell will not themselves be CZE, this will create a one element tall line of square continuum elements, which can be ordered and arranged in a specific manner to facilitate the insertions of CZE.

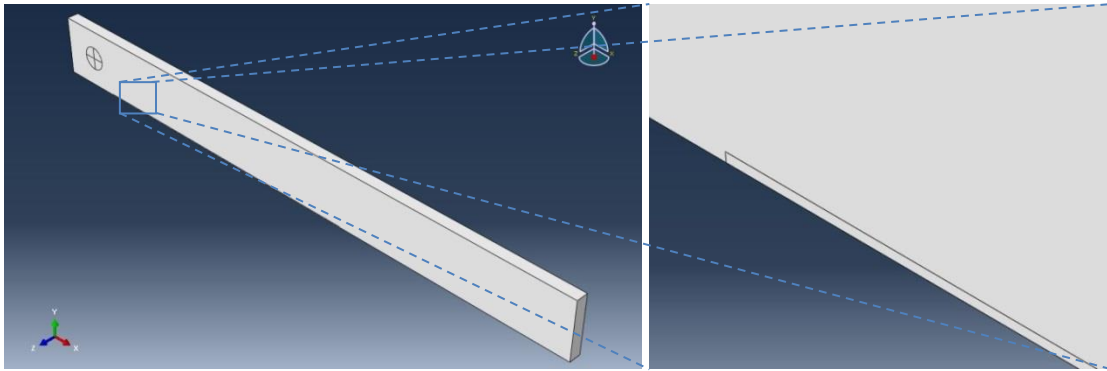


Figure 34: (Left) Double Cantilever Beam geometry, simplified to the half-model  
Figure 35: (Right) Cohesive Zone Element interface cell

A mesh is generated in the model using quadratic 20-node brick elements and a swept mesh generation algorithm to control the direction of element numbering along the CZE interface cell. Boundary conditions are applied as necessary except along the bottom face of the DCB where the CZE interface cell exists; In this area the face is fixed in the x, y and z direction as shown in Figure 36.

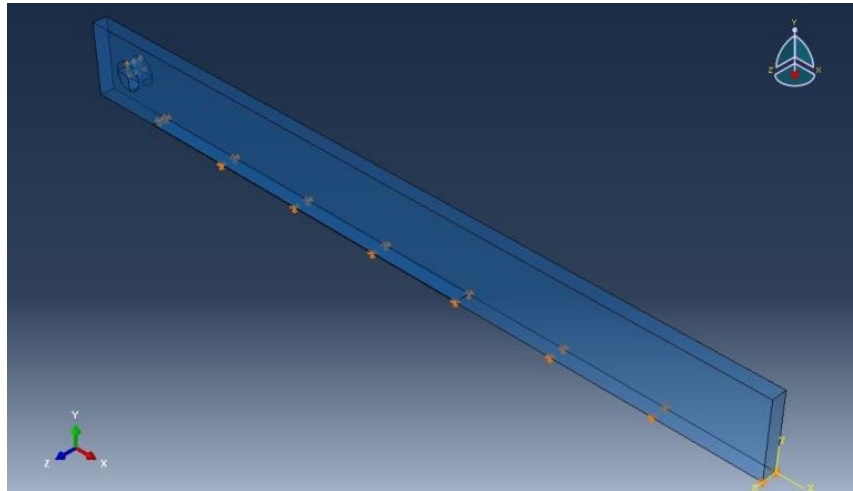


Figure 36: Boundary Conditions applied to the DCB model

This is done to lock what will become the bottom face of the CZE from moving during the simulation, which is often an issue that will yield a simulation error and termination due to elements excessively distorting.

ABAQUS does not have a direct method of inserting user-generated elements in the GUI. Instead, the UEL must be manually inserted into the input file using specific keywords. To do so, appropriate loading steps, part instances, history and field outputs were added as necessary to complete the model and a job was created for the DCB model but not submitted through ABAQUS CAE; instead, an input file, which will be used to create the CZE, was written from the job. Two new text documents, *AllElements* and *AllNodes* were created for use with a MATLAB routine designed to output the necessary text to insert CZE into the existing model. As their names suggest, the *AllElements* file contains a list of all elements in the model, and their associated nodes, whereas the *AllNodes* file



contains a list of all nodes associated with the model. These were created by copying the Node and Element data from the input file, as characterized by the keywords

```
*Node
    1,      -0.234999999000,      0.007499999830,      0.002000000090
    2,      -0.239999995000,      0.012500000200,      0.002000000090
    ⋮          ⋮                  ⋮                  ⋮
```

where the first column is the node number and the next three columns are the x-, y- and z-coordinates, respectively. Similarly, the Element keyword is as follows

```
*Element, type=C3D20
1,  1,  2,  3,  4,  5,  6,  7,  8,  9,  10,  11,  12,  13,  14,  15,
    16,  17,  18,  19,  20
2,  21,  22,  23,  24,  25,  26,  27,  28,  29,  30,  31,  32,  33,  34,  35,
    36,  37,  38,  39,  40
⋮   ⋮   ⋮   ⋮   ⋮   ⋮   ⋮   ⋮   ⋮   ⋮   ⋮   ⋮   ⋮   ⋮   ⋮   ⋮
```

where each element definition requires two rows due to the ABAQUS limitation of 16 data entries per line of the input file. In the odd rows, the first column is the element number while columns 2-5, 6-9 and 10-13 represent the corner nodes of the bottom face, the corner nodes of the top face, and the midpoint nodes on the bottom face, respectively. The last three columns of the odd rows and the first column of the even rows account for the midpoint nodes of the top face. The final four nodes of the even rows are the

midplane corner nodes, which fall between the bottom and top faces. Figure x depicts this graphically.

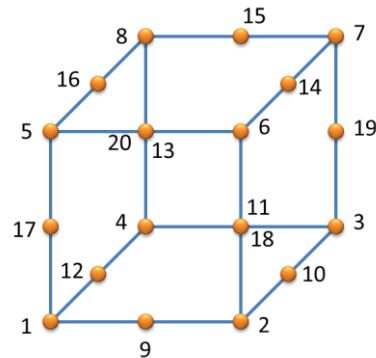


Figure 37: ABAQUS node naming convention for 20-node continuum brick elements

The MATLAB routine is a function that takes the inputs of the first and last elements of the CZE interface cell, the total number of elements in the model and the number of rows of elements in the CZE interface cell. After initializing the necessary variables, the routine calculates the number of elements in each row of the CZE interface cell. This is extremely important since the generation of new nodes and the linking of existing nodes changes after the initial row. The code now iterates the following procedures for all elements in the CZE interface cell. To start, the first element and its associated nodes are found in the *AllElements* file. The eight nodes on the bottom face are labeled *coh1* through *coh8* in numerical order and their x-, y- and z-coordinates are copied to new nodes that replace the original eight nodes in the continuum element (Figure 38)—the appropriate values are updated in the *AllElements* file.

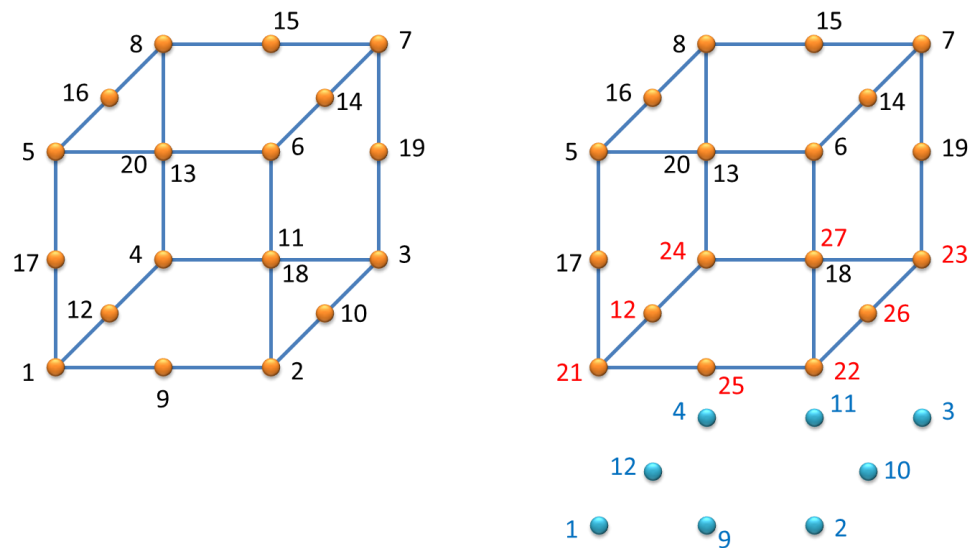


Figure 38: Separation of the bottom face nodes (blue) and replacement with new (red) nodes

The second element, and the remainder of the elements in the first row of the interface cell, will follow a similar pattern, however three less nodes need to be created for each CZE, as this element will share three nodes with the last element created, which is seen in Figure 39. If the interface cell consists only one row of elements then the iterative scheme ends at this point, otherwise it continues as follows: The first element of the second row shares three nodes with the first element of the first row similarly to how the second element of the first row shares three nodes with the first element of the first row. The second element, and the remainder of the elements in the second row of the interface cell, will follow a similar pattern, however six less nodes need to be created for each CZE, as this element will share three nodes with the last element created and three nodes with the previously created adjacent element, which is seen in Figure 40.

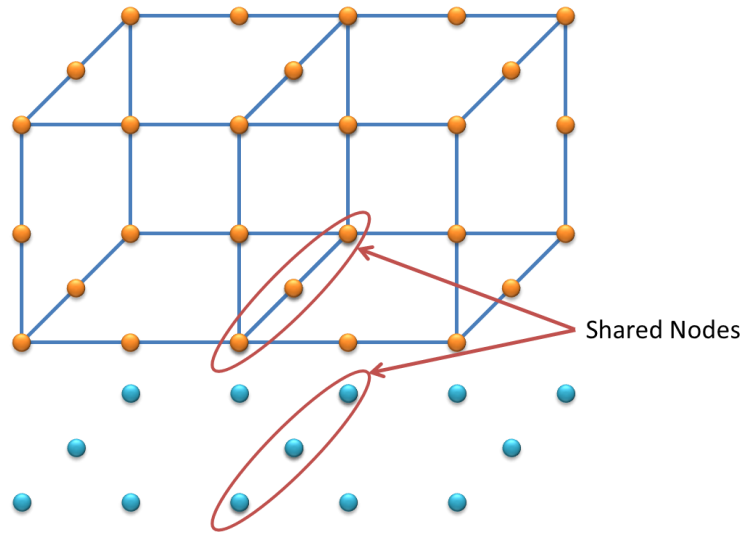


Figure 39: Shared nodes between the first and second element of the CZE interface cell

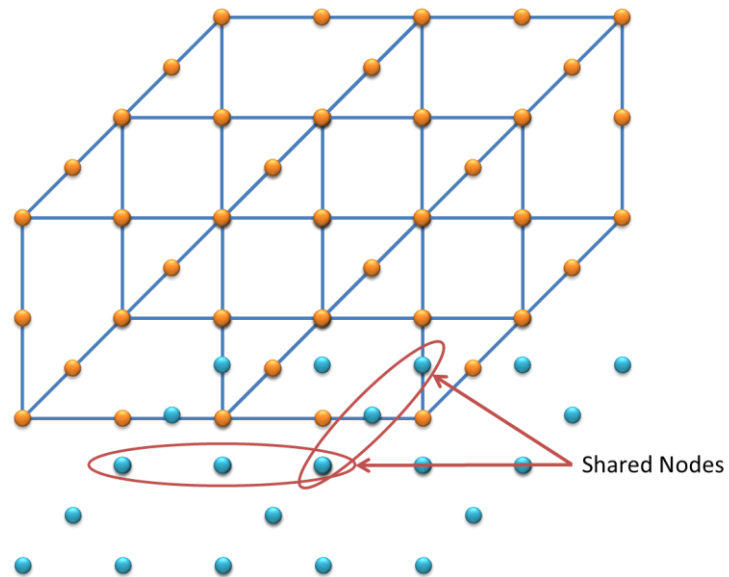


Figure 40: Shared nodes between the first and second element of the second row and the second element of the first row

After the duplication and replacement of the appropriate nodes the cohesive element is written to a temporary file as follows

*\*Element, type=U16*

```

1,  1,  2,  3,  4,  5,  6,  7,  8,  9, 10, 11, 12, 13, 14, 15,
   16
2, 17, 18, 19, 20, 21, 22, 23, 24, 25, 26, 27, 28, 29, 30, 31,
   32
:   :   :   :   :   :   :   :   :   :   :   :   :   :

```

where the first column of the odd rows is the element number and the 2-5, 6-9 and 10-13 columns are the bottom face corner nodes, bottom face midpoint nodes, and top face corner nodes, respectively. The last three columns of the odd rows and the first column of the even rows are the top face midpoint nodes.

Upon the completion of the iterative scheme, the routine will create a file, which prints all of the nodes, seamlessly including the added nodes, followed by the user element declaration keyword, the original element keyword and finally the new user element keyword. An example of this output is shown below.

*\*Node*

```

1,    -0.234999999000,    0.007499999830,    0.002000000090
2,    -0.239999995000,    0.012500000200,    0.002000000090
:      :                  :                  :
n+1  -0.234999999000,    0.007499999830,    0.002000000090
n+2  -0.239999995000,    0.012500000200,    0.002000000090
:      :                  :                  :

```

*\*User element, type=U16, nodes=16, coordinates=3, i properties=2, properties=6, variables=63*

```

1,  2,  3

```

```

*Element, type=C3D20
1, 1, 2, 3, 4, 5, 6, 7, 8, 9, 10, 11, 12, 13, 14, 15,
   16, 17, 18, 19, 20
2, 21, 22, 23, 24, 25, 26, 27, 28, 29, 30, 31, 32, 33, 34, 35,
   36, 37, 38, 39, 40
:  :  :  :  :  :  :  :  :  :  :  :  :  :  :  :
*Element, type=U16
1, 41, 42, 43, 44, 45, 46, 47, 48, 49, 50, 51, 52, 53, 54, 55,
   16
2, 57, 58, 59, 60, 61, 62, 63, 64, 65, 66, 67, 68, 69, 70, 71,
   72
:  :  :  :  :  :  :  :  :  :  :  :  :  :  :  :

```

The user element declaration keyword contain a minimum of seven values over two lines—the first holds six variables which are assigned values. The first of these variables is the *type*, which follows the ABAQUS naming convention for user elements, where *Un* is the element name and *n* is an integer between 1 and 1000. For this example, *n* was chosen to be the number of nodes. Following *type* on the first line are *nodes*, *coordinates*, *i properties*, *properties*, and *variables* which are the number of nodes associated with the element, the number of coordinates for each node, the number of integer properties to be set by the UEL Property keyword, the number of real floating-point properties to be set by the UEL Property keyword, and the number of solution-dependent state variables, respectively [54]. The second line contains the degrees of freedom, separated by commas. In this example, the UEL is for a 3D case and cannot hold any moments thus only DOF 1, 2 and 3 are active which are the translations in the x-, y- and z-directions, respectively.

This output directly replaces all input file data from the original node keyword through the original element keyword.

A second MATLAB routine was developed for computing the outputting the UEL Property keyword based upon the Traction Separation Law being utilized and the properties required in the FORTRAN code. Regardless of what scheme was being utilized the inputs always contained the peak bridging stress, the separation at which peak stress was achieved, the separation at which weakening began and finally, the critical separation where stresses go to zero. The output file contained the the UEL Property keyword in the following format

```
*UEL Property
0.05e-3, 0.15e-3, 10.0, 484.0e6, 1000.0, 1.0, 9, 1
```

Where each line contains a maximum of eight values per the ABAQUS requirements, and  $n$  real floating point properties are listed before  $m$  integer properties where  $n$  and  $m$  are the *properties* and *i properties* values, respectively, defined in the User Element declaration keyword. The UEL Property keyword is inserted into the input file directly after the last section declaration keyword inside the part definition as shown below.

```

:
** Section: Aluminum
**Solid Section, elset=_PickedSet12, material=Aluminum

** Section: Rigid
```

```

*Solid Section, elset=_PickedSet13, material=Aluminum
,
*UEL Property
0.05e-3, 0.15e-3, 10.0, 484.0e6, 1000.0, 1.0, 9, 1
*End Part
:

```

Upon completion of this final step, the original model will now have user-defined elements inserted along the CZE interface cell and define with the properties necessary to drive the Cohesive Zone Element FORTRAN code.

### *5.6 Integrating FORTRAN into ABAQUS Solver Environment*

ABAQUS requires specific applications and compilers, depending upon the version of ABAQUS and the operating system, for integrating user-defined codes into the solver system. For example, ABAQUS v6.10, which is used throughout this thesis, requires Intel Fortran Compiler V10.1 or 11.1, Microsoft Visual C++ 2008 SP1 or 2010 and MS-MPI v2.0, 2.1 or 2.2 for a Windows-based system. All requirements for ABAQUS releases can be found on the 3DS support website<sup>1</sup>. The current configuration of a system can be tested through the ABAQUS Command prompt by running the command *abaqus sysinfo* which will output the following

If any configuration is missing or incorrect it will appear here as *FAIL* – “*Description of why component did not pass*”. It should be noted that certain components could be newer than that specified by the ABAQUS requirements, however it is not recommended nor guaranteed that the functionality will be identical and it may appear as a *FAIL* in the

---

<sup>1</sup> <http://www.3ds.com/support/certified-hardware/simulia-system-information/>



*sysinfo* results regardless of the true functionality of that component. Due to the obsolescence and removal of Intel FORTRAN Compiler V10.1 and 11.1 from the market, Intel FORTRAN Composer XE<sup>2</sup> (Compiler V12.1) was tested and found to work in certain configurations of Windows XP x64 and Windows 7 x64-based systems. Additionally, it was found that ABAQUS v6.10 CAE, Viewer and the ABAQUS Command prompt function under Windows 8 x64 Consumer Preview Build 8250 however multi-core solver functionality is limited to threading mode only.



```

Intel(R) Visual Fortran Intel(R) 64 Compiler Professional for applications running on Intel(R)
System requirement status is:
Requirement:      Windows Server 2003, Windows Server 2008, Windows Server
                  2008 R2, Windows HPC Server 2008, Windows XP, Windows
                  Vista, or Windows 7
Products:         All Abaqus Products
Status:           Pass - Found Microsoft Windows XP Service Pack 2 (Build
                  3790) (x64).

Requirement:      Microsoft Visual C++ 9.0 (2008), or 10.0 (2010)
Products:         Abaqus make utility with C++
Status:           Pass - Found Microsoft Visual C++ 9.0.21022.8.

Requirement:      Intel Fortran Compiler 10.1, or 11.1
Products:         Abaqus make utility with Fortran and Abaqus with user
                  subroutines
Status:           Pass - Found Intel Fortran Compiler 11.1 Build 20101201
                  Package ID w_cprof_p_11.1.072.

Requirement:      MS-MPI 2.0, 3.0 or greater
Products:         Abaqus analyses using MPI-based parallelization and
                  Abaqus/CFD
Status:           Pass - Found MS-MPI 2.1.1765.0.

Requirement:      Internet Explorer 6.0 or 7.0 or 8.0, Firefox 2.0 or 3.0
                  or 3.5 or greater
Products:         Abaqus Documentation
Status:           Pass - Found Internet Explorer 8.0.6001.18702

All requirement checks succeeded.

```

Figure 41: ABAQUS System Information and Configuration Results for a Windows XP x64 system

Integrating the FORTRAN code and the modified input file poses the same issue that was present in the ABAQUS GUI when incorporating user-defined elements—that is

<sup>2</sup> <http://software.intel.com/en-us/articles/intel-composer-xe/>

ABAQUS GUI does not natively support these simulations; instead, the ABAQUS Command prompt must be utilized. Regardless of the operating system of the ABAQUS computer, the commands for running a simulation are identical; however guiding the command prompt to the folder where the input file is stored requires specific and often different commands depending upon the operating system. The input file and FORTRAN code must be located in the same folder and the FORTRAN code must have file extension `.for` in a Windows environment or `.f` in a Linux environment. To run a simulation, use the command

```
abaqus job=job_name user=code cpu=n interactive
```

where *job\_name* is the name of the input file, *code* is the name of the FORTRAN code file, *n* is the number of cores the simulation will use, and *interactive* is an optional command which will print the status of the simulation in the ABAQUS Command prompt window. It should be noted that if an interactive simulation were run, closing the command window would terminate the simulation. An additional option when running large simulations in a cluster environment is to utilize the MPI interface to distribute the load over several nodes. To do so, an additional statement is added to the above command

```
abaqus job=job_name user=code cpu=n mp_mode=MPI interactive
```

Additionally, the ABAQUS environment file must be updated to include the computing nodes and the number of cores on each machine as follows

$$mp\_host\_list=[['node1',4],['node2',8],\dots,['nodeN',6]]$$

where *node1*, *node2*, ... , *nodeN* are the host names of the computing nodes and the number which follows the name is the number of cores on that machine. Although each node does not need to have the same number of cores, ABAQUS will use a “Pauli Exclusion Principle”-like method for distributing the load over the number of cores specified by the command statement *cpu=n*. It is important to note that multi-node performance is highly dependent upon the computing nodes, their operating system, the interconnection speed, the size (Total DOFs) and type of simulation, and several other factors. Numerous studies [55]<sup>3</sup> have been conducted on various setups and a common theme exists where, after a certain number of cores are utilized, performance gains are trivial or even hindering.

### 5.7 Testing the FORTRAN code and the FORTRAN/ABAQUS interconnectivity

The above-discussed DCB CZE model was used as a test model to ensure the CZE implementation through MATLAB, the FORTRAN code and the FORTRAN/ABAQUS interconnectivity were functioning properly.

Loading was applied as a constant-rate displacement of 0.5mm/min over the course of one minute with an initial step size of 0.1s up to the point directly before the first

---

<sup>3</sup> [http://www.hpcadvisorycouncil.com/pdf/Abaqus%20Performance%20Analysis\\_.pdf](http://www.hpcadvisorycouncil.com/pdf/Abaqus%20Performance%20Analysis_.pdf)

increment of crack growth located at approximately 34.4s. At this point, and through the remainder of the simulation, the step size was decreased to 0.01s to improve stability and solution accuracy. Nonlinear discontinuous solver effects were taken into account throughout the entire simulation and the displacement correction factor ratio [52], an ABAQUS solver convergence criteria, was varied from 0.1 up to the point of crack growth, to 100 during crack propagation to allow for the sudden displacement jumps due to the failure of nodes.

Zero-thickness elements are not physically displayed in ABAQUS Viewer; instead, they are represented by an  $\times$  located at the first node of the element as shown in Figure 42.

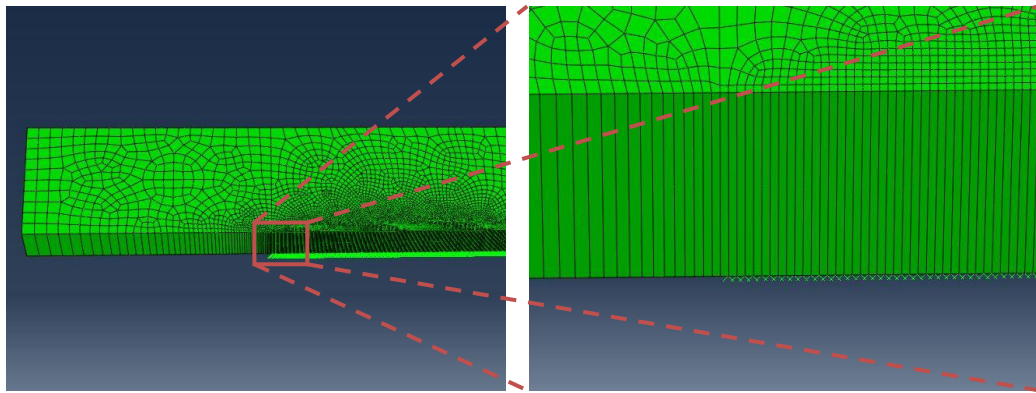


**Figure 42: Bottom face of the CZE interface cell showing CZE zero-thickness elements**

The results below (Figure 43) have been divided into three stages to show the progression of y-stress, y-strain and y-displacement 1) directly before crack growth ( $a = 0.00$  mm), 2) after 0.10 mm of crack growth and 3) after 2.00 mm of crack growth. Note that in the stress plots, the crack tip is easily seen by the sudden shift from a high stress area of 480+

MPa (red/organge) to zero stress (dark blue) or even negative stress (black) due to the geometry. Strain follows a similar pattern, however the defining line between elements which have failed (white) and elements which are still in tension (red through blue) can be seen in y-displacement plots as the vertical displacement exceeds the critical separation value of 0.15mm.

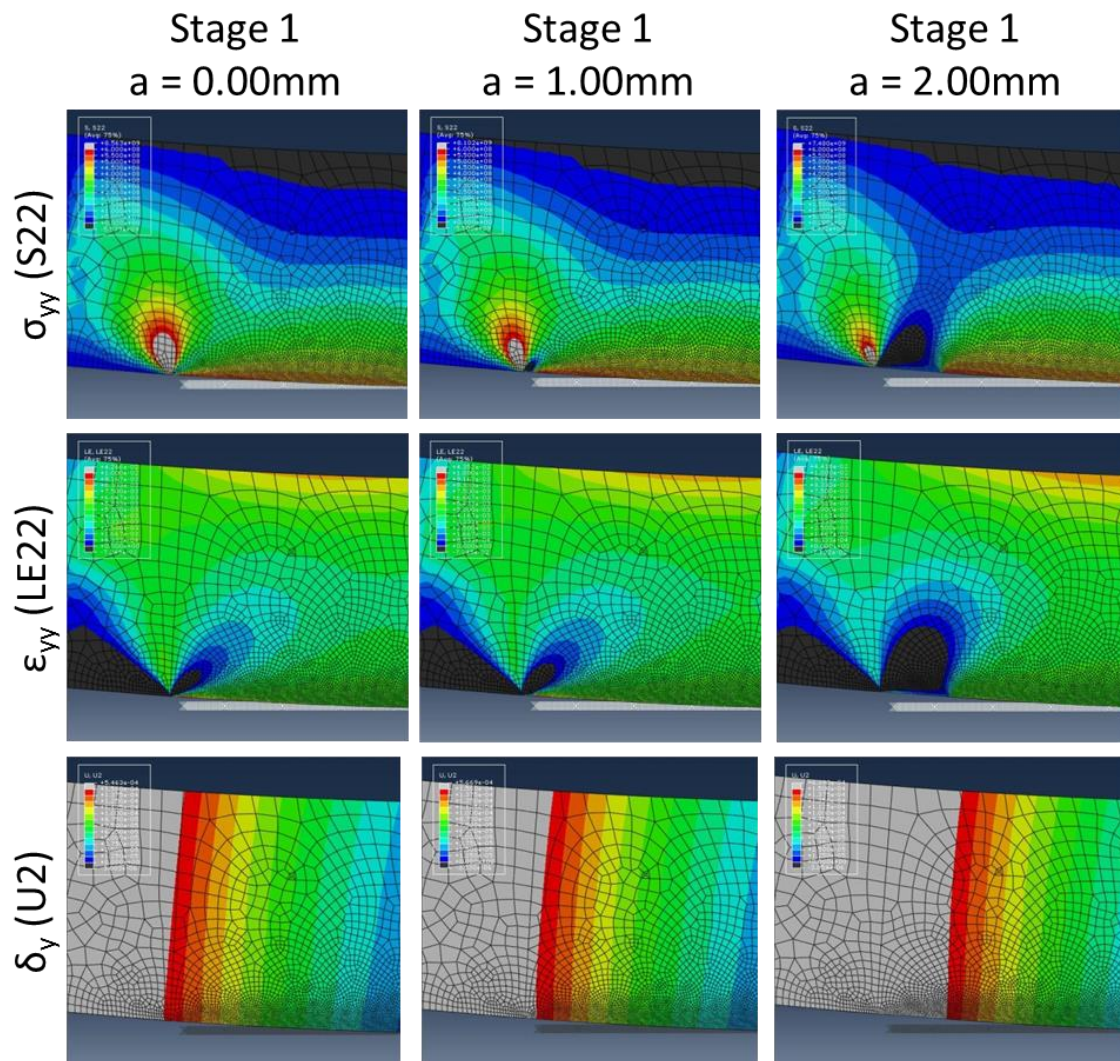


Figure 43: Stress, Strain and Displacement Field Outputs for a DCB with CZE

Similarly, the exact position of the crack tip can be tracked by monitoring the reaction force of the nodes in each CZE such as Figure 44, which shows the reaction force in the first CZE along with the reaction force at the applied displacement node. Note that the reaction force at the applied displacement reaches its peak value when the first CZE fails, and continues to decrease as the crack propagates. The displacement plots of Figure 43 are expanded upon by tracking the vertical displacement of each CZE, which reveals displacement contours of the interface edge at different time increments as seen in Figure 45. A distinct pattern is seen where the displacement contour is negatively sloped and positively contoured below the critical separation value for all time steps. Conversely, the displacement contour is negatively sloped and negatively contoured above the critical separation value for all time steps.

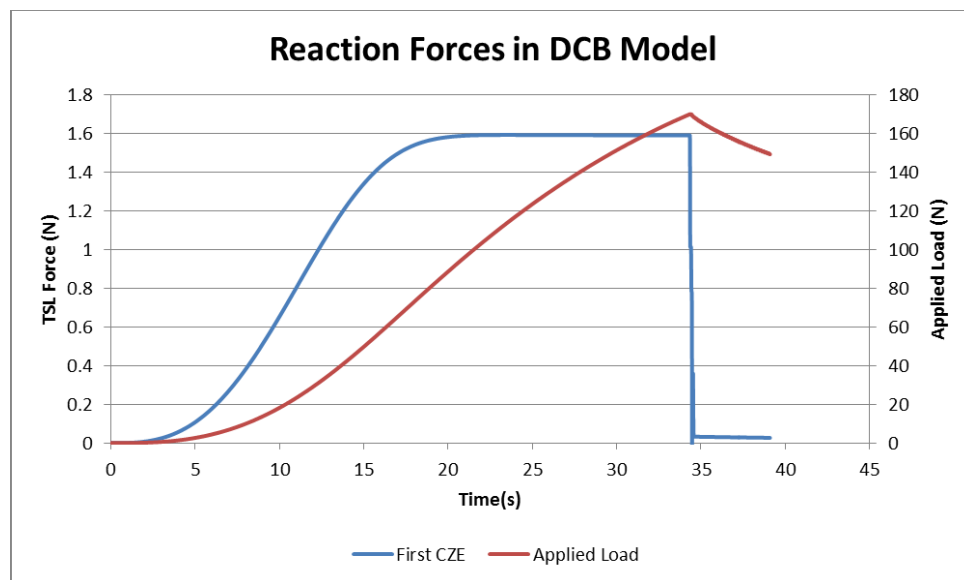


Figure 44: Reaction forces in the first CZE and the applied displacement node

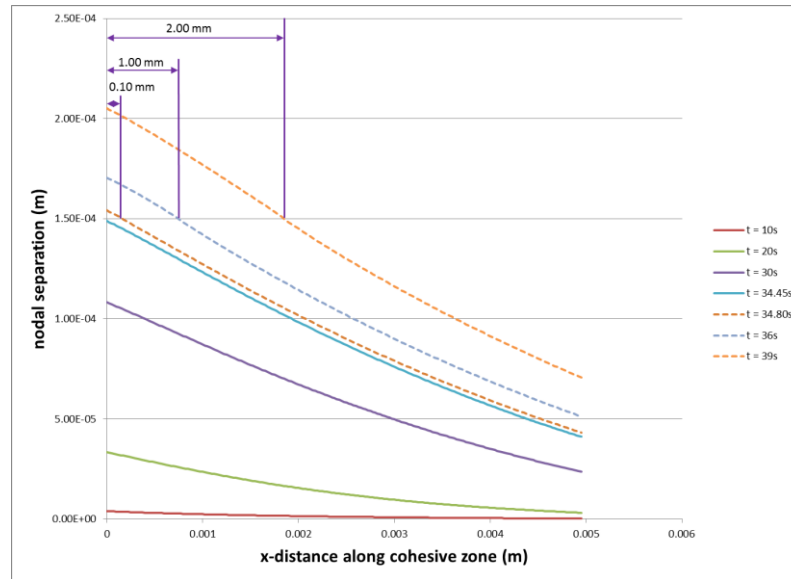


Figure 45: Nodal displacement along the CZE interface at various time steps

## **Chapter 6: Approach to Crack-Driven NDT Simulation**

Up to this point in this thesis, a specifically designed fracture experiment was used to capture mechanical and NDT data that were used in an optimization framework that yielded a realistic traction-separation law, which was later inserted into a quasi-static crack growth simulation. From this quasi-static simulation, the stress, strain and displacement fields at equilibrium points directly before and directly after an increment of crack growth will be utilized in this Chapter as inputs to a dynamic simulation capable to capture the generation and propagation of transient elastic waves caused by the rapidly changing strain energy associated with the crack growth. The presented results constitute a direct linkage between theoretical fracture mechanics and Acoustic Emission and show good agreement with corresponding experimental data. Figure 47 presents a flow chart of the information presented in this chapter including preliminary modeling efforts to investigate computational the transient response associated with energy release due to crack growth, as well as actual simulation efforts for damage-induced elastic wave propagation.



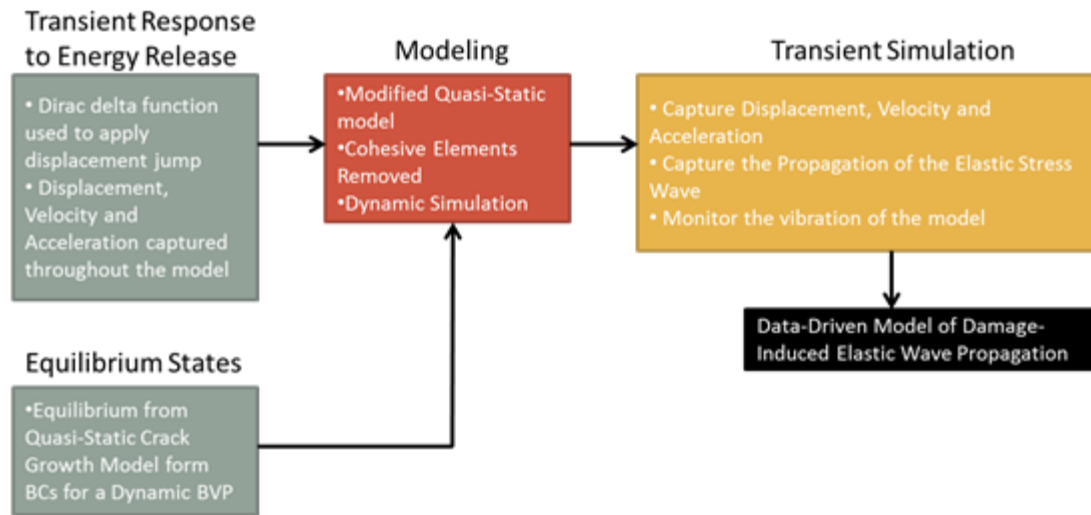


Figure 46: A brief mapping of the Chapter 6 layout

### 6.1 Transient Response Due to a Sudden Equilibrium Change

Before linking the quasi-static simulation to the dynamic simulation, it is critical to ensure that a sudden change in the equilibrium state of a continuum body will result computationally in the production and propagation of an elastic stress wave. To this aim, a Double Cantilever Beam (DCB) will be used in this section in a dynamic simulation where the exterior boundaries will be fixed in a manner that is similar to that of the Cohesive Zone Model used in Chapter 5, except in this case there will be no Cohesive Zone Elements. Loading will not be applied to the rigid pin; instead, a 5-mm segment of the lower boundary at the crack tip will be uniformly displaced in the positive  $y$ -direction by 90nm over the course of 1 microsecond in a Dirac delta-like function  $\delta(t)$  given in (E6.1) [56].

$$\delta(t) = \frac{C}{a\sqrt{\pi}} e^{-((t - 5 \times 10^{-7})^2/a^2)} \quad (\text{E6.1})$$

In E6.1  $a$  is a constant which adjusts the shape of the Dirac delta function and  $C$  is a multiplication constant to achieve the desired displacement of 90nm. A Dirac delta function was chosen in an attempt to excite all possible frequencies,

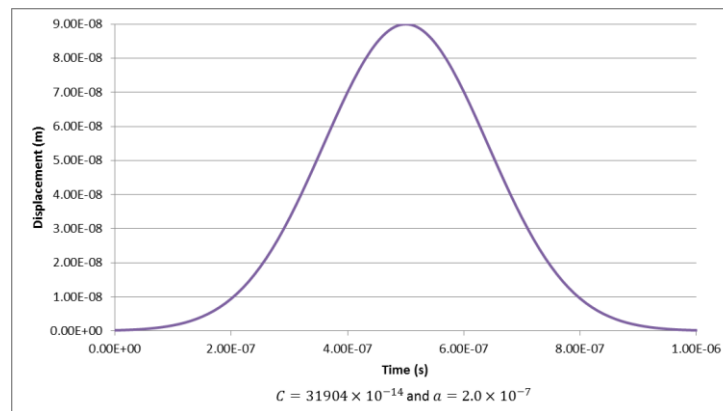


Figure 47: Dirac delta function utilized to create a sudden shift in equilibrium states

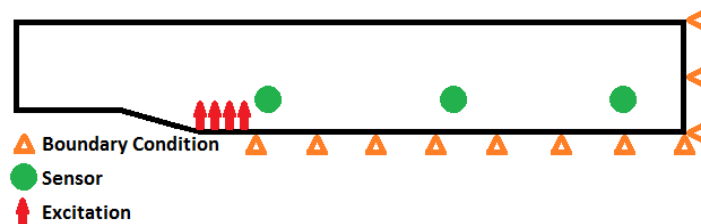
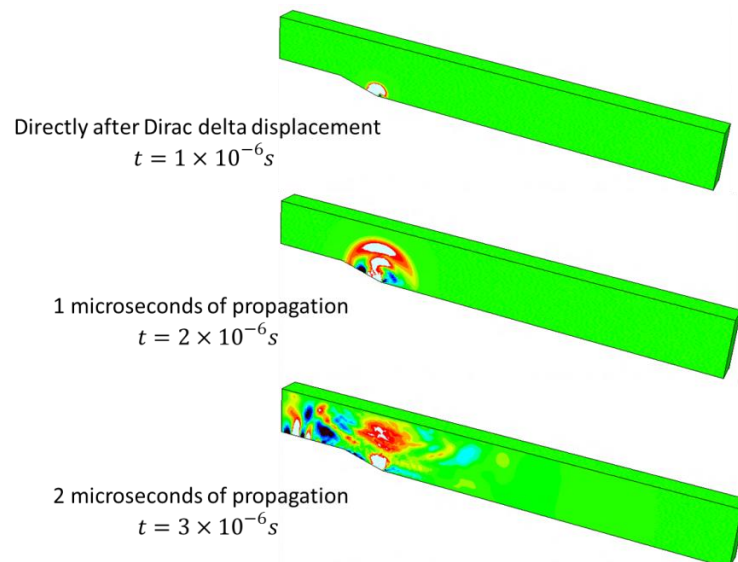


Figure 48: General schematic for transient dynamic simulation

The out-of-plane displacement, velocity and acceleration will be captured on the surface of the specimen at near-, mid- and far-field locations, each of which are located 10.0mm above and 0.0mm, 20.0mm and 40.0mm, respectively, away from the crack tip in the x-direction as shown in Figure 49. Data was captured at a fixed rate of 50MHz which is based on the maximum stable time step calculated by ABAQUS. The results of this simulation clearly show the development and propagation of an elastic stress wave originating at the location of forced displacement and radiating outward in a half-moon ripple pattern as illustrated in Figure 49.



**Figure 49: Elastic stress wave propagation due to a Dirac delta displacement of 90nm**

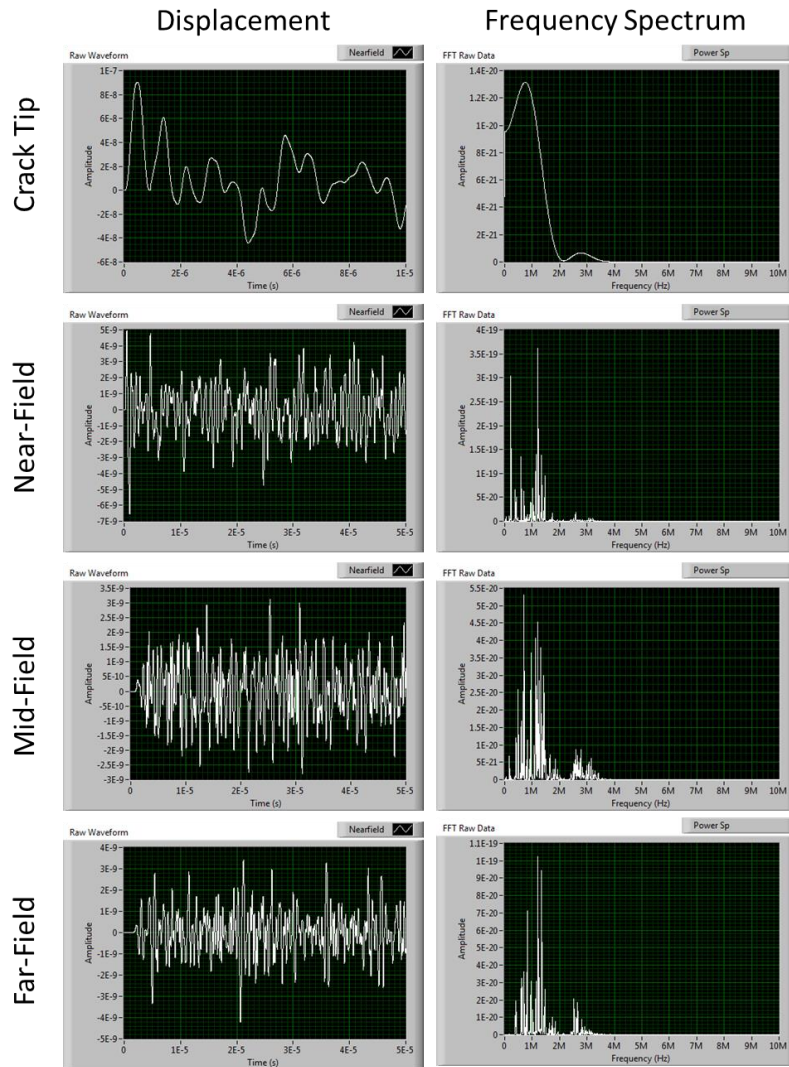


Figure 50: Out-of-plane displacements and frequency spectrums recorded at the near-, mid-, and far-field locations

Additionally, Figure 51 shows the near-, mid- and far-field out-of-plane (z-direction) displacement along with their associated frequency spectrum. Appendix B contains the displacement, velocity and acceleration data for this simulation. It should be noted that unlike the experimental setup described in Chapter 4, the captured data displaced below

is unfiltered so that all excited frequencies are displayed. The frequencies excited by the Dirac delta displacement function were not uniformly distributed as expected, however the distribution was a smooth function from 0MHz to 2MHz with a peak around 750kHz. A secondary smooth function occurred from 2MHz to 4MHz with a peak around 3MHz. The secondary function's peak amplitude was approximately twenty times less than the peak of the first function. Similarities between the frequency spectrums captured at the three locations compared to the Dirac delta displacement spectrum can be seen. Although the spectrums are no longer a smooth function, meaning that certain frequencies have dissipated, the same general pattern between 0MHz and 2MHz, and 2MHz to 4MHz can be seen with peaks occurring near 750 kHz and 3 MHz.

### *6.2 The Effect of Excitation Displacement Magnitude on the Transient Response*

After verifying that a sudden equilibrium change produces an elastic stress wave, a secondary study was conducted to determine the effect of maximum excitation displacement on the produced waveform at a given point. The peak displacements were chosen to be 60nm, 90nm, 500nm and 50 $\mu$ m with the same Dirac delta displacement function used before; in each case, the near-field location was selected to monitor the out-of-plane displacement. Note that 50 $\mu$ m was selected to produce plastic deformation at the point of loading. Figure 52 shows the displacements and frequency spectrums captured in these simulations. Analyzing the waveform plots shows that, although the peak amplitude increases, the general shape of the waveform remains consistent through all elastic deformation (60nm – 500nm). The 50 $\mu$ m plot follows the trend of increasing amplitude, however the shape of the waveform has, although still close, changed. Inspecting the

frequency spectrum plots reveals a similar trend where the general frequency decomposition for elastic deformation remains consistent. Again, the 50 $\mu$ m power spectrum follows the trend of increasing power however the frequency decomposition is significantly different than the previous three where frequencies greater than 2.5MHz have been truncated. Figure 53 and Figure 54 show the trend of increasing peak waveform amplitude at the near-field location and increasing peak frequency spectrum power as the peak displacement function increases; the waveform amplitude follows a highly linear trending whereas the power spectrum follows an increasing quadratic trend. Figure 51 shows the frequency which is associated with the peak frequency spectrum amplitude referenced in Figure 52 and Figure 54.

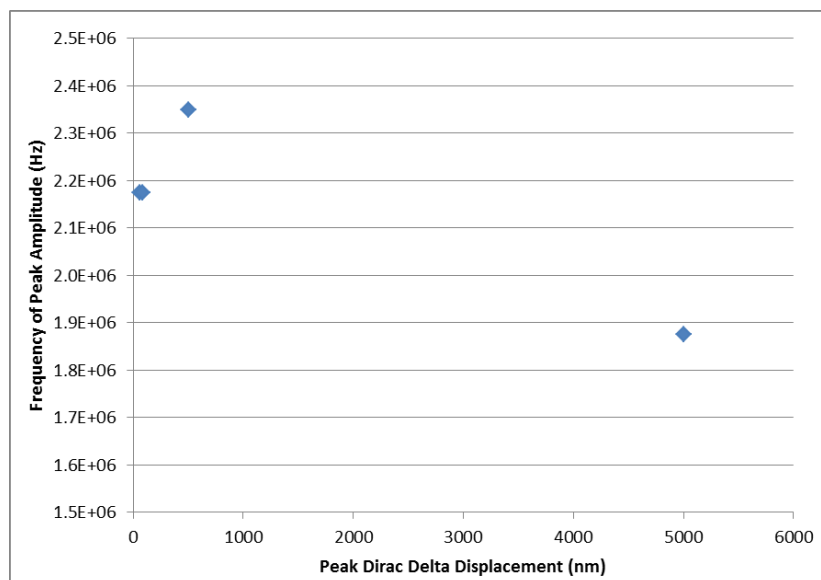


Figure 51: Frequency of the Peak Amplitude in the Power Spectrum

Both 60nm and 90nm displacements yield a peak amplitude frequency of 2.2MHz whereas 500nm and 50 $\mu$ m yields 2.4MHz and 1.9MHz, respectively. It is interesting to note that the frequency appears to increase with increasing peak displacement when in the fully linear elastic range, while an elastic-plastic deformation produces decreased frequencies.

### Displacement

### Frequency Spectrum

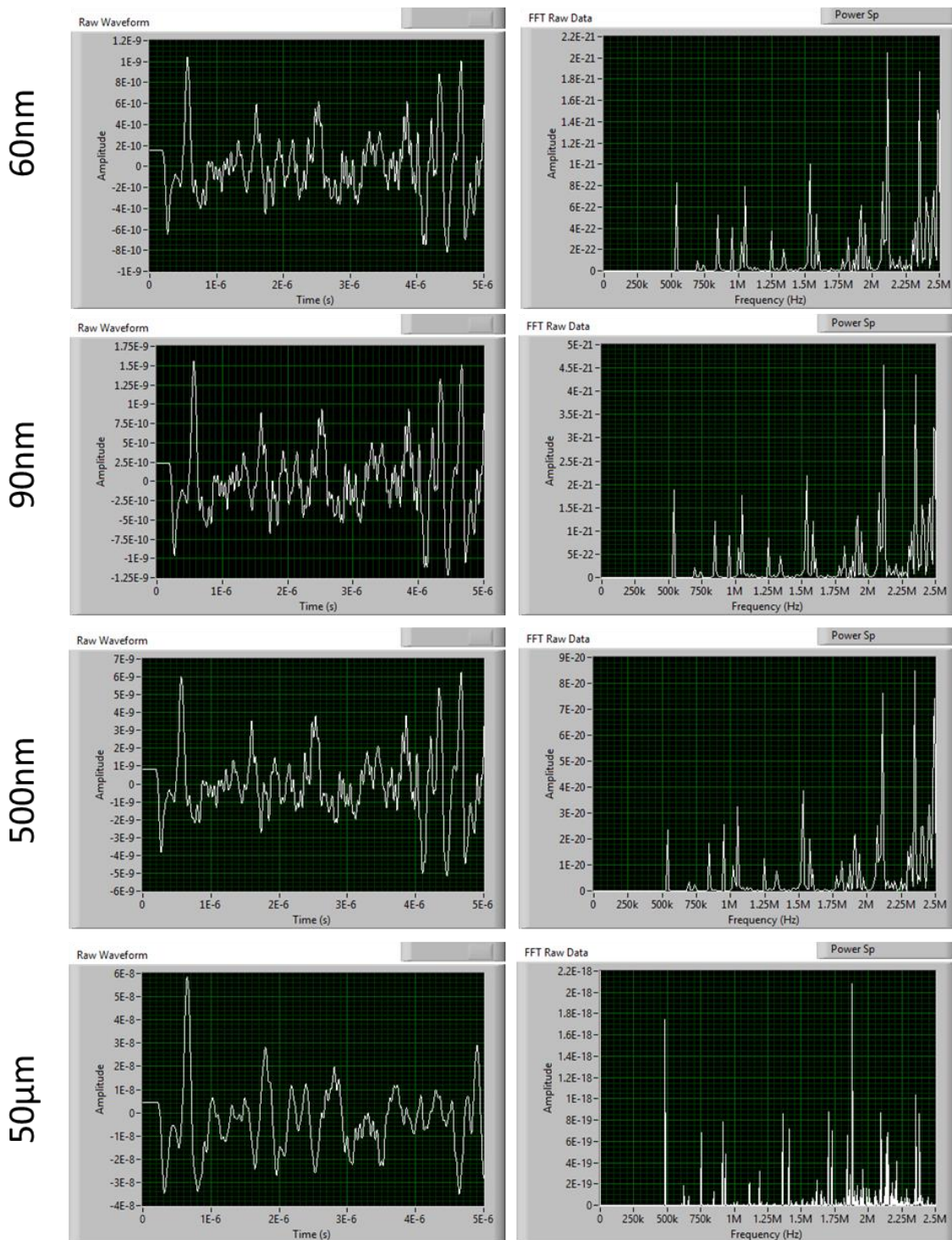


Figure 52: Displacement and frequency spectrums for various peak excitation displacements



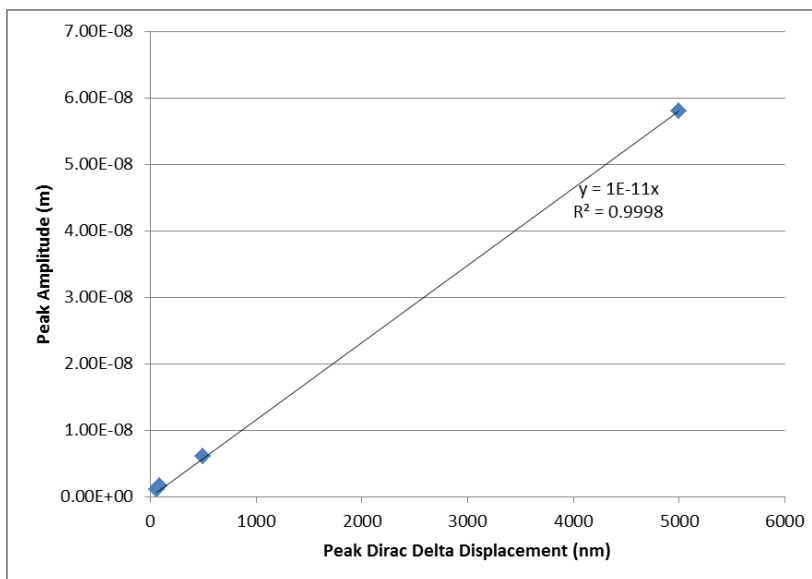


Figure 53: Peak waveform displacement

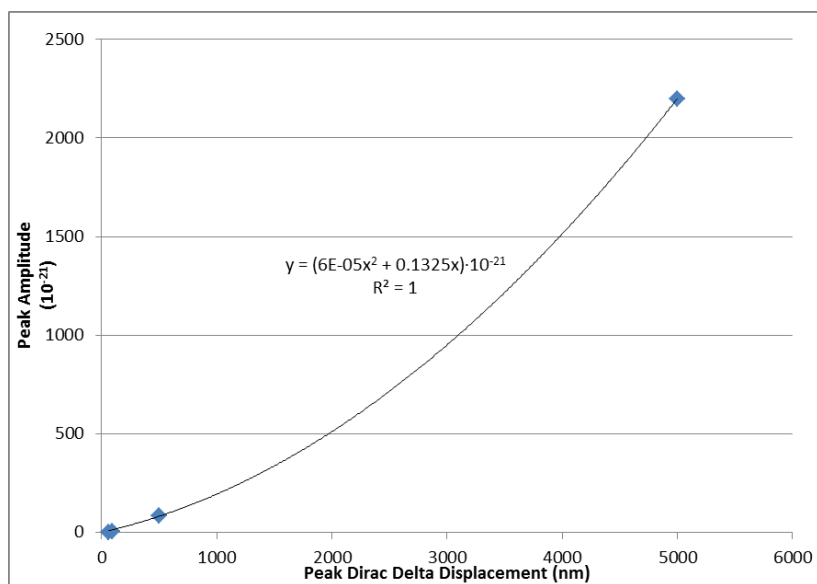
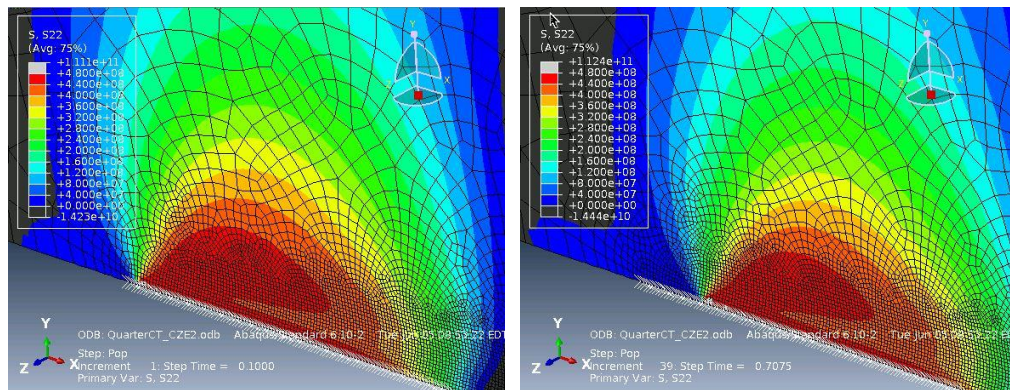


Figure 54: Peak frequency spectrum power

### *6.3 Preparing the Quasi-Static Crack Growth Model for Linking to the Dynamic Model*

In Chapter 5, the development a data-driven Cohesive Zone Model for quasi-static crack growth was discussed in detail from the geometry and boundary conditions to implementing in ABAQUS. The simulation was run and the extension of a 3 mm pre-crack was verified in Section 5.6. It should be noted that crack extension is measured from the tip of the pre-crack—the total crack length will be the crack extension plus 3mm. From this simulation, the two equilibrium states, which will be utilized as the input to the linked dynamic model, must be selected. The first equilibrium state, as shown in Figure 55, is chosen to be the time step directly before the first increment of crack growth where the separation is one time step away from exceeding the critical separation thus allowing stress at that node to go to zero and the extension of the initial pre-crack. The second equilibrium state was chosen to be when the crack extension was 2.0 mm, as shown in Figure 56. The extension value of 2.0mm is based upon the largest single increment of crack growth captured by DIC during the experiment discussed in Chapter 4. The total crack extension in the simulation was 2.5mm thus the simulation must be modified to capture only the segment of crack extension that is of interest. It is important to note that the quasi-static crack growth simulation assumes perfect conditions with perfectly homogeneous materials thus the crack will grow smoothly and in a predictable manner—this is not the case in realistic materials. Inclusions, voids, contamination, etc. may cause the crack tip to linger in a certain location before shooting forward by a certain extension, or conversely these defects may cause the crack to extend sooner than expected. To account for this, the largest observed single crack extension will be used to excite, as shown in Section 6.2, the largest energy in the model.

Once the equilibrium states have been chosen, the static simulation must be re-run to include a new step where the first time increment is the first equilibrium state and the last time increment is the second equilibrium state—This will isolate the segment of crack growth where the dynamic linked simulation will run. Table 6 below depicts the alteration in the quasi-static solver scheme.



**Figure 55: (Left) First equilibrium state – Directly before crack extension**  
**Figure 56: (Right) Second equilibrium state – After 2.0 mm of crack growth**

Figure 57 shows the through-thickness stress distribution of the cohesive elements along the crack interface. Note that the crack, in this simulation, is propagating at an angle across the thickness.

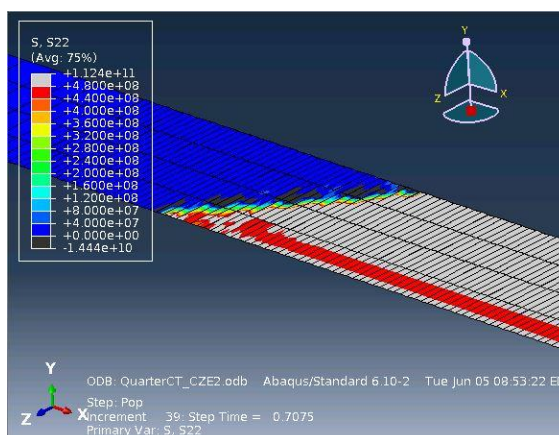


Figure 57: Through-thickness stress distribution at the second equilibrium point

Table 6: Modified quasi-static crack growth simulation scheme

Original Quasi-Static Simulation Scheme				Modified Quasi-Static Simulation Scheme			
Step	Start Time (s)	End Time (s)	Crack Extension (mm)	Step	Start Time (s)	End Time (s)	Crack Extension (mm)
1	0.00	40.00	2.50	1	0.00	34.45	0.00
--	--	--	--	2	34.45	39.00	2.00
--	--	--	--	3	39.00	40.00	2.50

#### 6.4 Modifying the Quasi-Static Model for Submodeling with a Dynamic Simulation

Submodeling is a technique where a portion of a larger (global) simulation is modeled in finer detail (local) and driven based upon the nodal reaction of the global simulation. This allows for highly refined meshing in an area of interest over a length of time of interest without the need of excessive computational strain in the global model caused by the refinement. Submodeling is a unique technique in that a static global model may be used to drive a dynamic local model, or vice-versa, again saving the computational time and storage space necessary to run the global simulation fully dynamically [52]. A full copy

of quasi-static model was made to be modified into the dynamic model without losing the original information. A large portion of the model was cut away, as shown in Figure 58, to yield a smaller model, focused around the crack tip and surrounding medium, to be used as the local submodel. The full model could not be used for this simulation with an appropriately sized mesh due to the RAM limitations on a single node. ABAQUS specifies that all preprocessing must run on a single node by a single core [52]. The reduced model utilizes 90% of the available RAM on a single node for preprocessing. The front face was partitioned into fifteen 5mm by 5mm, or closest portion of that around the edges, squares based on a starting location at the pre-crack tip. The intersection of these boxes will denote the location of sensors on the model. Figure 59 and Figure 60 show the front face partitions and the locations of sensors, noted by red dots, respectively.

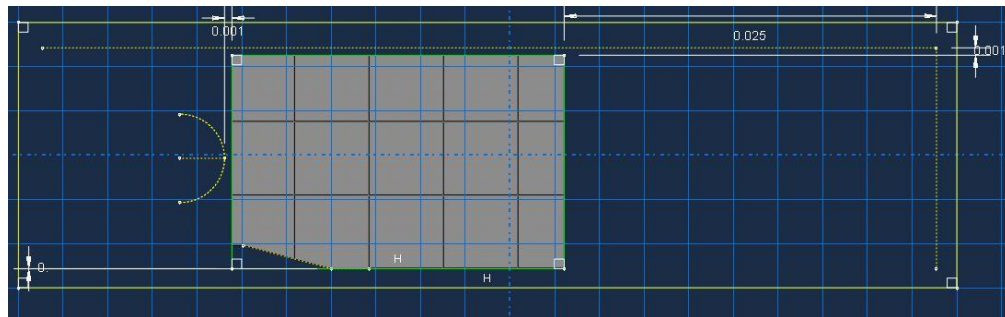


Figure 58: Submodel created by cutting away a large portion of the original quasi-static crack growth model

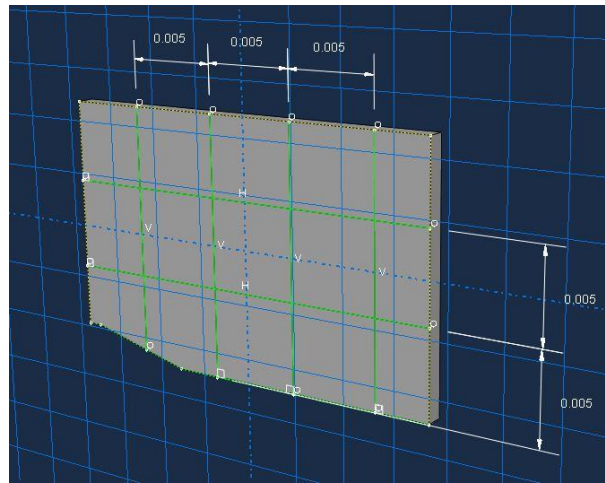


Figure 59: Front face partition for sensor location

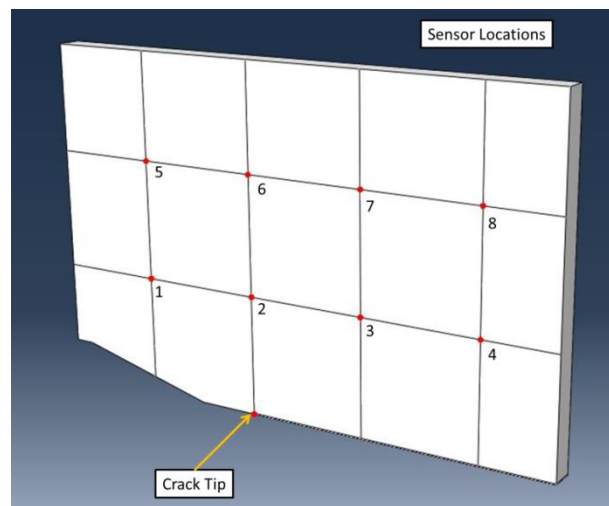
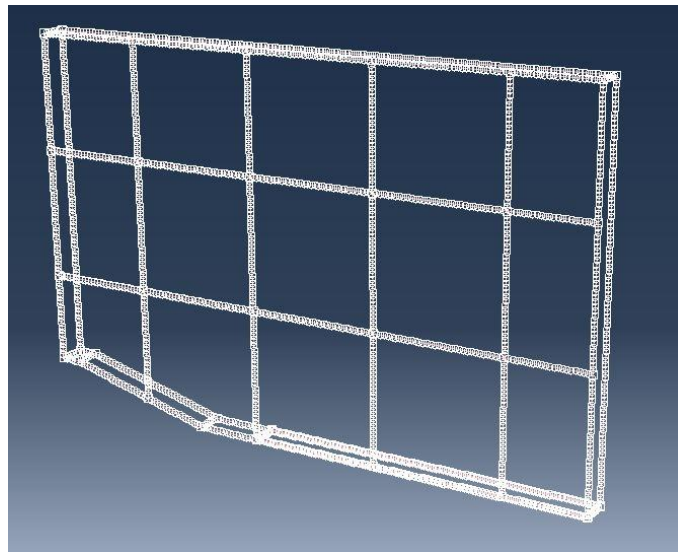


Figure 60: Sensors, denoted by red dots, located at the intersection of the partitions

It should be noted that, as with the simulations in Sections 6.1 and 6.2, the sensors are where the x-, y-, and z-direction displacements, velocities and accelerations are being recorded.

A global seed size of 0.10 mm was chosen for the local model which, when compared to the global model is approximately ten times more refined. Additionally, quadratic tetrahedron elements as opposed to the global model's quadratic brick elements were utilized—this means that in an equivalent global seed size, there are four times as many elements in the tetrahedral mesh as there are in the brick mesh.



**Figure 61: Global seed array for the dynamic model**

The results of these modifications yields a mesh, as shown in Figure 62 and Figure 63, with approximately 1.6 million elements and 9.6 million Degrees of Freedom. This demonstrates the versatility of Submodeling: Applying the same meshing technique to the entire global model yields over 10 million elements and 60 million Degrees of Freedom with an input file size of 1.1Gb which becomes difficult to transfer from a local

modeling node through an File Transport Protocol (FTP) client to a remote compute node.

Boundary conditions, of the ‘submodel’ type are applied to the entire outside perimeter of the submodel where a specific global model is chosen for driving the submodel boundaries. Within the global model, the boundary reactions are governed by the active DOFs and equilibrium endpoints that are selected through the application of global model steps.

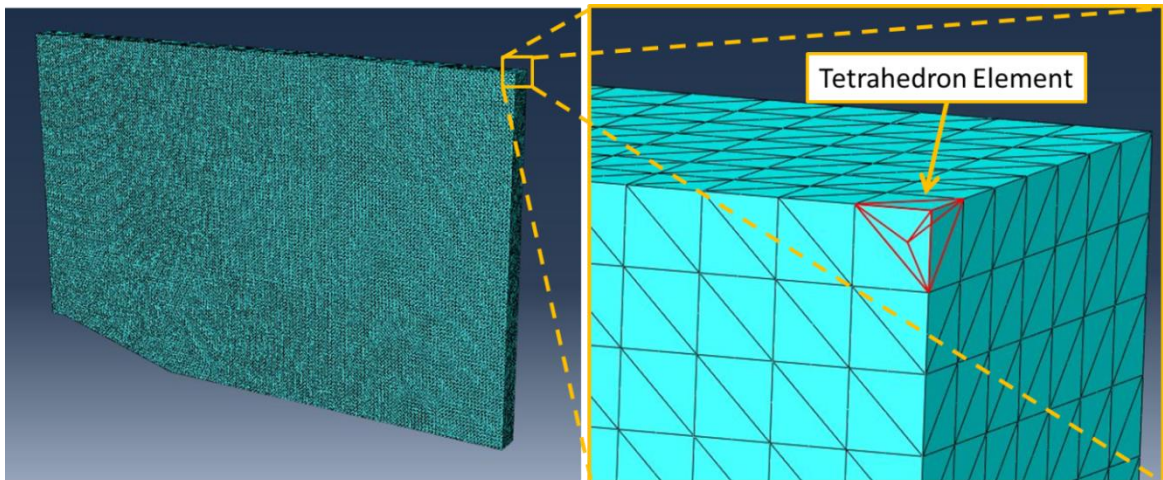
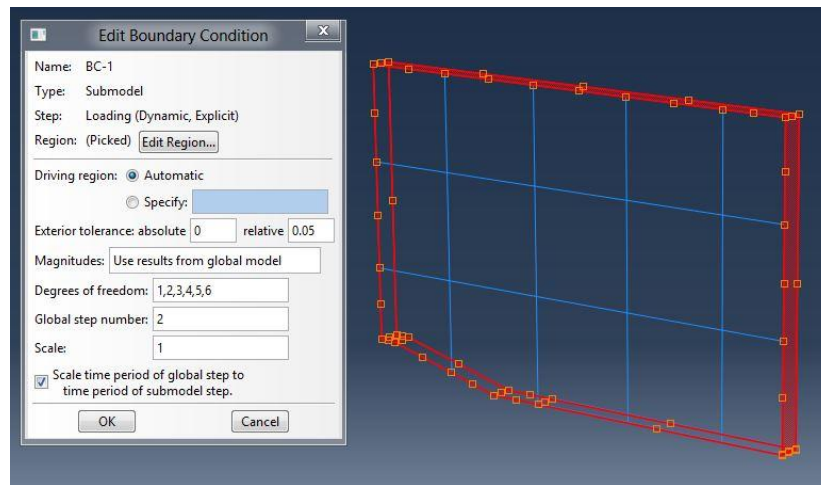


Figure 62: (Left) Tetrahedron mesh utilized for the dynamic simulation

Figure 63: (Right) Zoomed view of the tetrahedron mesh



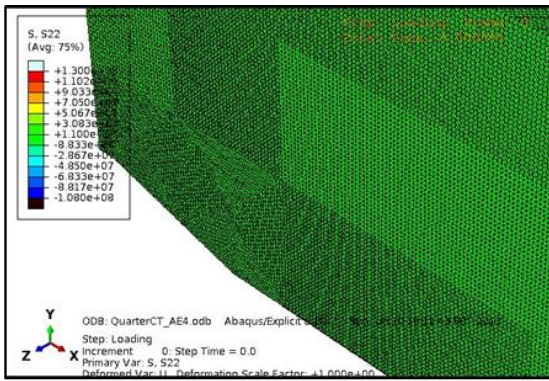


**Figure 64: Selected faces to apply submodel boundary conditions**

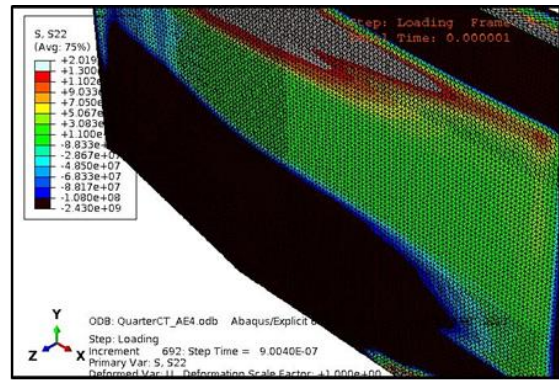
### *6.5 Data-Driven Simulation of Damage-Induced Elastic Wave Propagation*

In this simulation, the global model is the quasi-static crack growth simulation and the step which provides the boundary conditions is the second step, as described in Table 6, where a preselected amount of crack growth occurs. All six DOFs, x, y and z direction displacements and moments, are chosen as active. The total time length of the simulation was selected to be  $15\mu\text{s}$  to minimize the reflections of the elastic stress waves from the boundaries imposed by submodeling as shown in Figure 58. Below, shown in Figure 65, is the y-direction propagation of an elastic stress wave that has been produced through the utilization of equilibrium states in the quasi-static model. Similarly to how Acoustic Emissions were captured during the experiment in Chapter 4, the out-of-plane dynamic response of the system at the sensor locations shown in Figure 60 were captured, analyzed and displayed in Figure 66 along with their frequency spectrums. This figure

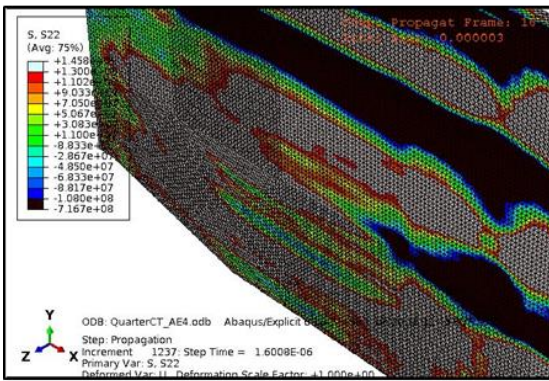
depicts the sensor information from sensor location 4, however the remaining 7 sensor locations are plotted in Appendix C. Generally speaking, specific patterns presented themselves in the waveforms and frequency spectrums captured at the eight locations: Displacement waveforms have peak frequencies in the range of 0Hz to 500kHz with a heavy weighting toward the lower spectrum values. In all cases the spectrum dies off quickly after 500kHz. Velocity waveforms showed a tendency to have peak frequencies in the range of 350kHz to 750kHz, and similarly to the displacement waveforms, the frequency spectrum dies off quickly after 750kHz. The acceleration waveforms were not nearly as consistent as displacement or velocity. While the trend in acceleration waveforms was to excite peak frequencies in the range of 2MHz to 4MHz, there was no trending to the spectrum dying off in one direction or another. Instead, the spectrum tends to be even distributed from 0Hz to 4MHz with smaller peaks in areas of similar frequency as the displacement and acceleration waveforms.



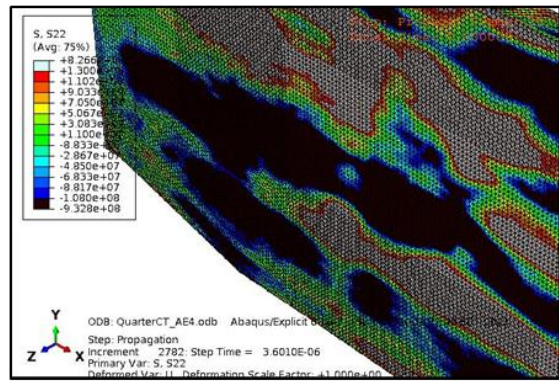
$t = 0.00\mu\text{s}$



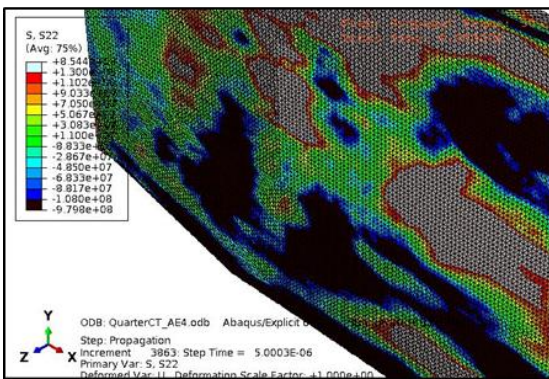
$t = 1.0\mu\text{s}$



$t = 2.0\mu\text{s}$



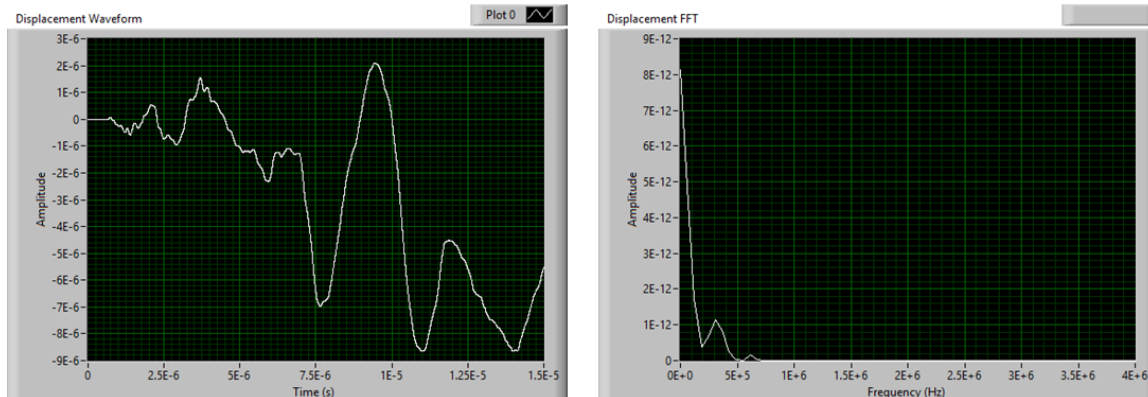
$t = 3.0\mu\text{s}$



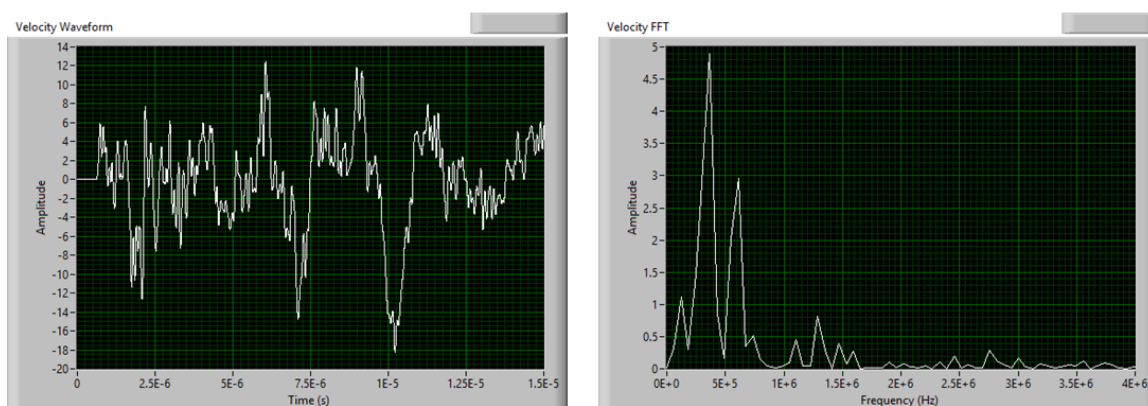
$t = 4.0\mu\text{s}$

Figure 65: Elastic stress wave propagation in the dynamic submodeling simulation that has been driven by the equilibrium states of the quasi-static simulation

## Sensor Location 4



## Displacement (m)



## Velocity (m/s)

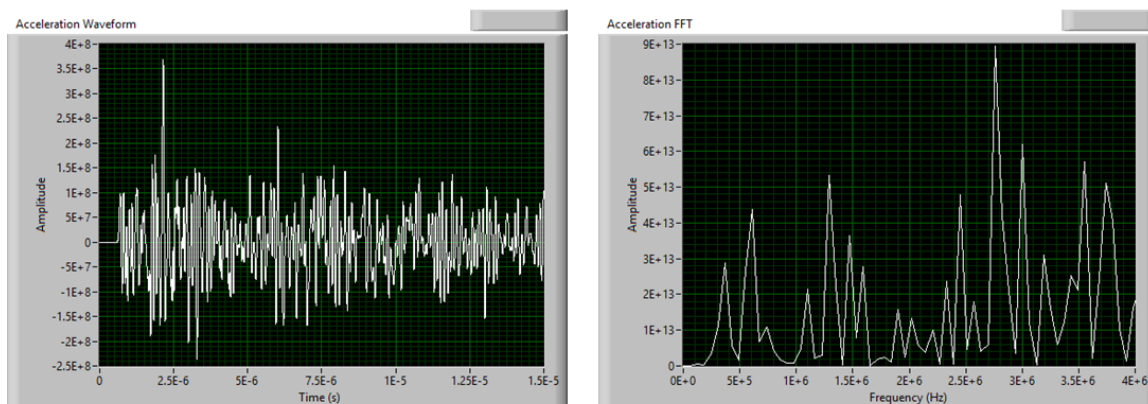
Acceleration ( $m/s^2$ )

Figure 66: Displacement, Velocity and Acceleration waveforms captured at sensor location 4 and their associated frequency spectrum analyses

An Acoustic Emission that was produced by crack growth in Aluminum Alloy 2024-T3 and captured during experimentation conducted by Vanniamparambil et al [3] is shown in figure 67. Comparing these waveforms yields some similarities in the general nature of the waveform where, unlike displacement, there appears to be numerous peak frequencies acting within the curve. It should be noted that the velocity waveform presented in this thesis is in the scale of meters per second due to the physical capturing of the displacement at that particular node whereas the scale of the waveform captured by Vanniamparambil et al is in Volts due to the transmission and conversion of the physical AE signal into the sensory system. Note that the time scale of the actual AE signal is twelve times longer than the signal captured in the simulation. Comparing the frequency spectrum of the waveform captured in the fracture experiment conducted by Vanniamparambil et al to that of the simulation shows similarities in the composition where peak frequencies occur in the range of 250kHz to 750kHz. Additionally, smaller peak frequencies are seen in both plots in the 100kHz to 250kHz range and the 900kHz to 1.5MHz range. The frequencies above 2.0Mhz taper off and stabilize near an amplitude of zero. It is interesting to note the similarities in the frequency contents of the actual Aluminum Alloy 2024-T3 test and the simulation considering the difference in location of the sensors. In the experiment conducted by Vanniamparambil et al, the sensors are located near the exterior edge, as shown in Figure 67, of a compact tension specimen which is equivalent in dimension to that used in the experiment discussed in Chapter 4 whereas in the simulation, the sensor location of the waveform plotted below is 5.0mm above and 10.0mm to the right of the crack tip as shown in Figure 59 and Figure 60.

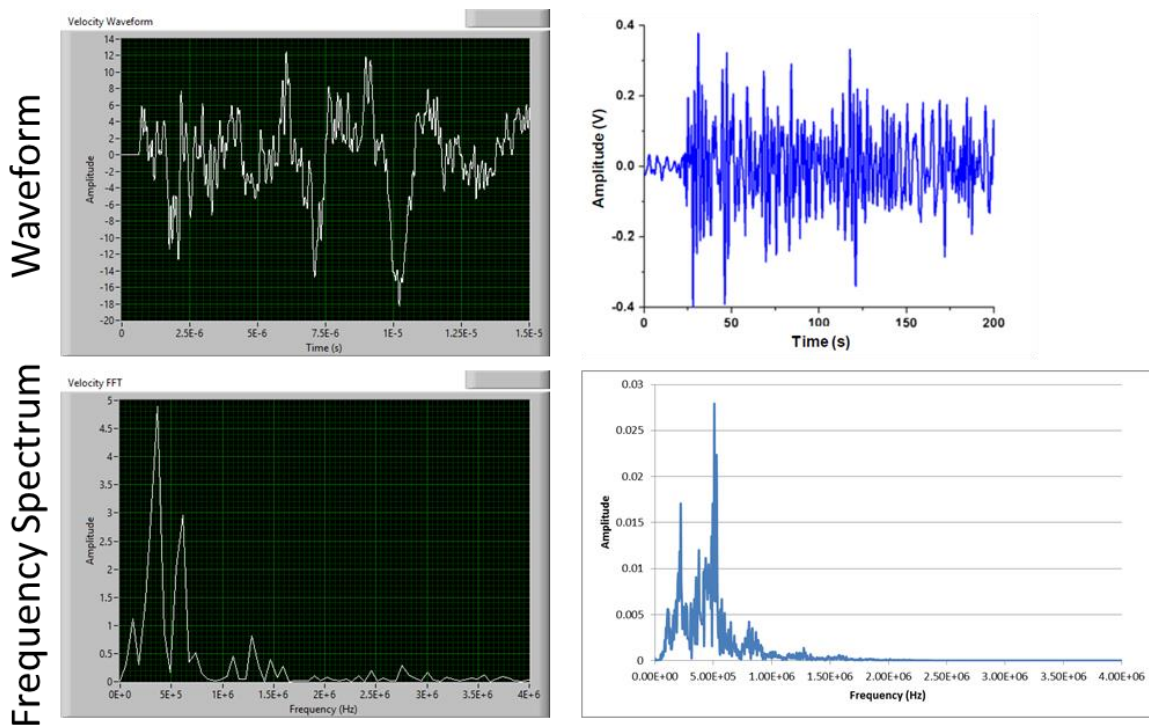


Figure 67: AE waveforms and frequency spectrums captured by the dynamic simulation (Left) and by Vanniamparambil (Right) [3]

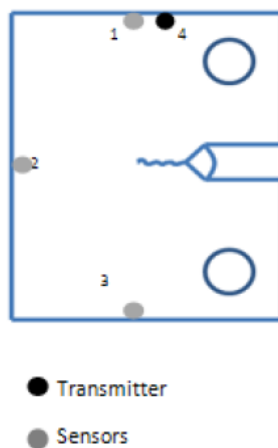


Figure 68: AE sensor location during an Aluminum Alloy 2024-T3 crack growth experiment [3]

## **Chapter 7: Conclusions and Future Work**

### *7.1 Summary and Conclusion*

This thesis has presented a collection of information, simulations and results that have become the basis of a novel approach to data-driven modeling of damage-induced elastic wave propagation through the utilization of advanced metrology and Nondestructive Evaluation techniques.

This work began by introducing the background of Fracture Mechanics, Cohesive Zone Modeling and Nondestructive Evaluation techniques in a historical and theoretical sense, while additionally posing the differentiation between the forward and inverse problems of damage-induced stress wave propagation. The mathematical basis of Cohesive Zone Modeling, and the coding required to integrate it into a simulation realm, was discussed in great detail along with the computational scheme which was utilized to run the simulations. A model was developed, with integrated Cohesive Zone Elements and the extracted damage parameters, which mimicked the experimental scheme. From this model, specific stress, strain and displacement equilibrium fields were chosen to act as boundary conditions into a dynamic Boundary Value Problem. The transient response of an equivalent model to an otherwise arbitrary energy release through the implementation of a sudden displacement jump was simulated to comprehend how displacement, velocity and acceleration waveforms may be captured throughout a continuum body. The results showed oscillating waveforms that resembled those captured during the experiment. The equilibrium points captured through the quasi-static crack growth simulation were also implemented into the same model, which drove the crack propagation, but without the

Cohesive Zone Elements. The transient response of this continuum body due to energy release, similar to the first transient simulation discussed, caused by the shift in equilibrium states was captured in this model. The important thing to note here, and the novelty of this approach, is that the energy release is based fully on the solution to the quasi-static crack growth simulation: absolutely no displacements or forces were imposed by the user. Instead, the displacements, forces, stresses and strains in the model are produced by the dynamic Boundary Value Problem that is minimizing the energy shift from one equilibrium state to another.

The results found herewith in are a significant contribution toward the next generation of data-driven simulations that are based upon and updated through experimental results.

The proof-of-concept has shown that based solely on the equilibrium states derived from a static simulation of crack propagation, a dynamic Boundary Value Problem could be solved to determine the transient response and propagation of elastic stress waves due to an upset in the energy balance. The possibilities of expansion for this thesis and the concepts proposed within are numerous and will be discussed in more detail in the next section.

## *7.2 Future Work*

The concept of utilizing realistic damage parameters in a Cohesive Zone Model to drive a dynamic transient simulation can be extended to research areas beyond Mode I fracture, as discussed below.



**Nondeterministic Crack Path:**

In this thesis, a major assumption was made: The crack will propagate in a perfectly linear line along the horizontal boundary which begins at the exact point of the notch tip. Realistically, however, the crack will follow the structure of the material and thus it may travel around inclusions, through voids, and branch, potentially creating two or more active cracks [57, 58]. There are two proposed ways, in Finite Element Analysis, to detach the crack from a set path. The first is using a remeshing technique which inserts new cohesive elements in real-time [8] through a prescribed algorithm. Alternatively, a triangular mesh with cohesive elements inserted between every element boundary will allow for branching and nonlinear crack propagation [5] within the constraint that the crack path is still limited to inter-element boundaries. The second method is a relatively new technique in Finite Element Analysis known as the eXtended Finite Element Method (XFEM) where B-splines are utilized to model inter-element discontinuities. An area that a crack is expected to form will be “refined” in the sense that specialized systems of equation that incorporate the B-spline algorithm will be used in place of the standard stiffness-based system of equation. This allows for a crack to form in any portion of, and in any direction within, an element, thus the crack is no longer bounded to the interface of elements [59, 60].

**Nonhomogeneous Materials and Non-Fracture Events:**

Cohesive Zone Modeling has been utilized in a variety of applications which range from non-homogeneous materials, such as composites [10, 12, 61] and adhesive delamination [11, 26], to non-fracture based energy events such as friction [13, 14] and impact [62,

63]. The extension of the concepts presented in this thesis to non-homogeneous materials, adhesive delamination, friction and impact would be a simple modification of the damage parameters, quasi-static simulation and equilibrium states in the dynamic linked model.

### **The Effects of the Sensory System on the Captured Results:**

Regardless of how accurate a sensing system is, there will always be a certain effect caused by the materials of the sensor, the data-sampling rate, and the open loop response of the data acquisition system. This, of course, holds true for Acoustic Emissions sensing as well. Studies have been conducted where the sensor's material response and the interaction between the continuum body and sensor have been taken into account in simulations. Through this set of imposed transfer functions, the theoretical elastic stress wave caused by damage, was converted into the measured elastic stress wave [6]. Through this understanding and the application of this thesis to the simulation of theoretical elastic waves, the given transfer function of a sensing system can be determined and "reversed" to give the true captured elastic stress wave.

### List of References

1. Anderson, T.L., *Fracture Mechanics: Fundamentals and Applications*. 3 ed 2004, Boca Raton, Florida: CRC Press. 640.
2. Hellier, C., *Handbook of Nondestructive Evaluation*, in *McGraw-Hill Handbooks* 2003. p. 594.
3. Vanniamparambil, P.A., et al., *An integrated structural health monitoring approach for crack growth monitoring*. *Journal of Intelligent Material Systems and Structures*, 2012.
4. Carroll, J., et al., *A hybrid experimental/numerical technique to extract cohesive fracture properties for mode-I fracture of quasi-brittle materials*. *International Journal of Fracture*, 2011. **169**(2): p. 113-131.
5. Zhang, Z.G.P.W.C., *Extrinsic Cohesive Modeling of Dynamic Fracture and Microbranching Instability in Brittle Materials*. *International Journal for Numerical Methods in Engineering*, 2007. **72**(8): p. 893-923.
6. Sause, M. and S. Horn, *Simulation of Acoustic Emission in Planar Carbon Fiber Reinforced Plastic Specimens*. *Journal of Nondestructive Evaluation*, 2010. **29**(2): p. 123-142.
7. Zhang, Z., G.H. Paulino, and W. Celes, *Extrinsic cohesive modelling of dynamic fracture and microbranching instability in brittle materials*. *International Journal for Numerical Methods in Engineering*, 2007. **72**(8): p. 893-923.
8. Khoei, A., et al., *Modeling of cohesive crack growth using an adaptive mesh refinement via the modified-SPR technique*. *International Journal of Fracture*, 2009. **159**(1): p. 21-41.
9. Park, K., G.H. Paulino, and J.R. Roesler, *A unified potential-based cohesive model of mixed-mode fracture*. *Journal of the Mechanics and Physics of Solids*, 2009. **57**: p. 891-908.
10. Feih, S., *Development of a User Element in ABAQUS for Modelling of Cohesive Laws in Composite Structures* 2005, Roskilde, Denmark: Riso National Laboratory.

11. Makhecha, D.P., *Dynamic Fracture of Adhesively Bonded Composite Structures Using Cohesive Zone Models*, in *Aerospace Engineering* 2005, Virginia Polytechnic Institute and State University. p. 206.
12. Sun, C. and Z. Jin, *Modeling of composite fracture using cohesive zone and bridging models*. *Composites Science and Technology*, 2006. **66**: p. 1297-1302.
13. Alfano, G., S. Marfia, and E. Sacco, *A cohesive damage–friction interface model accounting for water pressure on crack propagation*. *Computer Methods in Applied Mechanics and Engineering*, 2006. **196**(1–3): p. 192-209.
14. Alfano, G. and E. Sacco, *Combining interface damage and friction in a cohesive-zone model*. *International Journal for Numerical Methods in Engineering*, 2006. **68**(5): p. 542-582.
15. Bray, D.E., *Nondestructive Evaluation*, in *Kirk-Othmer Encyclopedia of Chemical Technology* 2000, John Wiley & Sons, Inc.
16. Ruegsegger, R.M.a.P., *Micro-Tomographic Imaging for the Nondestructive Evaluation of Trabecular Bone Architecture*. *Bone Research in Biomechanics*, ed. G. Lowet 1997, Van Diemenstraat, Netherlands: IOS Press.
17. Griffith, A.A., *The Phenomena of Rupture and Flow in Solids*. *Philosophical Transactions of the Royal Society of London. Series A, Containing Papers of a Mathematical or Physical Character*, 1921. **221**: p. 163-198.
18. Parnell, T.K., *Fracture Mechanics: Overview and Basics*, 1999. p. 20.
19. Brossman, M.W. and J.A. Kiess, *Energy Release Rates During Fracturing of Perforated Plates*, 1955, Ship Structure Committee: Washington, D.C. p. 27.
20. Westergaard, H.M., *Bearing Pressure and Cracks*. *Journal of Applied Mechanics*, 1938. **6**: p. 49-53.
21. Rice, J.R., *A Path Independent Integral and the Approximate Analysis of Strain Concentration by Notches and Cracks*. *Journal of Applied Mechanics*, 1968. **35**: p. 379-386.
22. Shi, Z., *Crack Analysis in Structural Concrete: Theory and Application* 2009, Oxford: Linacre House, Jordan Hill. 326.
23. Hellan, K., *Introduction to Fracture Mechanics*, ed. M. Eichberg 1984, United States of America: McGraw-Hill, Inc. 302.
24. Broek, D., *Elementary Engineering Fracture Mechanics* 1987, Dordrecht, Netherlands: Martinus Nijhoff Publishers.

25. Lawn, B., *Fracture of Brittle Solids*. 2 ed. Cambridge Solid State Science Series 1993, New York: Press Syndicate of the University of Cambridge. 381.
26. Alfaiate, J., et al., *Cohesive Zone Modeling of Mode I Fracture in Adhesive Bonded Joints*. Key Engineering Materials, 2007. **348 - 349**: p. 13-17.
27. Enkvist, J., A. Edland, and O. Svenson, *Human Factors Aspects of Non-Destructive Testing in the Nuclear Power Context: A review of Research in the Field*, 1999, Swedish Nuclear Power Inspectorate. p. 41.
28. Baram, J. and M. Rosen, *Prediction of low-cycle fatigue-life by acoustic emission—1: 2024-T3 aluminum alloy*. Engineering Fracture Mechanics, 1981. **15**(3-4): p. 477-486.
29. Worlton, D.C., *ULTRASONIC TESTING WITH LAMB WAVES*, in *Other Information: Decl. with deletions Mar. 5, 1957. Orig. Receipt Date: 31-DEC-581956*. p. Medium: X; Size: Pages: 17.
30. Grosse, C.U. and M. Ohtsu, *Acoustic Emissions Testing: Basics for Research - Applications to Civil Engineering* 2008, Leipzig, Germany: Springer.
31. Aljets, D., et al., *Acoustic emission source location on large plate-like structures using a local triangular sensor array*. Mechanical Systems and Signal Processing, 2012. **30**(0): p. 91-102.
32. Tobias, A., *Acoustic-emission source location in two dimensions by an array of three sensors*. Non-Destructive Testing, 1976. **9**(1): p. 9-12.
33. *Guidelines on use of acoustic emission testing on railway bridges*, 2009, Research Designs and Standards Organisation.
34. Ozevin, D., Z. Li, and Z. Heidary, *Early state damage detection of aluminum 7075-T6 plate based on acoustic emission*. 2011(Proc. SPIE 7983, 798304).
35. Ivanov, V.I., *Acoustic Emission: Some Problems, Tasks and Solutions*. NDT International. **17**(16): p. 323-328.
36. Masounave, J., et al., *Acoustic emission and fracture of ductile materials*. Engineering Fracture Mechanics, 1976. **8**(4): p. 701-709.
37. Bassim, M.N., *Detection of fatigue crack propagation with acoustic emission*. NDT & E International, 1992. **25**(6): p. 287-289.
38. Bassim, M.N., S.S. Lawrence, and C.D. Liu, *Detection of the onset of fatigue crack growth in rail steels using acoustic emission*. Engineering Fracture Mechanics, 1994. **47**(2): p. 207-214.

39. Berkovits, A. and D. Fang, *Study of fatigue crack characteristics by acoustic emission*. Engineering Fracture Mechanics, 1995. **51**(3): p. 401-416.
40. Maslouhi, A., *Fatigue crack growth monitoring in aluminum using acoustic emission and acousto-ultrasonic methods*. Structural Control and Health Monitoring, 2011. **18**(7): p. 790-806.
41. Yu, J., et al., *Prediction of fatigue crack growth in steel bridge components using acoustic emission*. Journal of Constructional Steel Research, 2011. **67**(8): p. 1254-1260.
42. Andreykiv, O., et al., *Acoustic emission estimation of crack formation in aluminium alloys*. Engineering Fracture Mechanics, 2010. **77**(5): p. 759-767.
43. *ARAMIS User Manual - Software*2009, Germany: GOM Optical Measuring Techniques.
44. Schwartz, E., *ARAMIS and PONTOS applications for Automotive testing: Measurements of components in operation made easy*, in *Trillion User Group Meeting*2011: Plymouth Meeting, PA.
45. Lianxiang Yang, e.a., *Measure Strain Distribution Using Digital Image Correlation (DIC) for Tensile Tests*, 2010, Oakland University: Rochester, MI.
46. Gain, A.L., *A Hybrid Technique to Extract Cohesive Fracture Properties of Elasto-Plastic Materials using Inverse Analysis and Digital Image Correlation*, in *Civil Engineering*2010, University of Illinois at Urbana: Urbana, Illinois. p. 115.
47. McNeill, S.R., W.H. Peters, and M.A. Sutton, *Estimation of stress intensity factor by digital image correlation*. Engineering Fracture Mechanics, 1987. **28**(1): p. 101-112.
48. Pop, O., et al., *Identification algorithm for fracture parameters by combining DIC and FEM approaches*. International Journal of Fracture, 2011. **170**(2): p. 101-114.
49. Reu, P.L., G.W. Wellman, and B.R. Rogillio, *Stable Crack Growth Measurement using DIC as a Tool for Model Validation*, 2006, Sandia National Laboratories, p. 1-6.
50. ASTM, *E399*, 1996, ASTM: Boston.
51. *ASTM Standard E1290-08, 2010, "Standard Test Method for Crack-Tip Opening Displacement (CTOD) Fracture Toughness Measurement," ASTM International, West Conshohocken, PA, 2010, DOI: 10.1520/E1290-08E01, [www.astm.org](http://www.astm.org).*
52. Hibitt, Karlsson, and Sorenson, *ABAQUS User's Manual v6.10*2010, Providence, RI: Dassault Systemes.

53. *Atlas of Stress-Strain Curves*. 2 ed2002, Materials Park, Ohio: ASM International. 816.
54. Hibitt, Karlsson, and Sorenson, *ABAQUS Keyword Manual v6.10*2010, Providence, RI: Dassault Systemes.
55. Council, H.A., *ABAQUS Performance Benchmark and Profiling*, 2009.
56. *Dirac Delta Function*, in *Fourier Transform*2007, The University of Edinburgh School of Physics and Astronomy: Edinburgh, Scotland.
57. Becher, P.F. and M.K. Ferber, *Grain-size dependence of the slow-crack growth behavior in noncubic ceramics*. *Acta Metallurgica*, 1985. **33**(7): p. 1217-1221.
58. Hong, Y., et al., *Effect of grain size on collective damage of short cracks and fatigue life estimation for stainless steel*. *Fatigue & Fracture of Engineering Materials & Structures*, 1998. **21**: p. 1317-1325.
59. Mougard, J.F., P.N. Poulsen, and L.O. Nielsen, *A partly and fully cracked triangular XFEM element for modeling cohesive fracture*. *International Journal for Numerical Methods in Engineering*, 2011. **85**(13): p. 1667-1686.
60. Zi, G. and T. Belytschko, *New crack-tip elements for XFEM and applications to cohesive cracks*. *International Journal for Numerical Methods in Engineering*, 2003. **57**(15): p. 2221-2240.
61. Li, S., et al., *Use of a cohesive-zone model to analyze the fracture of a fiber-reinforced polymer–matrix composite*. *Composites Science and Technology*, 2005. **65**: p. 537-549.
62. Borg, R., L. Nilsson, and K. Simonsson, *Simulation of low velocity impact on fiber laminates using a cohesive zone based delamination model*. *Composites Science and Technology*, 2004. **64**(2): p. 279-288.
63. Kulkarni, M.N., *Reliability Assessment of Electronics Under Drop-Impact Using Cohesive Zone and XFEM Models*, 2011, Auburn University. p. 168.
64. Stowell, E.Z., *Stress and Strain Concentration at a Circular Hole in an Infinite Plate*, 1950, Langley Aeronautical Laboratory: Washington, DC.

## **Appendix A: The Importance of Mesh Independence**

Regardless of how geometrically accurate a finite element model is, it possesses no credibility or accuracy in representing a loaded structure if the model presents mesh dependence. Mesh dependence is a condition where the results of a finite element model is directly affected by the size, shape or type of mesh used in generating the discrete solution points. Mesh dependence occurs due to the interpolation of a solution between the discrete solution points which may become highly inaccurate if a phenomenon, such as but not limited to a crack, hole or inclusion, exists between solution points.

Theoretically, a finite element model will never achieve complete mesh independence considering the exact solution is achieved when the number of solution points equals infinity and a discretized solution will always have less than infinity solution points.

Alternatively, mesh independence is typically considered to be achieved when a solution meets one or both of the following criteria: The solution converges to a theoretically known solution within a prescribed tolerance; or when the difference in the solution between an original mesh and a refined mesh is within a prescribed tolerance.

A study was conducted to determine the solution mesh dependence of a theoretically infinite thin plate with a circular hole in the center under uniaxial loading as depicted in Figure 69 and Figure 70. The applied load is equivalent to a constant negative pressure along the entire upper boundary of 1000 Pa and will remain steady during all simulations, whereas the mesh seed size will decrease, producing a more refined mesh, for each



subsequent simulation. It should be noted that the outside boundary of the model will remain a constant seed size of 5.00 mm whereas the inside square boundary and hole, as seen in Figure 70, will have a variable seed size starting with 1.00 mm.

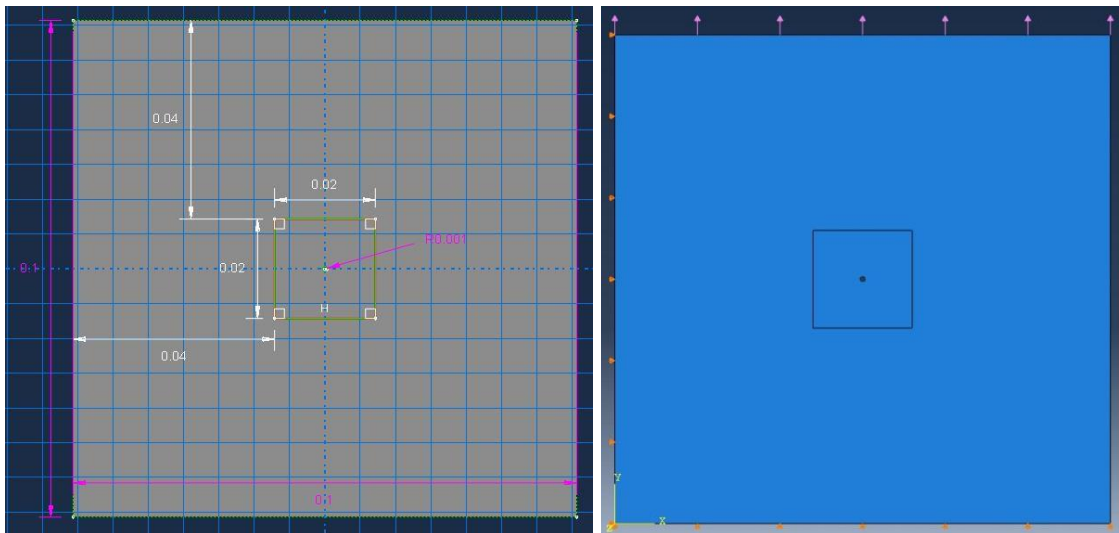


**Figure 69: (Left) Theoretically infinite plate with a circular hole in the center.**  
**Figure 70: (Right) Boundary conditions applied to the theoretically infinite plate.**

A plane stress 2D simulation was chosen due to the thin plate requirement of the infinite plate theory. Aluminum Alloy 2024-T3, which has an Elastic Modulus of 73.1GPa and a Poisson's Ratio of 0.33, was applied to the model to follow the remainder of the simulations discussed in the paper; however, the material properties are not important to this particular simulation since they do not affect the stress solution. The peak stress around an oblong hole in a thin plate is computed as follows [64]:

$$\sigma_{max} = \sigma \left(1 + 2 \frac{a}{b}\right) \quad A1$$

Where  $2a$  and  $2b$  are the width and height of the hole, respectively and  $\sigma$  is the applied stress (pressure). When  $2a = 2b$ , the hole is a perfect circle, as with the simulation, and the peak stress reaches 3000 Pa, which is exactly three times the applied pressure.

In each simulation, the variable seed size, total number of elements, peak stress and computational time was recorded. The first seed size selected was 1.00mm, which resulted in a mesh consisting of 2632 elements and a peak stress of 1586 Pa, or an error of 47%. The next three seed sizes selected were 0.50, 0.10 and 0.05 mm which resulted in meshes consisting of 5480, 94755, and 455,389 elements, respectively, and peak stresses of 1665, 2569 and 2844 Pa, or errors of 45%, 14% and 5%, respectively. The progression of refined meshes and associated stress contours are shown in Figure 71.

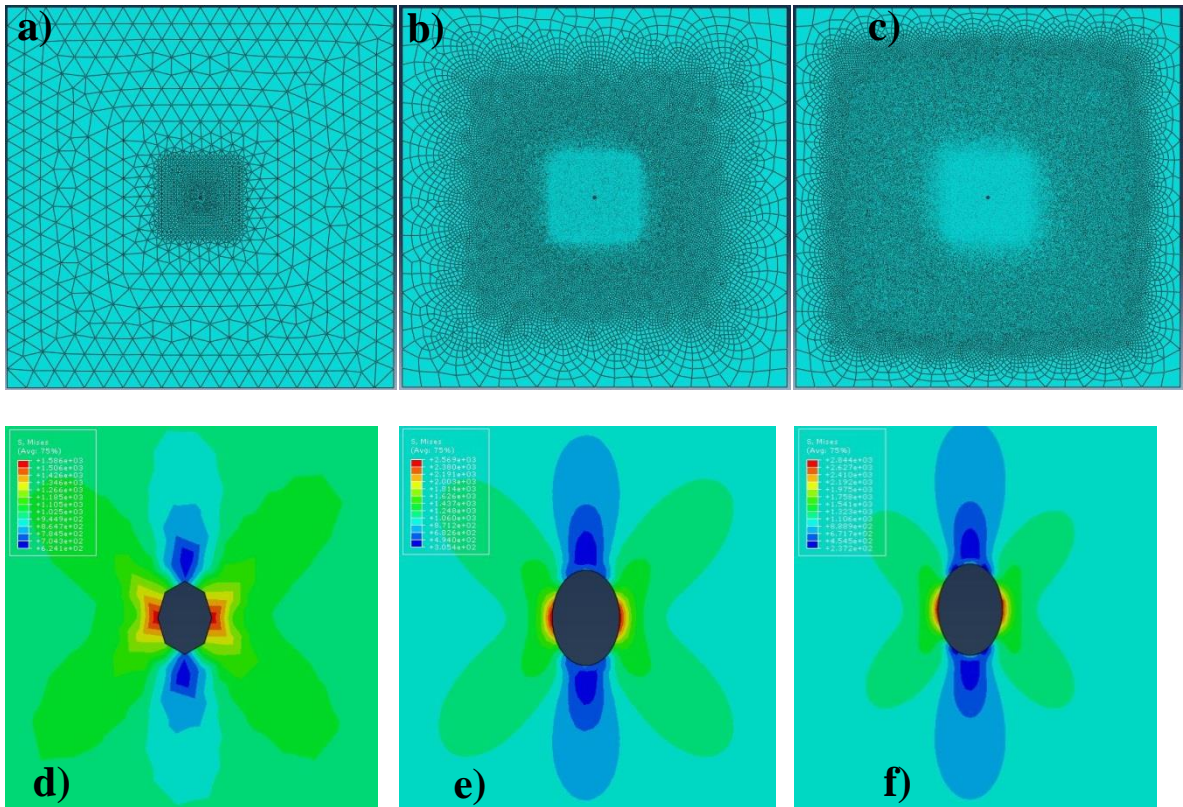


Figure 71: a) 1mm mesh, b) 0.1mm mesh and c) 0.05mm mesh and the associated stress contour for d) 1mm e) 0.1mm and f) 0.05mm meshes.

A logarithmic trend, which approaches the theoretical solution of 3000 Pa, was observed in peak stress as the total number of elements increased.

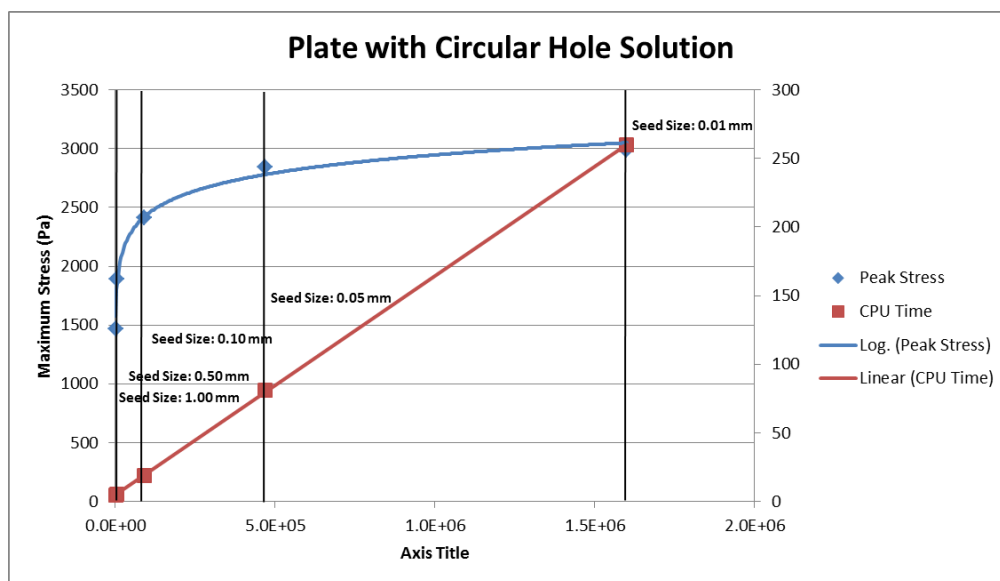
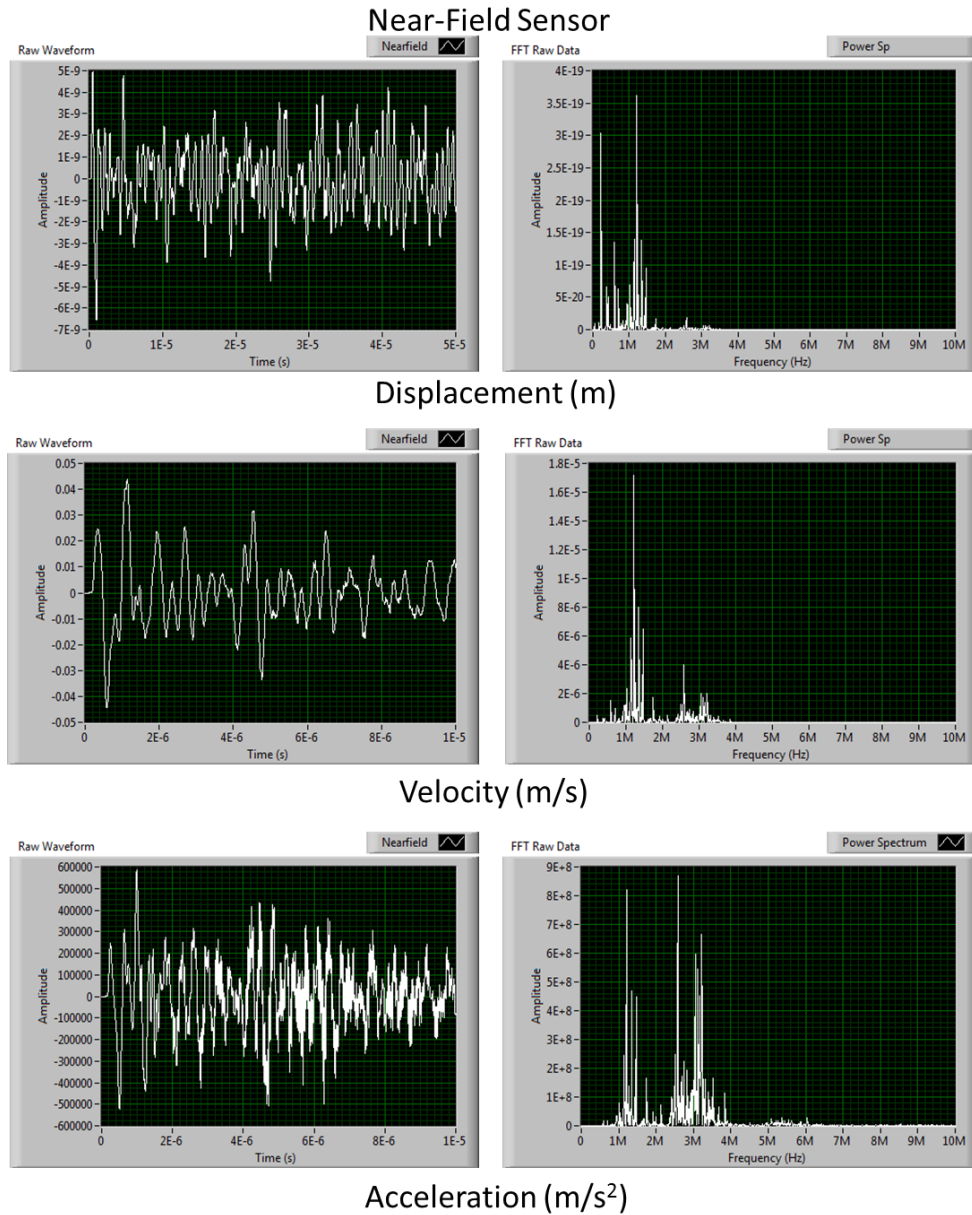


Figure 72: Mesh dependence simulation results

## Appendix B: Displacement, Velocity and Acceleration Waveforms due to a 90nm Displacement



**Figure 73: Displacement, Velocity and Acceleration waveforms captured at the near-field sensor and their associated frequency spectrum analyses**

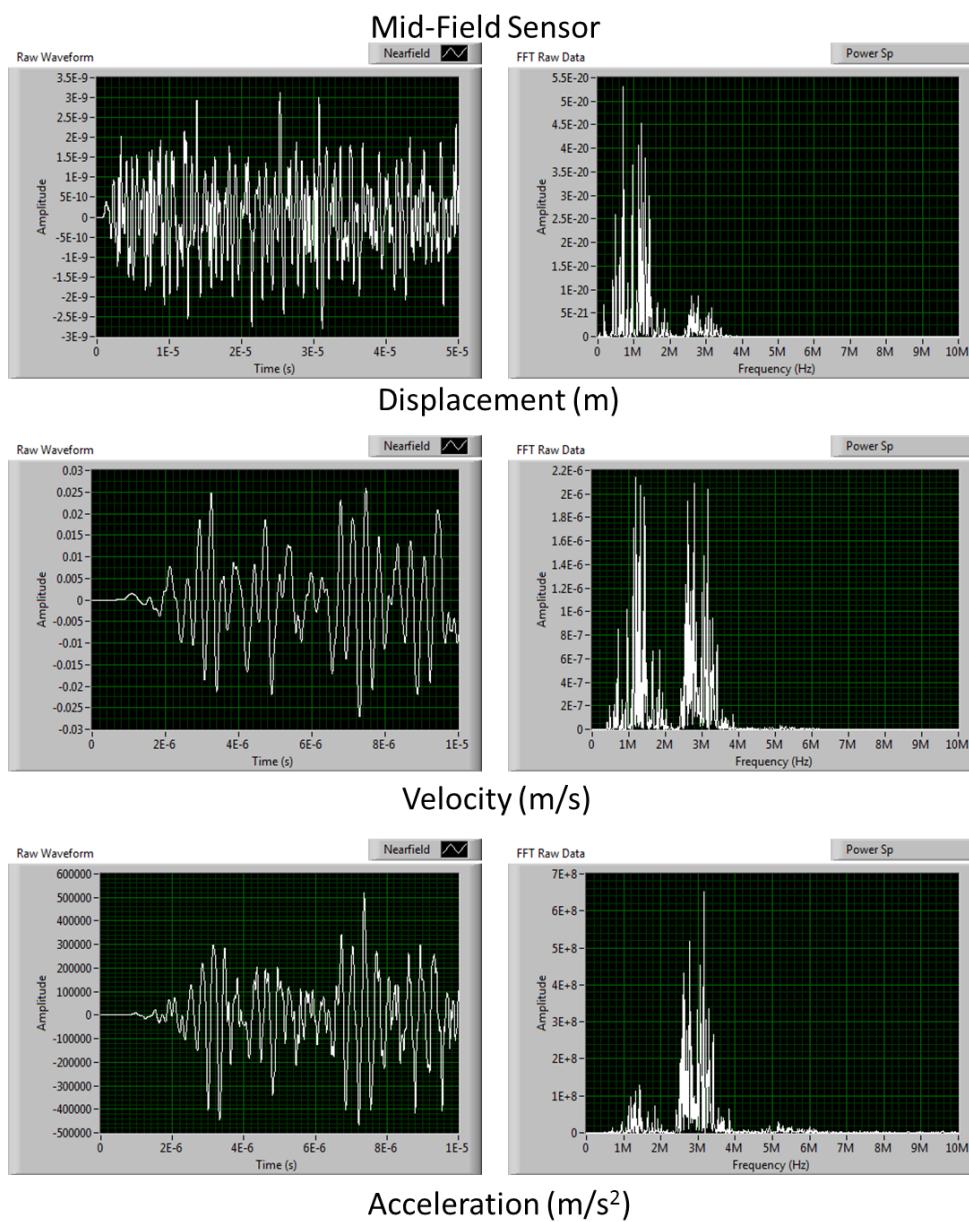
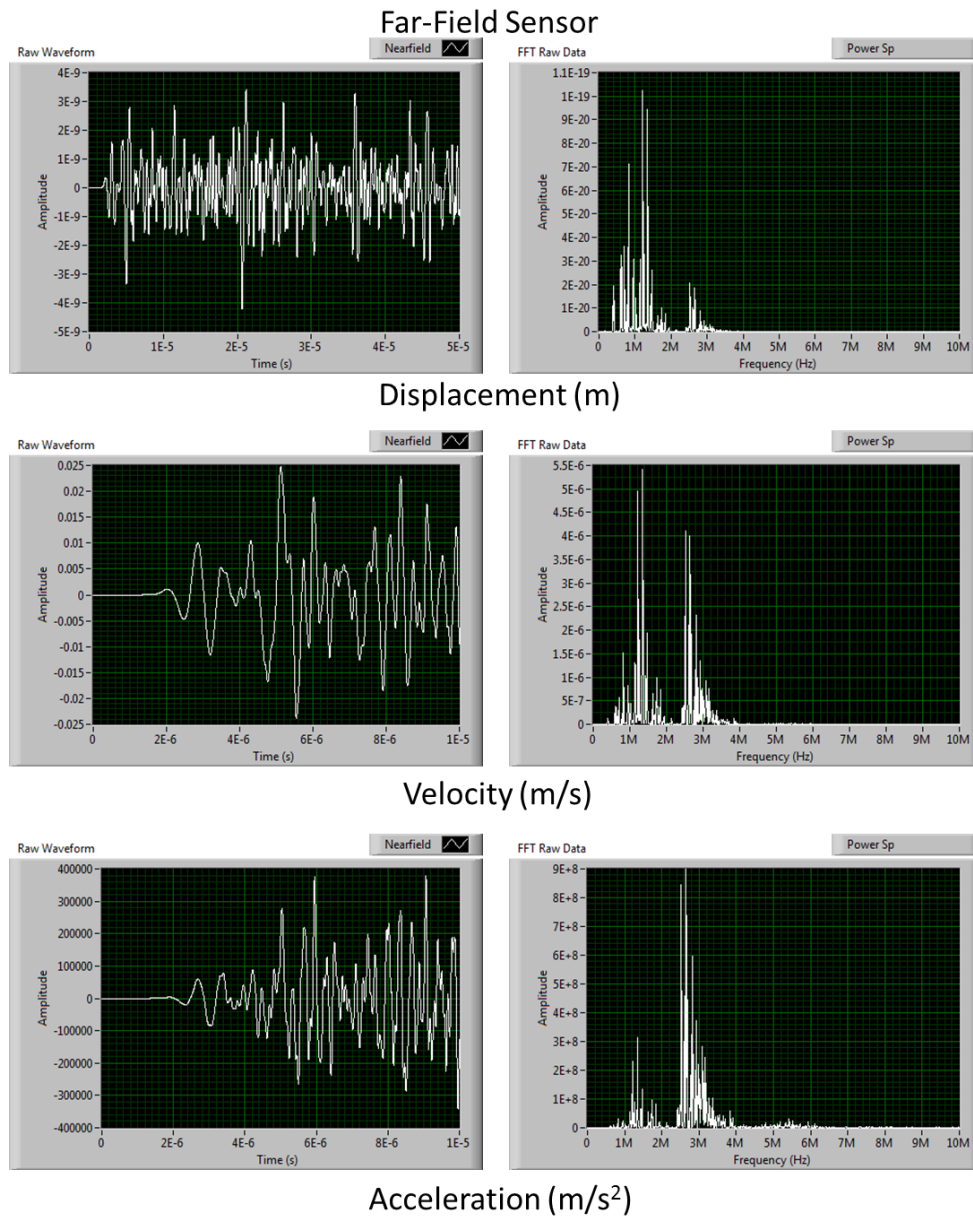


Figure 74: Displacement, Velocity and Acceleration waveforms captured at the mid-field sensor and their associated frequency spectrum analyses



**Figure 75: Displacement, Velocity and Acceleration waveforms captured at the far-field sensor and their associated frequency spectrum analyses**

## Appendix C: Waveform and Frequency Spectrums Captured during the Dynamic Simulation

### Sensor Location 1

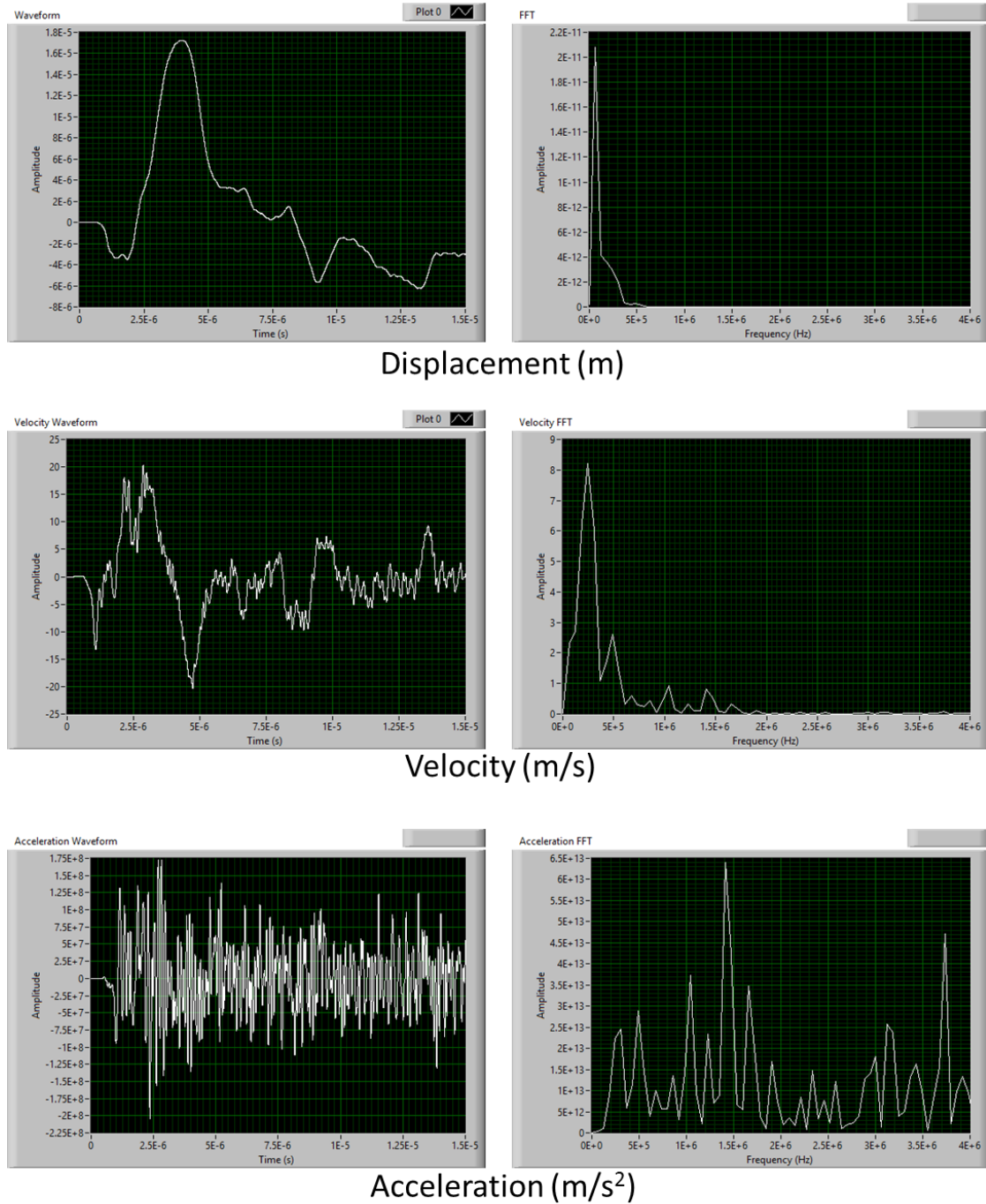
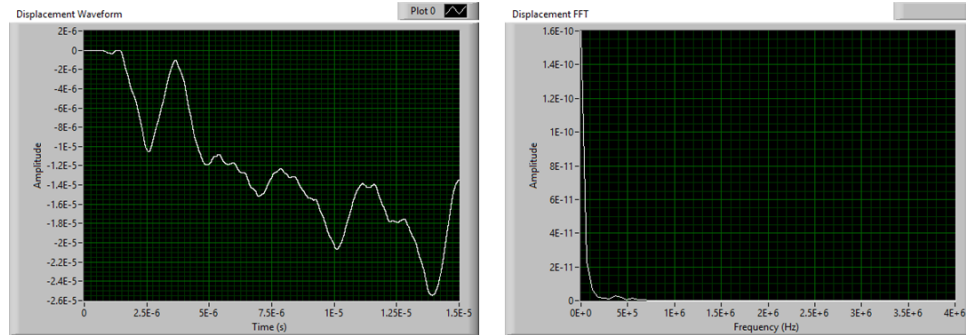


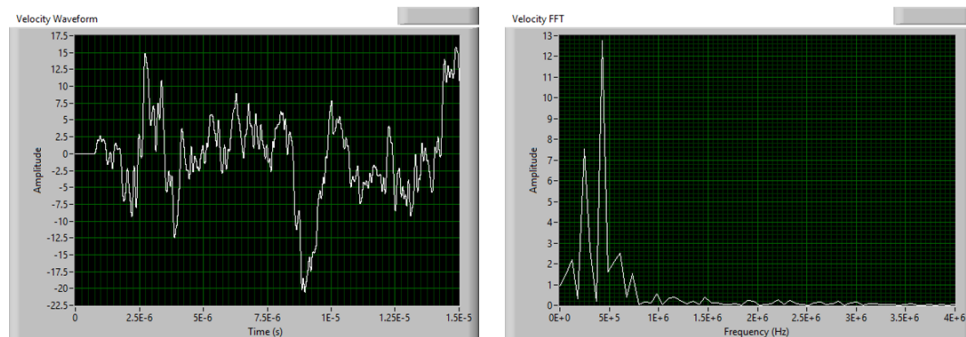
Figure 76: Displacement, Velocity and Acceleration waveforms captured at sensor location 1 and their associated frequency spectrum analyses



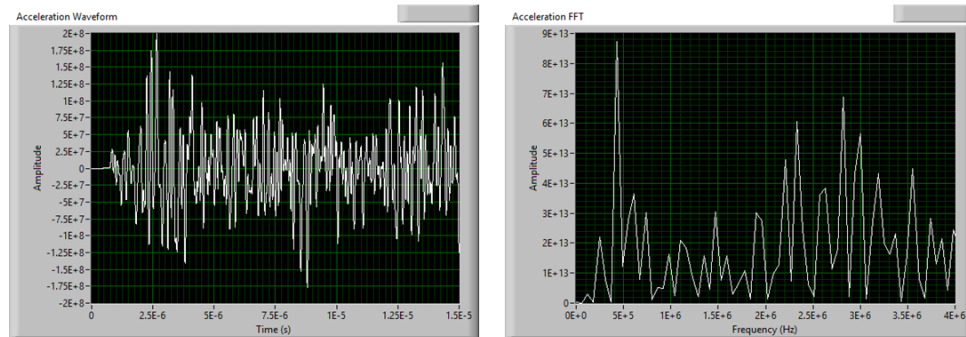
### Sensor Location 2



### Displacement (m)



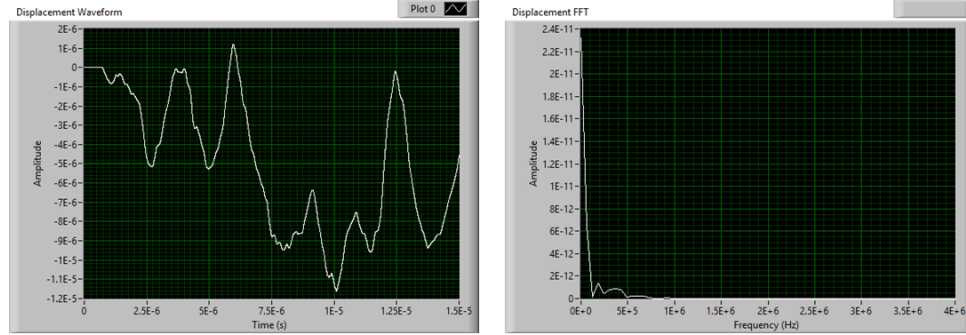
### Velocity (m/s)



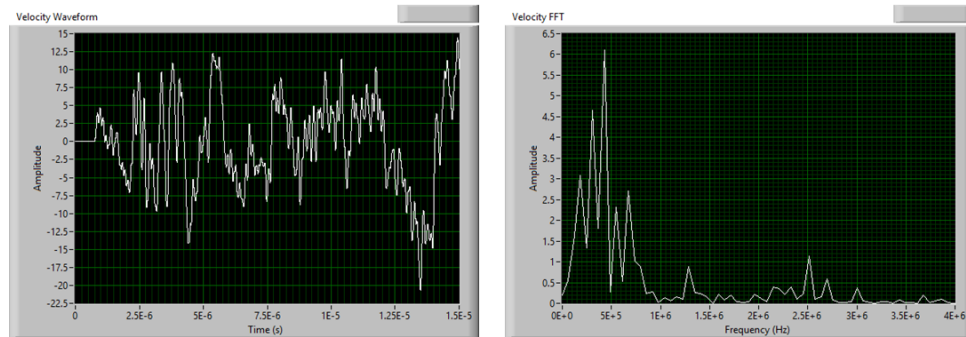
### Acceleration (m/s<sup>2</sup>)

Figure 77: Displacement, Velocity and Acceleration waveforms captured at sensor location 2 and their associated frequency spectrum analyses

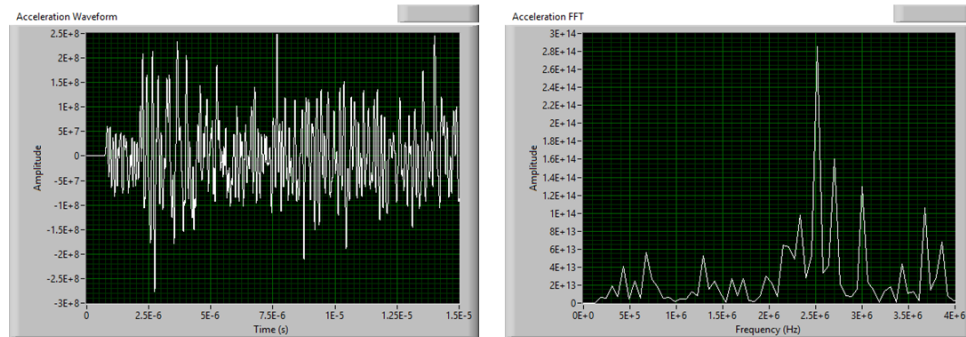
### Sensor Location 3



Displacement (m)



Velocity (m/s)



Acceleration (m/s<sup>2</sup>)

Figure 78: Displacement, Velocity and Acceleration waveforms captured at sensor location 3 and their associated frequency spectrum analyses

## Sensor Location 4

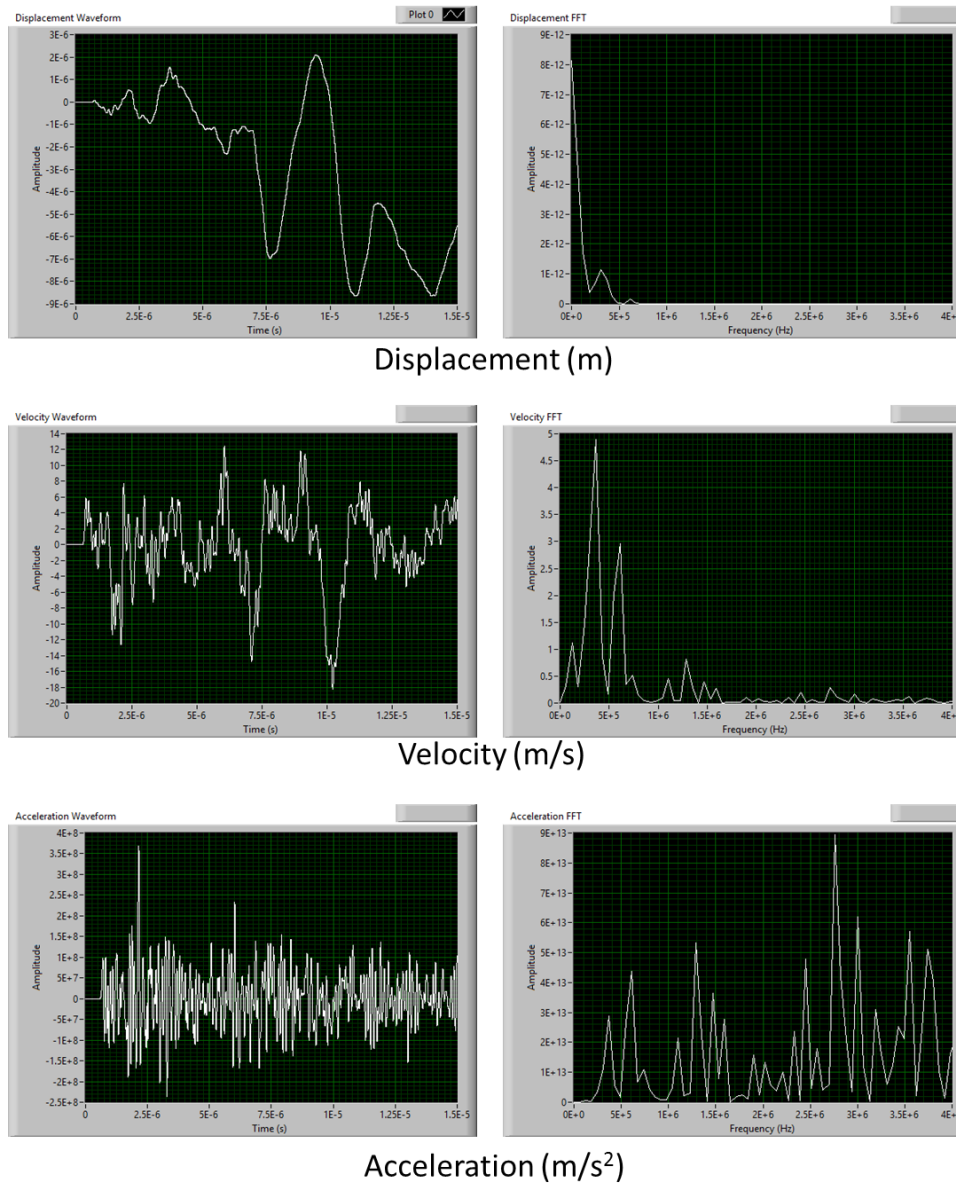
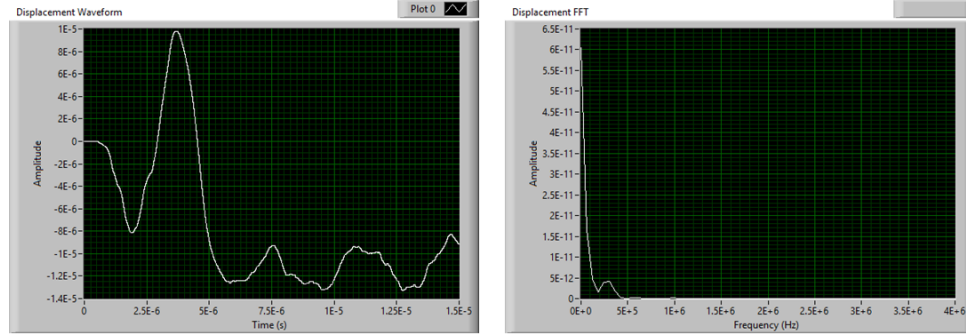
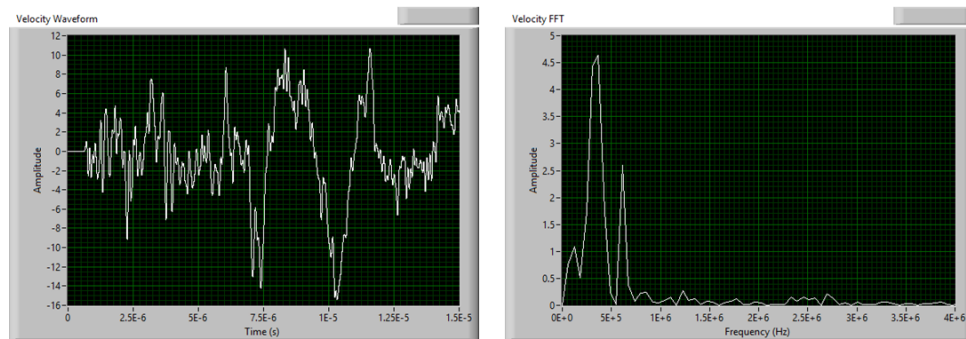


Figure 79: Displacement, Velocity and Acceleration waveforms captured at sensor location 4 and their associated frequency spectrum analyses

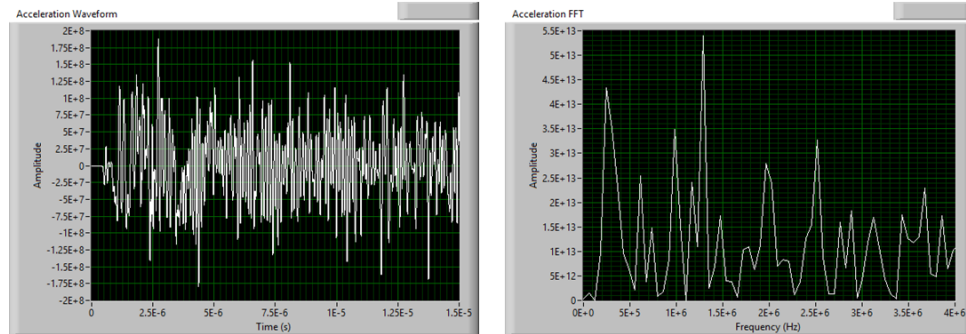
### Sensor Location 5



Displacement (m)



Velocity (m/s)



Acceleration (m/s<sup>2</sup>)

Figure 80: Displacement, Velocity and Acceleration waveforms captured at sensor location 5 and their associated frequency spectrum analyses

## Sensor Location 6

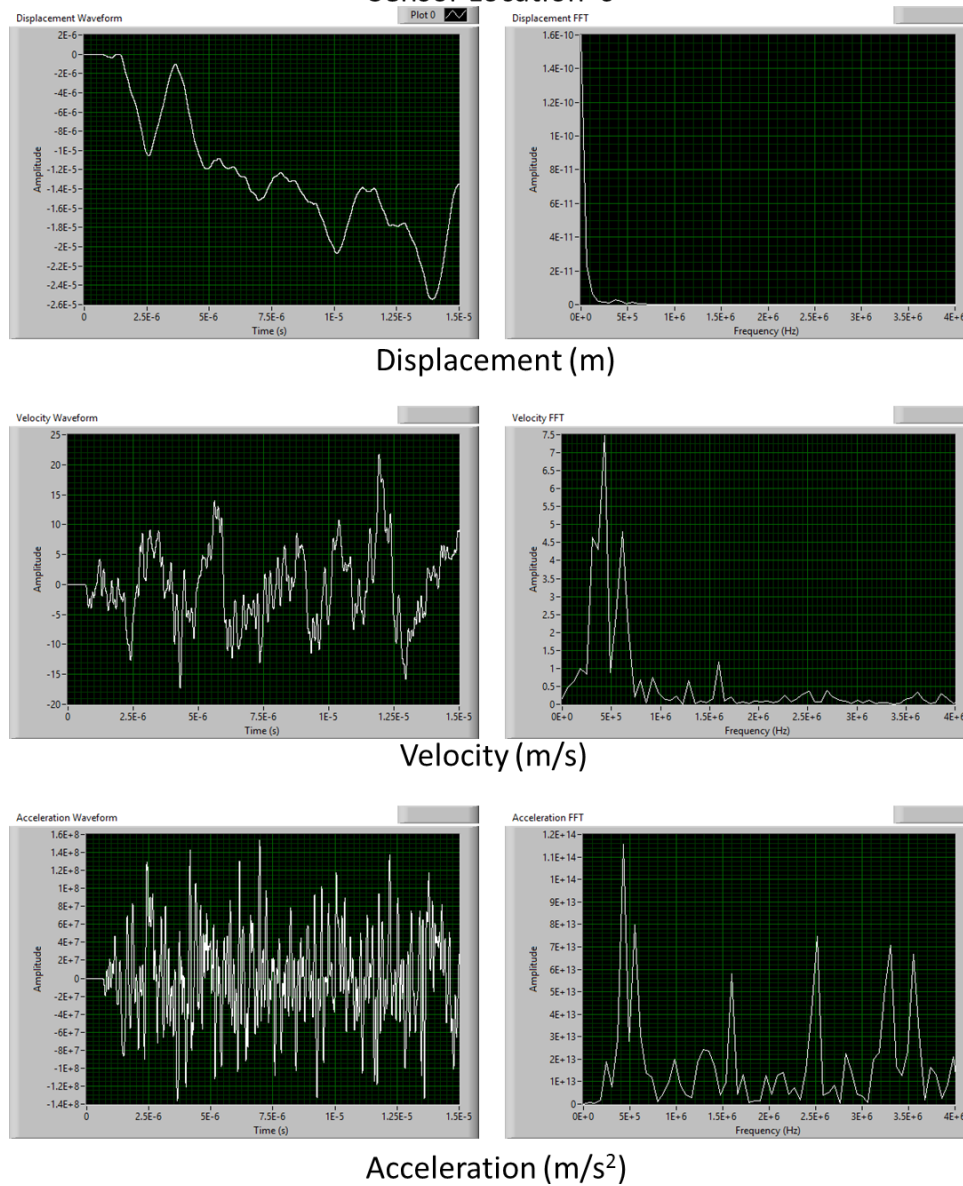
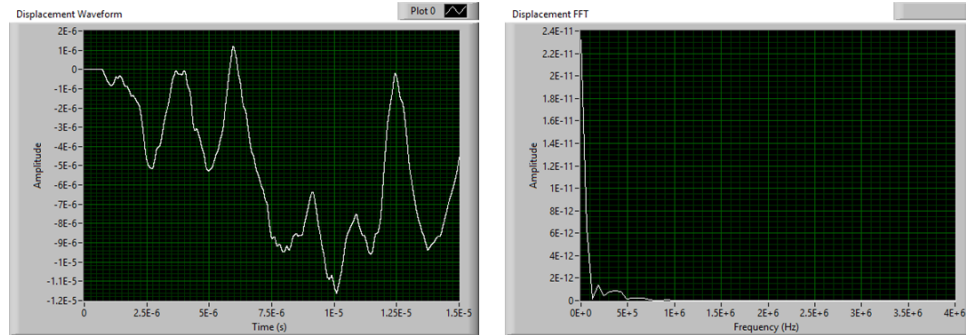
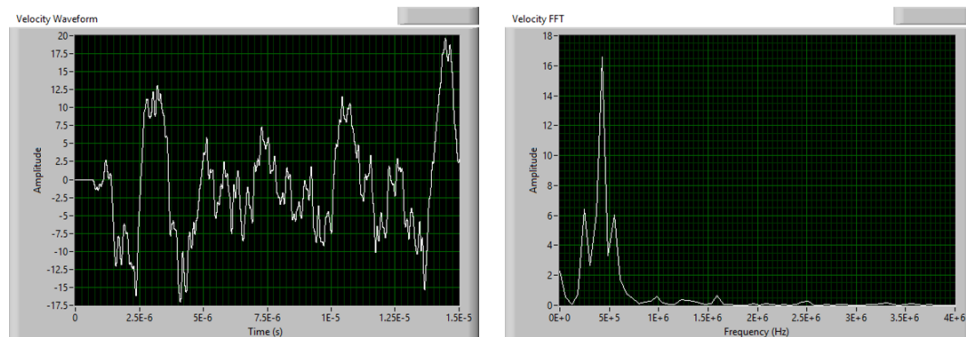


Figure 81: Displacement, Velocity and Acceleration waveforms captured at sensor location 6 and their associated frequency spectrum analyses

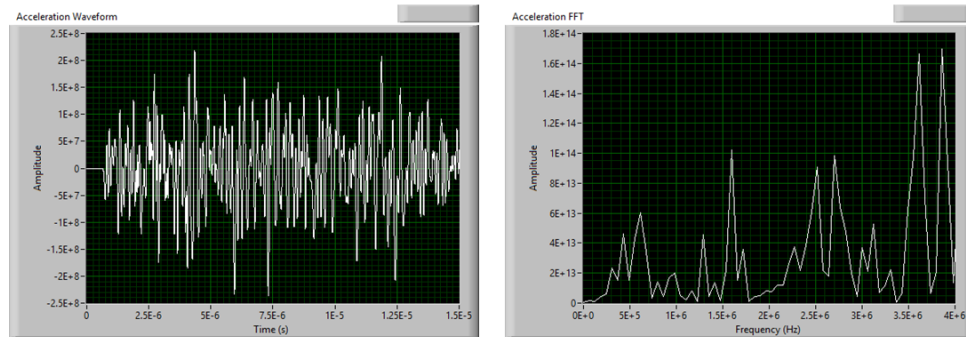
### Sensor Location 7



Displacement (m)



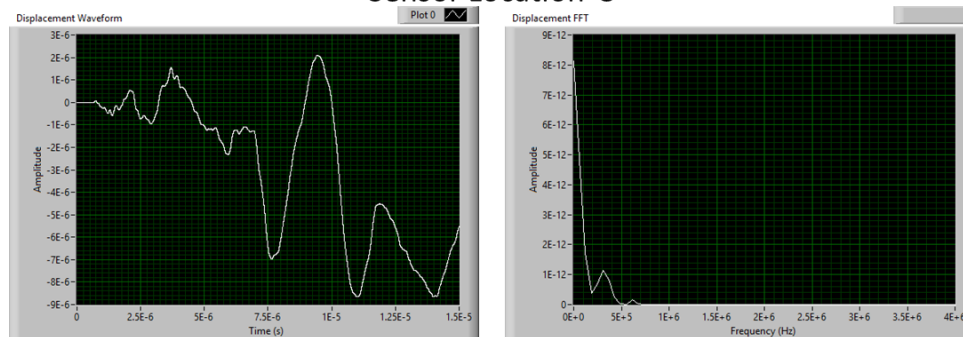
Velocity (m/s)



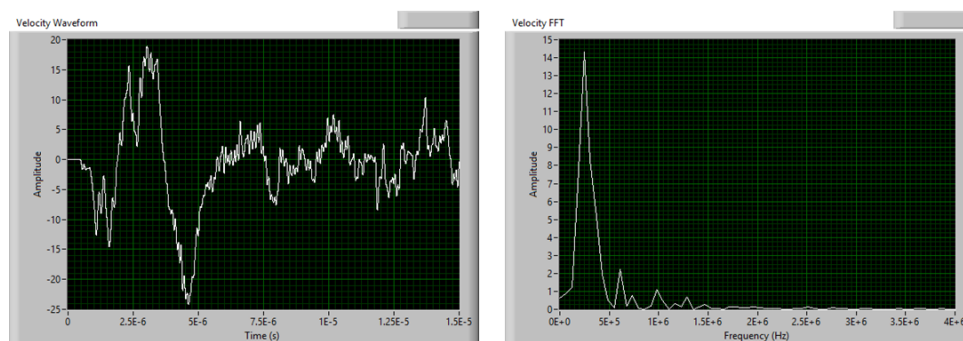
Acceleration ( $m/s^2$ )

Figure 82: Displacement, Velocity and Acceleration waveforms captured at sensor location 7 and their associated frequency spectrum analyses

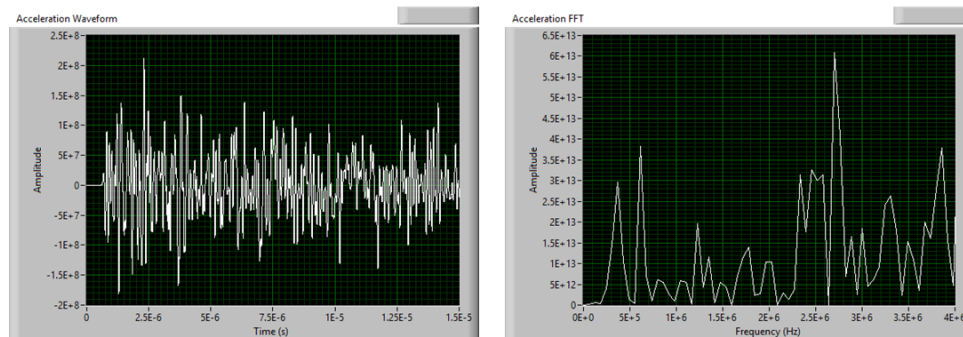
## Sensor Location 8



Displacement (m)



Velocity (m/s)

Acceleration ( $m/s^2$ )

**Figure 83: Displacement, Velocity and Acceleration waveforms captured at sensor location 8 and their associated frequency spectrum analyses**